UNIVERSITÀ DEGLI STUDI FIRENZE

PhD in
Architecture, design, knowledge
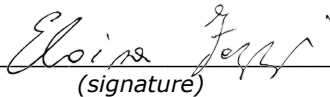# and safeguarding the cultural heritage
CYCLE XXXV

COORDINATOR Prof. Collotti Francesco V.

Fibre reinforced cementitious matrix (FRCM) for masonry strengthening:
modelling of textile-matrix interface

Academic Discipline (SSD) ICAR/08

Doctoral Candidate	**Supervisor**
Dr. Fazzi Eloisa	Prof. Rovero Luisa
(signature)	_(signature)_

Coordinator
Prof. Collotti Francesco V.

(signature)

Years 2019/2022

FLORENCE UNIVERSITY

DEPARTMENT OF ARCHITECTURE

Dissertation

FIBRE-REINFORCED CEMENTITIOUS MATRIX (FRCM) FOR

MASONRY STRENGTHENING:

MODELLING OF TEXTILE-MATRIX INTERFACE.

by

ELOISA FAZZI

BA in Philosophy, Catholic University of Milan, 2011
BA in Architecture, University of Florence, 2015,
MA in Architecture, University of Florence, 2018

Submitted in partial fulfillment of the

requirements for the degree of

Doctor of Philosophy

2023

DEDICATION

This dissertation is dedicated to Albertina

REVIEW

I would like to thank Professor Francesco Focacci for revising this manuscript.

FIBRE-REINFORCED CEMENTITIOUS MATRIX (FRCM) FOR MASONRY STRENGTHENING:
MODELLING OF TEXTILE-MATRIX INTERFACE.

ELOISA FAZZI

Florence University, Department of Architecture, 2023

Major Professor: Luisa Rovero, PhD

ABSTRACT

Fibre Reinforced Cementitious Matrix (FRCM) proved effective for retrofitting and strengthening unreinforced masonry structures, enabling capacity improvement with negligible added masses, and overcoming the drawbacks of Fibre Reinforced Polymers. Although extensive research has been carried out in recent years, a complete characterisation of the mechanical behaviour of such materials is yet not available. In this framework, the present research is aimed at a better understanding of the mechanical behaviour of FRCM. The general purpose of contributing to the definition of procedures for the characterisation of FRCM systems and the design of strengthening interventions is pursued through both experimental campaign and numerical modelling. In particular, within mode II fracture mechanics, a finite difference numerical model is developed for the description of FRCM behaviour in the characterisation tests. The proposed model describes the fundamental mechanism governing the response of these materials, i.e. the shear transfer mechanism at the textile-matrix interface. The enforcement of adequate loading conditions allows the model to correctly capture the FRCM behaviour in direct shear test (DST) and in direct tensile test (DTT) with any set-up. The im-

plementation of a displacement-controlled loading procedure, simulating crack widening, enables capturing all phases typically observed during experimental trials. Relying on independent solutions which consider the system in different phases since the beginning of the loading process, a new procedure for the construction of the load slip diagram of DTT is implemented, allowing estimation of load drops and stiffness degradation caused by cracks opening. A comprehensive parametric analysis highlights the effects that the variation of the main mechanical and geometrical parameters defining constituent materials have on the response of the FRCM system; the effects of cracks opening at different locations in DTT are also investigated through parametric analysis. The correlation between influencing parameters allows the description of the great variability of results obtained in characterisation tests in terms of variation of the test set-up, and of mechanical and geometrical parameters characterising constituent materials. The model proposed is validated through comparison with experimental data available in the literature and the outcomes of an experimental campaign specifically carried out on a set of FRCM systems. It is shown that even with fixed geometrical features of the specimen and gripping apparatus, great variability of results can be encountered, due to the role of matrix tensile strength in determining the mechanical response of DTT: the matrix tensile strength value and its random distribution along the reinforcement can determine cracks to open at different positions, thus greatly affecting the load and slip capacity of the system. Furthermore, it is suggested that matrix tensile strength plays a relevant role, along with the CML properties, also in determining the shape of the load slip diagram of DTT, so that bi-linear and tri-linear diagrams can be found within the same test set-up.

CONTENTS

LIST OF TABLES

CHAPTER 1

Introduction

1.1 FRAMEWORK

In the construction field, fibre-reinforced cementitious matrix (FRCM) proved effective for retrofitting and strengthening purposes of masonry and reinforced concrete structures, enabling capacity improvement with negligible added masses, and overcoming the drawbacks of fibre-reinforced polymers, (Kouris and Triantafillou 2018; Koutas et al. 2019).

Made of a reinforcing fibre embedded as an open mesh textile in an inorganic matrix, they efficaciously increase the tensile strength of the structural members to which are applied. Through the interface with the textile, the matrix transfers the external action from the substrate to the reinforcing textile, which finally bears tensile axial stress. Experimental campaigns carried out also in the framework of round-robin tests (Arboleda et al. 2016; Caggegi et al. 2017; Carozzi et al. 2017; De Santis et al. 2017b; Lignola et al. 2017) highlight that the response of these materials is mainly driven by the shear transfer mechanism activated at the textile-matrix interface. The most frequent failure modes are due to textile slippage and reaching of fibre tensile strength, as observed in adhesion tests, tensile tests, and fibre pull-outs. Experimental campaigns carried out to investigate the influence on the system response of test set-up, specimen preparation, textile geometry and mechanical parameters of constituent materials showed great variability of results.

Modelling of the mechanical behaviour of FRCM materials is usually tackled assuming a pure mode II fracture, to describe the textile-matrix interface. In this framework, the interaction at the textile-matrix interface is described by a cohe-

sive material law (CML), which summarises the phenomena involved in the shear transfer mechanism through a function or law relating relative slips and shear stresses at the interface. The CML can be determined directly through specimen instrumentation, or indirectly through the interpretation of the load slip diagram. Given the difficulty of a direct calibration of the CML from experiments, the problem becomes twofold and comprises a primal (or direct) and a dual (or indirect) problem: the primal problem implies the assumption of CML for the implementation of a model which describes the FRCM behaviour; in the dual problem, the CML has to be calibrated from the interpretation of experimental outcomes (Naaman et al. 1991).

Although extensive research has been carried out in recent years, a complete characterisation of the mechanical behaviour of such materials is yet not available (Grande, Ghiassi, and Imbimbo 2019). Various numerical and analytical models have been proposed for the description of characterisation tests of FRCM materials. However, the interpretation and prediction of the mechanical behaviour of FRCM systems call for further investigation. The great variability of results obtained in characterisation tests in terms of set-up test, and variation of the mechanical and geometrical parameters defining constituent materials, shape of the load-slip diagram, and calibration mode are hardly captured through a unique model. An interesting issue concerns the change in the shape of the load slip curves in direct tensile tests (i.e., bi-linear and tri-linear) that is attributed both to the quality of bonding (CNR 2014; Arboleda et al. 2016; D'Antino and Papanicolaou 2018) and to the test set-up, i.e. clamped or clevis grip, (De Santis et al. 2017a; De Santis et al. 2018; Nerilli and Ferracuti 2022). In Focacci, D'Antino, and Carloni (2022b) severe concerns have been posed on the reliability of tensile properties provided

by DTT, due to the dependency of the test results on the length of the gripping device, length of the specimen and the gauge length to which the strains are referred. These parameters, which are not uniquely prescribed by ACI 549.4 R-13 (2013) and CNR (2018), affect the measurements of the tensile capacity of the system, preventing the determination of the intrinsic system properties. The research presented was developed in relation to the pointed-out issues concerning a further understanding of the mechanical behaviour of FRCM materials.

1.2   FRCM FOR HISTORICAL MASONRY STRENGTHENING

Historical buildings call for appropriate strengthening techniques suited to providing the required structural performances and complying with the restoration principles stated by internationally acknowledged institutions (Venice Charter 1964; Principles 2003). Especially in masonry buildings, structural features are mostly merged with semantic and formal aspects, so that an adequate understanding of the mechanical behaviour of built heritage is essential to fully protect the historical evidence conveyed by the architectural heritage.

Seismic events, natural disasters and the ageing process highlight vulnerabilities of masonry structures, which constitute a relevant portion of the worldwide building stock. Such vulnerabilities are mainly related to the scarce tensile strength of un-reinforced masonry. Unless stress concentrations are determined in structural members with reduced cross-sections, the stability of masonry structures is usually not undermined by vertical loading conditions and self-weight. Tensile stresses caused by thrusting elements, in-plane and out-of-plane loading conditions determine the formation of cracks in the materials, which separates into a series of macro-elements. Therefore the mechanical behaviour of masonry can be

understood as an articulated series of in-plane and out-of-plane rigid displacements, i.e. local damage mechanisms. Strengthening techniques adopted in the last century often involved the introduction of inertial masses, such as reinforced concrete ring beams and coating, which proved detrimental during earthquakes. These interventions were meant to replace the structural capacity of buildings, but due to the increased mass and incompatible stiffness, they became an additional cause of vulnerability.

In this framework, FRCM materials disclose new perspectives for strengthening un-reinforced masonry thanks to continuous fibres embedded as open mesh textiles in inorganic matrices, which offer high levels of structural efficiency. Providing tensile strength to the masonry substrate, they can effectively hinder the activation of local damage mechanisms. Lime-based and cementitious matrices selected also allow for the reversibility of interventions, and guarantee good compatibility with the substrate, making them appropriate for applications on buildings belonging to the cultural heritage. In FRCM systems, the failure occurs at the fibre-to-matrix interface, which constitutes the weak interface of the system; the typical failure mode of FRP, i.e. delamination of the substrate, which would not be acceptable for interventions on the architectural heritage, is therefore avoided.

Technologies adopted for the strengthening of historical masonry should comply with the basic principles of restoration, enshrined in fundamental documents such as the Venice Charter and ICOMOS principles (Venice Charter 1964; Principles 2003): reversibility, compatibility and minimum intervention.

Although it is very often interpreted in an exclusively chemical sense, the concept of compatibility also concerns the physical and mechanical performance of strengthening techniques. Composite materials are compatible with historical ma-

sonry architectures due to the use of inorganic matrices, which guarantee adhesion to the substrate and good levels of breathability; also they do not modify the mechanical behaviour of the structure when subject to self-weight or vertical loads. The preservation of the original mechanical behaviour is also compliant with the demand for authenticity expressed by ICOMOS principles.

The concept of reversibility is related to the awareness of the progressive nature of scientific knowledge, so that improved strengthening techniques available in the future may replace those previously adopted. Such a possibility is guaranteed by the inorganic nature of the matrix used in FRCM, which allows for the removal of reinforcement from the substrate. The failure mode of these materials further ensures reversibility, since the FRCM reinforcement is damaged during actions, while the masonry substrate is preserved.

This fact, along with a proper understanding of the structural behaviour of buildings, supports the principle of minimum intervention, which ensures safety and durability with the least harm to heritage values. Since FRCM composites are often installed under plasters, stone blocks or bricks and at vault extrados, they also have a minimum (or null) visual impact on the strengthened building.

1.3   AIM AND SCOPE

The research here presented is aimed at contributing to a better understanding of the mechanical behaviour of fibre-reinforced composite materials. The general purpose of contributing to the definition of procedures for the characterisation of FRCM systems and the design of strengthening interventions is pursued through both an experimental campaign and numerical modelling. In particular, within mode II fracture mechanics, a finite difference numerical model is developed for

the description of FRCM behaviour in the characterisation tests: direct shear test (DST) and direct tensile test (DTT). Fundamental mechanisms driving the FRCM response under tensile loading conditions are identified and implemented in the model along with appropriate boundary conditions, which account for different loading procedures. Comparison with experimental data available in the literature and the outcomes of a specifically carried out experimental campaign are meant to provide validation to the proposed model. The model is intended to improve understanding of the relation between the great variability of results obtained in characterisation tests in terms of the test set-up, and variation of the mechanical and geometrical parameters defining constituent materials, shape of the load-slip diagram and failure mode.

1.4 RESEARCH OUTLINE

The research is organised as follows: in Chapter 2 an overview of FRCM systems, main characterisation tests and models proposed in the literature for the prediction of experimental results is reported; in Chapter 3 a finite difference model describing the mechanical behaviour of FRCM materials in direct shear tests and direct tensile tests is presented; in Chapter 4 a parametric analysis is carried out on the proposed model, to highlight the effects of the variation of the geometrical and mechanical parameters influencing the response of the system in both tests; in Chapter 5 an analysis of the combined variation of mortar tensile strength and CML characteristics is performed on the DTT model, highlighting the influences on the shape of the load slip diagrams; in Chapter 6, a specifically carried out experimental campaign is reported and the proposed model is also applied for the estimation of DTT results; Finally, conclusions are drawn in Chapter 7, where the

main achievement of the research are highlighted.

CHAPTER 2

State of the art

2.1 IDENTIFICATION

Fibre-reinforced cementitious matrix (FRCM) is a class of recently developed composite materials, consisting of continuous reinforcing fibres embedded in an inorganic fine-grain matrix. Inorganic matrices can be cement, lime or gypsum based and their properties are sometimes enhanced through the addition of short dispersed fibres and polymeric additives. To avoid negative effects on vapour permeability, fire resistance and durability, polymeric additives should be kept to a maximum of 10% by weight of the inorganic binder, according to CNR (2018), or to 5%, according to ACI 549.4 R-13 (2013). High-strength fibres, namely basalt, carbon, Polyparaphenylene Benzobisoxazole (PBO), Aramid and Kelvlar are typically employed as reinforcement, although the use of natural materials was also investigated (Olivito, Cevallos, and Carrozzini 2014; Asprone et al. 2011). The selected fibres are bundled in yarns comprising hundreds or thousands of single fibres, i.e. filaments, which have a diameter of a few microns (Hartig et al. 2012). Yarns are organised in bi-dimensional or tri-dimensional structures with a defined geometry through proper textile fabrication technologies, such as weaving, knitting, tufting, felting, braiding, or bonding, (ACI 549.4 R-13 2013). When fabrication techniques, e.g. weaving, envisage that a series of parallel yarns are kept stationary and others are introduced passing over and under them, a primary direction, called warp, and a secondary direction, called weft or fill, can be identified in the textile. Differently from polymers, inorganic matrices are unable to fully impregnate yarns, due to the grain size and the reohological characteristics of the fresh paste, which prevent it

from flowing among the inner fibres. Therefore two different areas can be identified in an embedded yarn: a sleeve or outer ring imbued with matrix, and a dry core (Hartig et al. 2012). The presence of a dry core is considered, by definition, a distinctive feature of FRCM (ACI 549.4 R-13 2013; Arboleda et al. 2016), distinguishing them from FRP. In fact, in case a polymeric coating is applied to the fibres and completely imbues them, the reinforcement system is no longer considered an FRCM, but an FRP embedded in mortar (Arboleda et al. 2016).

The textile geometry of the reinforcing fibres employed in FRCM is meant to provide geometrical stability during casting and strength to the composite (Peled and Bentur 2000; Peled, Bentur, and Yankelevsky 1998). Furthermore, since the mortar matrix cannot fully impregnate fibres, the open mesh geometry of the textile allows effective bonding between mortar layers. In fact, the inability of the inorganic matrix to penetrate among the inner filaments of yarns would generate a plane of discontinuity in the composite material if continuous or tight mesh textiles were used, causing a lacking connection between the upper and lower mortar layers, and negatively affecting the composite response (Fazzi, Misseri, and Rovero 2023). In ACI 549.4 R-13 (2013) it is specified that the coverage area of the textile should be below 2/3, to allow for sufficient connection between the composite layers.

Regarding the geometrical configuration of the textile, spacing between yarns should not exceed 25.4 mm, according to ACI 549.4 R-13 (2013) or 30 mm, according to CNR (2018). The mortar matrix thickness should be 5 to 15 mm in case one layer of textile is embedded and should be smaller than 30 mm, in case several layers of reinforcement are embedded (CNR 2018).

The reinforcing fibre content of a textile is expressed through the equivalent

thickness t_f, defined as the ratio between the weight of the reinforcing fibres in the textile and their specific weight (CNR 2018); t_f provides the thickness the textile would have if fibres were arranged without spacing in between.

In FRCM adhered to a substrate, the matrix transfers the external actions from the support to the textile, which finally bears axial stresses through the fibre-matrix interface. Experimental evidence provided by round-robin tests, shows that the FRCM behaviour is based on the bond mechanism between the phases, causing textile-matrix relative slippage and/or textile tensile failure, as observed in direct shear tests (DST), (CNR 2014; CNR 2018; Ceroni and Salzano 2018; De Santis et al. 2018; Alecci et al. 2016; Alecci et al. 2021), direct tensile tests (DTT),(ACI 549.4 R-13 2013; CNR 2014; CNR 2018; De Santis et al. 2017a; Dalalbashi, Ghiassi, and Oliveira 2021a; Nerilli and Ferracuti 2022), independently of set-ups, and, at lower scale, yarn pull-out tests (Ghiassi et al. 2016; Dalalbashi et al. 2018; Dalalbashi, Ghiassi, and Oliveira 2021a).

The tensile behaviour of FRCM differs significantly from the one of FRP due to characteristics of the inorganic matrix, which cannot undergo the same strain level of the textile and therefore cracks before maximum load is attained. Due to the formation of multiple cracks, FRCM materials in tension also show a pseudo-ductile behaviour, which accommodates relatively large deformations before failure of the system. The pseudo-ductility of the material plays a crucial role in energy dissipation and structural safety (Barhum and Mechtcherine 2012). Another important role in the response of the material is played by the tension stiffening, i.e. the stiffening effect exerted on the textile by the uncracked portions of matrix comprised between consecutive cracks (Soranakom and Mobasher 2010a; Soranakom and Mobasher 2010b; Nerilli and Ferracuti 2022).

2.2 TESTING PROTOCOLS

2.2.1 Direct Tensile Test

Italian and American guidelines (CNR 2018; ACI 549.4 R-13 2013) envisage the performance of direct tensile tests for the design of strengthening applications with FRCMs and for certification of materials. DTTs are performed by tightening a stand-alone lamina of the composite and are intended to provide a mechanical characterisation of the material under tensile loading.

Involving the definition of the load application method, the shape of the specimen and the positioning of measuring instruments, the test set-up has a crucial role in defining the information retrieved from the test (Hartig et al. 2012; Kim 2021; Focacci, D'Antino, and Carloni 2022b). Different shapes of the specimen and gripping methods have been proposed in the literature. Regarding the specimen shape, although the rectangular coupon with constant cross-section is the most frequently employed geometry, (Arboleda et al. 2016; Lignola et al. 2017; Leone et al. 2017; Carozzi et al. 2017), also bone-shaped (or dumbbell) specimens, characterised by offsets in the plane of the reinforcement (D'Antino and Papanicolaou 2018), and waisted specimens, characterised by offsets in the plane perpendicular to the one of the reinforcement (Hegger et al. 2006) were employed. The dumbbell and waisted geometry are meant to reduce stress concentration in the transition zone between the gripping area and the free length, where the failure of rectangular specimens was frequently observed. Gripping methods for load transfer can be classified into clevis and clamping. In the clevis method, Figure 2.1a, also defined as rigid load application (Hartig et al. 2012), the load is transferred through metal plates adhered to the specimen so that the load transfer mechanism is driven by

a)

b)

c)
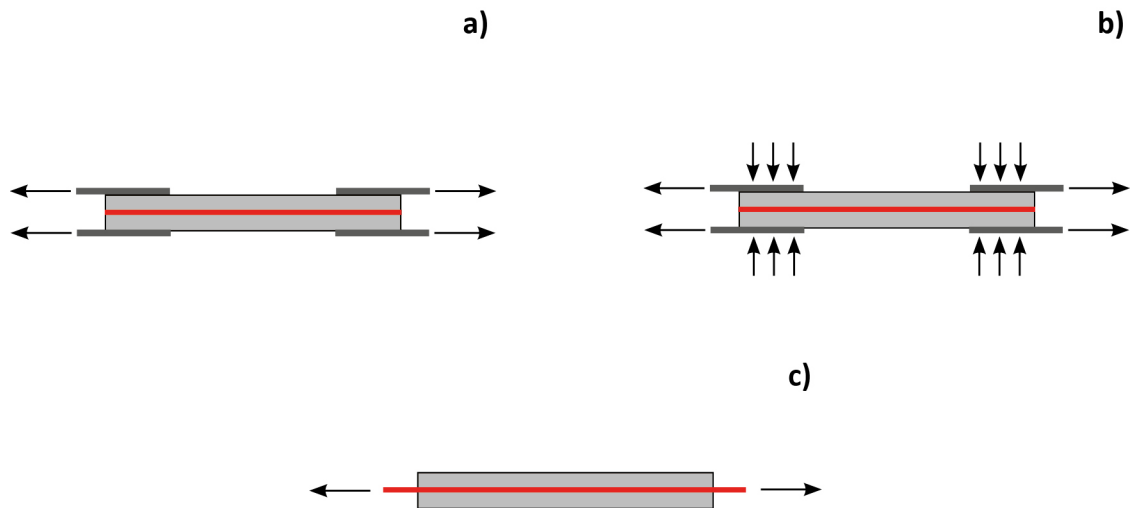
Figure 2.1: Different gripping methods for DTT: (a) clevis, (b) clamping and (c) fibre clamping.

adhesive tension and shear. In clamping, Figure 2.1b, also defined as soft clamping by Hartig et al. (2012), the load is transferred through Coulomb friction, which can be obtained by inserting the specimen in the hydraulic wedges of the testing machine (wedge clamping) or by tightening metal plates trough bolts (bolted clamping). The transverse compression exerted by the gripping apparatus must be carefully calibrated to avoid slipping between the matrix and the textile or matrix crushing. Furthermore, an even tightening level of bolts must be ensured in bolt clamping, while the specimen must be positioned into wedges with particular care to avoid damages in wedge clamping. A more recently developed load application method is fibre clamping, Figure 2.1c, which envisages that the gripping area of the specimen is free from the matrix so that the load is transferred directly to the fibre. Thereby, textile slippage in the gripping area is avoided and results can be compared to the ones of direct shear tests with fixed far-end (Bertolli and D'Antino 2022), due to the similar load application method (Ghiassi et al. 2016;
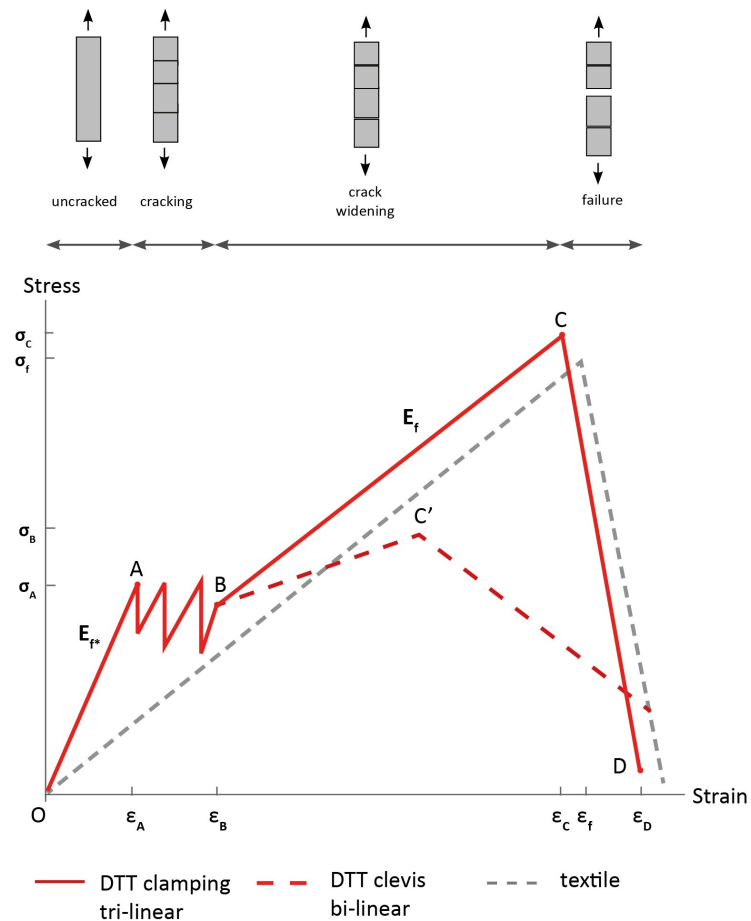
Figure 2.2: Schematization of typical stress-strain diagrams obtained from DTT

Calabrese, Colombi, and D'Antino 2019).

In the literature, different mechanical response and failure modes have been associated with different gripping methods, on the basis of observational evidence: typically in clevis grip set-up, lower peak loads are recorded and tensile failure of the fibre is not reached, since relative slips between matrix and fibre are not inhibited by the gripping apparatus (Arboleda et al. 2016; De Santis et al. 2018; Kim 2021); in wedge or bolted clamping set-ups, the specimen often fails due to tensile failure of the fibre, since the transverse compression exerted by the gripping apparatus prevents slippage of the textile within the matrix.

Each test set-ups provide specific boundary conditions influencing the mechanical response of the system. It has been suggested that, due to the different boundary conditions provided, clevis grip can be employed to evaluate FRCM behaviour in conditions of installation, while clamping can provide a complete characterisation of the composite, comprising failure of both constituent materials (Arboleda et al. 2016).

The mechanical response of DTT comprises different stages (ACI 549.4 R-13 2013; Arboleda et al. 2016; De Santis et al. 2017a; CNR 2018; Truong and Kim 2021). In the first phase, the material is uncracked and its behaviour is mainly governed by the load capacity of the matrix, providing a linear branch in the load-slip or stress-strain diagram, segment O-A in Figure 2.2. Then the first crack forms and the load is transferred at the crack location through the fibre; cracks may continue to open until saturation of the specimens is reached, point B in Figure 2.2. Once the number of cracks stabilises, the existing cracks widen and, in clamping set-ups, the response is mainly driven by the tensile strength and elastic modulus of the textile (segment B-C in Figure 2.2), while in clevis set-up the response is mainly driven by the CML properties (segment B-C′ in Figure 2.2). The cracked phase of DTT is influenced by the tension-stiffening effect, which is the stiffening action exerted on the textile by the mortar between consecutive cracks. Such effect along with cracking of the mortar is governed by the mechanical properties of the mortar and by the fibre-to-mortar bond behaviour (Ghiassi et al. 2016). Finally, failure of the system occurs due to fibre slippage or tensile failure of the fibre (Arboleda et al. 2016; D'Antino and Papanicolaou 2018) or due to a combination of both mechanisms (Arboleda et al. 2016).

According to these phases, the response of DTT can be idealised as a load-slip

diagram consisting of three consecutive segments with different slopes (Arboleda et al. 2016; CNR 2018; Truong and Kim 2021; De Santis et al. 2017a): the uncracked phase, characterised by the uncracked tensile modulus of elasticity, the crack development phase, and the crack widening phase, characterised by the cracked tensile modulus of elasticity (AC434 2013). According to (ACI 549.4 R-13 (2013)), the diagram can be further reduced to a bi-linear with a bend-over point by elongating and intersecting segments representing the uncracked and the cracked phases.

Experimental evidence showed that in some cases the crack development phase and the cracked phase can be almost indistinguishable, having similar elastic modulus; therefore, a bi-linear diagram describes all stages of the trial. In the literature, the obtainment of tri-linear or bi-linear diagrams in DTT is attributed to two main factors: the quality of bonding at the textile-matrix interface and to test set-up. Good bonding is associated with tri-linear diagrams, while poor bonding to bi-linear diagrams. Regarding the quality of bonding, in D'Antino and Papanicolaou (2018) and Truong, Lee, and Kim (2021) bi-linear and tri-linear diagrams are found within the same gripping method, by applying a coating to the fibre in order to improve bonding at the interface. In Arboleda et al. (2016) and De Santis et al. (2018) the effect of different gripping methods is investigated, highlighting that wedge clamping produces tri-linear diagrams, while clevis grip produces bi-linear diagrams. Different results are ascribed to the effect of the clamping compression which inhibits the sliding of textile within the matrix, allowing higher peak loads (D'Antino and Papanicolaou 2018). In general, it can be noted that both explanations attribute tri-linear diagrams to systems in which relative slips between matrix and textile are limited due to good bonding or to the restraining mechanical effect exerted by the gripping method.

Although experimental campaigns showed that a great variability of results can be obtained from the same FRCM system by simply changing the test set-up, international guidelines do not provide a unique indication about it for DTT. The clevis grip set-up, as described in Committee et al. (2013) is recommended by the ACI 549.4 R-13 (2013), while the clamping grip is recommended by the CSLLPP Servizio Tecnico (2019) and by RILEM (2016). The variability of results obtained by changing boundary conditions provided by the gripping method and shape of the specimen must be carefully taken into consideration, since parameters employed for design purposes should be an intrinsic property of the material and not be greatly affected by the set-up selected (Hartig et al. 2012). Focacci, D'Antino, and Carloni (2022b) further highlighted that the length of the gripping devices, the length of the specimen and the gauge length adopted to measure the deformation of the specimen highly influence the results recorded during trials, arising concern about the ability of DTT to provide reliable tensile properties.

2.2.2   Direct Shear Test

When applied as reinforcing materials to masonry or concrete structures, FRCM materials are characterised by two interfaces: the textile matrix interface and the matrix-support interface. The mechanical behaviour of these interfaces defines the failure mode of FRCM systems, which can be caused by different mechanisms:

1. cohesive debonding in the substrate (Ascione, De Felice, and De Santis 2015; De Felice et al. 2018; CNR 2018);

2. debonding at the matrix to substrate interface (Ascione, De Felice, and De Santis 2015; De Felice et al. 2018; CNR 2018);

3. debonding at the textile to matrix interface (Ascione, De Felice, and De Santis 2015; De Felice et al. 2018; CNR 2018);

4. sliding of the textile within the matrix (Ascione, De Felice, and De Santis 2015; De Felice et al. 2018);

5. tensile failure of the textile out of the matrix (Ascione, De Felice, and De Santis 2015; De Felice et al. 2018; CNR 2018);

6. sliding of the textile and cracking of the outer layer of the matrix (CNR 2018);

7. tensile failure of the textile within the matrix (Ascione, De Felice, and De Santis 2015; De Felice et al. 2018; CNR 2018).

Failure modes 1-3 are driven by debonding, which is defined as cohesive when happening in the substrate, and adhesive when happening at the textile-support or textile matrix interface (ACI 549.4 R-13 2013). Ascione, De Felice, and De Santis 2015 correlated failure modes with different shapes of the load-slip diagram: failure modes 1, 2, and 3, which are driven by debonding taking place at different interfaces, provide a diagram with a nearly flat post-linear branch, followed by a brittle failure; sliding of the textile within the matrix induces strain softening behaviour due to the progressive degradation of the bonding at the textile matrix interface; tensile failure of the textile out of the matrix determines a sudden load drop; tensile failure of the textile within the matrix, which is due to telescopic rupture of fibres and consequent slippage of the textile out of the jacket, is related to a diagram showing a sudden load reduction, followed by a further slight reduction of the load.

The assessment of the typical failure mode characterising a specific FRCM system can be obtained through direct shear tests (DST), in which the non-embedded

length of a composite system adhered to a substrate is pulled out. Through DST, Ceroni and Salzano (2018) highlighted that while, for concrete, substrate debonding is the most frequent failure mode, being experienced by 87% of the analysed dataset, tensile failure and slippage of the textile represent the prevalent failure modes when the FRCM reinforcement is applied to a masonry substrate, representing the failure mode of 35% and 44% respectively. In DAmbrisi, Feo, and Focacci (2013a) the debonding at the textile matrix interface was observed on FRCM adhered to concrete, and no substrate debonding occurred. Further experimental evidence provided by round-robin tests (Caggegi et al. 2017,Carozzi et al. 2017; De Santis et al. 2017b; Leone et al. 2017; Lignola et al. 2017) showed that the FRCM behaviour is based on the bond mechanism between the phases, causing textile-matrix relative slippage and/or textile tensile failure, as observed in direct shear tests (CNR 2014; Alecci et al. 2016; CNR 2018; Ceroni and Salzano 2018; De Santis et al. 2018; Alecci et al. 2021).

In Sueki et al. (2007), D'Antino et al. (2014), and D'Antino et al. (2018), an idealised response for DST is proposed. The typical load-slip diagram of a pull-out test on FRCM specimens shows an initial approximately linear behaviour of the material, identified by a segment with constant slope until point $A(\delta_1; P_A)$, Figure 2.3. Afterwards, micro-crackings at the fibre-to-matrix interface begin to develop and the response of the material becomes non-linear; the load value continues to increase up to point $B(\delta_2; P_B)$, Figure 2.3, at which debonding at the matrix to fibre interface begins. The load attained at point B is the maximum load transferable by the interface before the initiation of debonding and is therefore called debonding load or load-carrying capacity of the interface. For some FRCM typologies, there is a further linear segment until the peak load is reached at point $C(\delta_3; P_C)$, Figure
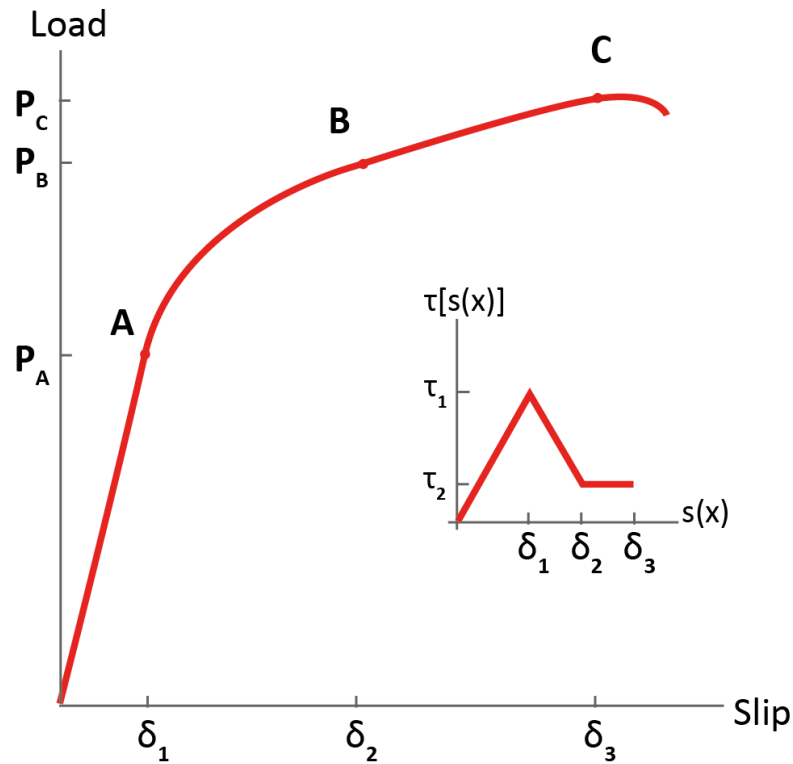
Figure 2.3: Relation between points $A(\delta_1; P_1)$, $B(\delta_2; P2)$ and $C(\delta_3; P3)$ of different load-slip diagrams and the related Cohesive Material Laws.

2.3; such further load increase is attributed to the frictional forces arising among fibre filaments and between the matrix and the fibres (D'Antino et al. 2014). It must be observed that the maximum load, P_C, is attained when the stress-transfer zone (STZ), i.e. the portion of textile-matrix interface by which stresses are transferred through bond only (no friction), reaches the free end of the specimen (D'Antino et al. 2014). Afterwards, as the slip continues to increase, load values progressively decrease until settled to a constant value, meaning that the whole textile-matrix interface is subject to frictional forces only (D'Antino et al. 2014).

Changes in the shape of the response on the load slip-curve are related to different shear transfer mechanisms at the interface, i.e. the shape of the load-slip

diagram depends on the mechanism activated by the slippage between the fibre and the matrix, which is described by a bond-slip relation (BRS), also called cohesive material law (CML). The CML summarises the phenomena involved in the shear transfer mechanism. Consequently, the slippage values registered at points A, B, and C of the load slip diagram mark the passage between different shear transfer mechanisms in the CML.

- δ_1 end of the linear elastic branch

- δ_2 end of softening branch

- δ_3 end of the frictional branch.

Furthermore, each point of the interface is subject to a specific stress transfer mechanism, depending on its slippage value, s:

- $s < \delta_1$ the point of the interface is in the linear elastic phase

- $\delta_1 < s < \delta_2$ the bonding begins to deteriorate, i.e. the point is in the softening branch of the CML

- $\delta_2 < s$, the point of the interface is debonded and experiences friction only.

Given that different points of the reinforcement experience different stress mechanisms at the same time, an effective bond length can be defined l_{eff} as the minimum length of the specimen that is needed to fully establish the STZ and bond mechanism (D'Antino et al. 2014). Consequently, for load equal to P_C, $l_{eff} = l_{STZ}$, and conversely, P_C can be reached only if the length of the specimen is at least equal to l_{eff}. As shown by Focacci et al. (2017) and reported in Section 2.4.3, a relation between the CML and the load-slip diagram can be established by equating

the work done by the fibres during the elongation and the work done by the shear stress due to fibre slip at the interface.

2.3 EFFECT OF FABRICATION TECHNIQUES

The effect of techniques adopted for the fabrication of reinforcing textiles and of the composite can significantly influence the FRCM performances. The pullout response of FRCM is indeed highly dependent on the fabric type, mixture design, and processing methods (Sueki et al. 2007).

In Hegger et al. (2006) and Peled et al. (2008) is shown that yarns fabricated with wider diameters allow better penetration of the matrix within filaments, enhancing the bond properties of the composite, while tight binding of filaments is detrimental. Also, flat cross-sections enhance the performance of the composite improving the bond between matrix and textile and a more homogeneous activation of the cross-section. Peled et al. (2008) found that the crimped and twisted geometry of yarns significantly enhances the flexural strength of the composite, compared to the straight yarn also leading to a hardening response. The crimped geometry shows better performances compared to the twisted one, having higher reinforcing efficiency in flexural testing that reflects effective bonding (Peled and Bentur 2000), although excessively wavy textile can cause splitting failure of the composite (Hartig et al. 2012).

Techniques adopted for textile fabrication, i.e. weaving, knitting, tufting, felting, braiding, or bonding (ACI 549.4 R-13 2013), determine different geometrical configurations of the reinforcement, which can affect the mechanical properties of the yarn, of the textile and the level of matrix impregnation. For instance, it was shown that the pull-out strength of knitted fabrics is between 20% to 30% lower

than the one of single yarns (Peled and Bentur 2000) since the loops generated between warp and weft direction prevent deep penetration of the matrix among filaments (Peled et al. 2008). Also, fabrics made of bundles with small diameters and large loop sizes proved to be more efficient in developing a good bond with the matrix. This is due to a good penetration of the matrix between the filaments of the bundle into the fabric. On the other hand, the bonding strength is enhanced in woven fabrics, compared to the one of the single yarn due to the crimped geometry induced by the fabrication process.

Some studies also highlighted that some restraining effect on the fibre slippage is provided by yarns orthogonal to the pull-out direction at junction points between weft and warp (Peled, Bentur, and Yankelevsky 1998; Peled and Bentur 2000; Peled et al. 2008; Soranakom and Mobasher 2009; D'Antino, Calabrese, and Poggi 2020). The effectiveness of such anchoring effect is tightly dependant on the textile typology. For instance, in woven textiles, the main role of transversal yarn is in the maintenance of the crimped geometry, and the contribution of the junction points is limited (Peled, Bentur, and Yankelevsky 1998).

Different fabrication techniques were investigated to understand the effect on the textile-matrix bond quality (Peled, Sueki, and Mobasher 2006; Mobasher, Peled, and Pahilajani 2006). Besides casting, which is the most commonly used technique, pultrusion and vacuum fabrication methods were adopted to obtain better matrix impregnation of the textile. In the casting technique, after the first layer of mortar is cast, the textile is positioned and then another layer of mortar is cast to complete the jacket. In the pultrusion technique, the textile is impregnated with matrix and pressed through rotating cylinders which eliminate the excess paste, before being positioned onto the first layer of mortar. The vacuum process envisages that,

once the mixing of the matrix is completed, the fresh paste is transferred to a vacuum chamber. The pultrusion induces better impregnation of interstitial spaces between filaments in uncoated textiles, improving bond properties either in weft intersection and woven fabrics, but does not affect the performances of systems embedding coated textiles. The vacuum process is found to not be advantageous for fabric reinforcements while providing better bonding when the reinforcement is in the form of yarns.

The level of matrix penetration among fibres significantly influences the performances of the system and can also determine telescopic failure of fibres under tensile loading conditions (Peled and Bentur 1998; Banholzer 2004; Peled et al. 2008).

2.4   MODELLING

2.4.1   Analytical modelling of bond behaviour

The perfect interface and the cohesive interface approaches are the main analytical models based on equilibrium conditions employed for modelling the pull-out problem. The perfect interface model envisages displacement continuity at the interface, i.e. no relative slip between matrix and textile is allowed. Since the constituent materials of the composite are considered perfectly adhered to each other, the perfect interface model is suited for fibre-reinforced polymers, where the textile-matrix interface does not represent the weak joint. In the cohesive interface approach, a thin inter-phase, i.e. a transition zone with mechanical properties different from the ones of the composite constituent materials is considered to exist between the matrix and the fibre. The formation of such an inter-phase is caused by the wall effect and local bleeding, which prevent appropriate packing of aggre-

gates around the embedded fibre so that a porous transition zone forms (Bentur, Gray, and Mindess 1986; Igarashi, Bentur, and Mindess 1996).

The mechanical behaviour of the inter-phase can be described as the difference between the deformation in the fibre and in the matrix, on the basis of its different stiffness from adjacent materials. Due to its negligible thickness, the inter-phase is usually idealised as a zero-thickness surface, i.e. an interface, and is described by a cohesive material law (CML), also called cohesive zone model (CZM) or bond-slip relation (BSR), which relates fibre-matrix slips and shear stresses. The fictitious reduction of the inter-phase to an interface introduces in the model the possibility of displacement discontinuity between fibre and matrix. Within this framework, the CML can be regarded either as a constitutive property of the inter-phase or as a law summarising the shear transfer mechanism taking place at the textile-matrix interface.

The shape of the CML depends on the resisting mechanisms activated at the interface by fibre tightening (adhesion, debonding, friction, etc.) and any combination of matrix and textile can theoretically provide a specific CML: in Zastrau, Richter, and Lepenies (2003) a tri-linear law, based on the assumption of adhesion, failure and friction is considered; in Sueki et al. (2007) the bond behaviour is described by a tri-linear function in terms of a linear elastic adhesion, static friction and dynamic friction; in Banholzer, Brameshuber, and Jung (2005) a multi-linear piecewise function is considered; in Colombi and D'Antino (2019) an elastic-brittle bond behaviour, with frictional ending plateau is assumed; in Misseri, Rovero, and Galassi (2021) four tri-linear cohesive material laws are selected and investigated to understand their suitability with different FRCM systems. Although different shapes of the CML are assumed, in Zastrau, Richter, and Lepenies (2003),

Sueki et al. (2007), Hartig, HäuSSler-Combe, and Schicktanz (2008), Soranakom and Mobasher (2009), Colombi and D'Antino (2019), and Misseri, Rovero, and Galassi (2021) a constant ending branch is assumed to describe a frictional resisting mechanism, considered as a distinctive trait of FRCM pull-out behaviour.

Since the CML is unknown *a priori*, a calibration of parameters defining it has to be carried out directly from measurements on experimental tests, or indirectly, through interpretation of the experimental load slip diagram obtained. In the direct calibration, considerable difficulties are encountered, since the shear transfer mechanism takes place at the internal interfaces of the composite and the embedding matrix prevents the recording of reliable measurements of fibre slippage through strain gauges: strain gauges embedded in the composite with the textile are subject to debonding due to shear stress concentrations caused by the matrix interlocking effect (Carloni et al. 2015; Sneed, D'Antino, and Carloni 2014); when strain gauges are applied to the fibre after casting, through slots into the matrix, the concentration of stresses at the edges of the slot may affect the measurements of fibre strain (Sneed, D'Antino, and Carloni 2014; D'Antino et al. 2014). Therefore sufficient experimental evidence about the CML is not yet available. The indirect calibration, also defined as back-calibration, represents a viable option to overcome issues involved in the direct approach, through the analytical fitting of experimental curves.

Given the difficulties of direct calibration of the CML and that indirect calibration is pursued, the analytical problem of modelling the FRCM bond behaviour becomes twofold, consisting of two complementary problems (Naaman et al. 1991; Banholzer, Brameshuber, and Jung 2005; Banholzer, Brameshuber, and Jung 2006; Focacci et al. 2017), since a CML is needed for the implementation of models and

the same CML has to be back-calibrated from experimental results. The primal or direct problem consists in the prediction of the load slip diagram (GLS), and implies the assumption of a known relation CML: $\tau(s) \to P$. The dual or inverse problem retrieves a CML through the analytical fitting of experimental results: $P \to \tau(s)$.

2.4.2 The direct problem: prediction of the load slip diagram

For the prediction of the load slip diagram, the assumptions on the constituent materials of the composite system envisage that each yarn of the mesh textile is equally tightened and that the fibre yarn is homogeneous and linear elastic. In this framework, the effect of the mesh spacing and of transverse filaments is neglected, hence, the textile mesh behaviour is n_y times that of the yarn, with n_y number of yarns. Matrix is assumed rigid with limited tensile strength. Dimensionless textile-matrix interface is assumed to follow a tri-linear CML with the initial branch starting from zero slip at zero stress and ending frictional branch:

$$\lambda[s(x)] = \begin{cases} \frac{\tau_1}{\delta_1} s(x) & 0 \leq s(x) \leq \delta_1 \\ \frac{\tau_1 - \tau_2}{\delta_1 - \delta_2} \left(s(x) - \delta_2 \right) + \tau_2 & \delta_1 \leq s(x) \leq \delta_2 \\ \tau_2 & \delta_2 \leq s(x) \leq \delta_3 \end{cases} \tag{2.1}$$

A mono-dimensional model is considered representative of the problem, and the equilibrium of an infinitesimal portion of the composite between two cross-sections spanning dx can be written as

$$d\sigma_f(x) \, A = 2\tau[s(x)] \, \psi \, d_x \tag{2.2}$$

where t_f and b_f are the textile equivalent thickness and width. Considering that $\sigma(x) = \varepsilon_f(x) \, E_f$, the equilibrium equation becomes:

$$d\varepsilon_f(x) \, E_f \, b_f \, t_f = 2 \, b_f \, \tau[s(x)]dx \tag{2.3}$$

For the compatibility relation, it is also known that $s'(x) = \varepsilon_f(x)$. Therefore, Equation 2.3 yields

$$s''(x) \, E_f \, b_f \, t_f = 2 \, b_f \tau[s(x)]dx \tag{2.4}$$

$$s''(x) = \frac{2}{t_f \, E_f} \tau[s(x)] \tag{2.5}$$

Equation 2.5 provides the values of the slip law $s(x)$ along the reinforcement, once a CML is given.

Since a tri-linear CML is here selected, the general solution of the interface problem provided by Equation 2.5 must be specialized for each segment of the load-slip diagram, enforcing appropriate boundary and continuity conditions.

For the linear elastic branch of the load-slip diagram, i.e. segment O-A in Figure 2.3, the equation of the linear elastic branch of the CML is inputted into the general solution, yielding

$$s''(x) = \frac{2}{t_f \, E_f} \frac{\tau_1}{\delta_1} s_1(x) \tag{2.6}$$

Setting coefficient $\chi^2 = \frac{2 \, \tau_1}{t_f \, E_f \, \delta_1}$, the above equation becomes

$$s''(x) = \chi^2 \, s_1(x) \tag{2.7}$$

The boundary conditions enforce that the deformations for s=0 are null and that the displacement in L is equal to δ_1:

$$\begin{cases} s1''(x) = \xi 2 \\ s'(0) = 0 \\ s_1(L) = \delta_1 \end{cases} \tag{2.8}$$

providing the following solution

$$s_1(x) = \delta_1 \text{sech}(\chi L) \cosh(\chi x) \tag{2.9}$$

For sufficiently long embedded lengths, after the maximum shear stress τ_1 is attained, the loaded end begins to enter the softening phase of the CML; in this phase part of the reinforcement, with legth 0-a is still in the elastic phase, while L-a is in the softening stage. For the part in the elastic phase Equation 2.9 becomes:

$$s_1(x) = \delta_1 \text{sech}(\chi a) \cosh(\chi x) \tag{2.10}$$

For the part in the softening stage, boundary conditions enforce continuity of slip and strains at point $x = a$ and the solving system becomes

$$\begin{cases} s_2''(x) + \xi^2 s_2(x) = \zeta \\ s_2(a) = \delta_1 \\ s_2'(a) = s_1'(a) \end{cases} \tag{2.11}$$

where, $\zeta = \frac{2}{E_f t_f} \frac{\delta_2 \tau_1 - \delta_1 \tau_2}{\delta_2 - \delta_1}$ and $\xi = \sqrt{\frac{2}{E_f t_f} \frac{\tau_1 - \tau_2}{\delta_2 - \delta_1}}$ and the solution yields:

$$s_2(x) = \frac{1}{\xi^2}(\zeta \sec(a-x)\xi) - \delta_1\xi\chi\tan((a-x)\xi)\tanh(a\chi) + \delta_1\xi^2 - \zeta) \qquad (2.12)$$

When the part of the reinforcement close to the applied load enters the frictional phase, point c separates where the response of the material is driven by the frictional and softening branch of the CML. Enforcing strain continuity and that the slip for $s = c$ is equal to δ_2, the solving system becomes:

$$\begin{cases} s_3''(x) = \eta \\ s_3'(c) = \delta_2 \\ s_3'(c) = s_2'(c) \end{cases} \qquad (2.13)$$

where $\eta = \frac{2\tau_2}{E_f t_f}$ and the solution is provided by:

$$s_3(x) = \frac{\eta(c-x)^2}{2} - s_2'(c)(c-x) + \delta_2 \qquad (2.14)$$

2.4.3   The inverse problem: indirect calibration of a tri-linear CML

The indirect calibration of a CML typically consists of three phases Zou, D'Antino, and Sneed 2021: first, a CML with a pre-defined shape, which is described by a series of unknown parameters is assumed; then the solution for the bond behaviour of the composite is found with the assumed CML; finally, the unknown parameters defining the CML are calibrated by finding the best numerical fitting of experimental results. Different shapes of the CML can be considered, and the one providing a closer estimation of experimental results is selected.

Although different procedures for the back-calibration of a CML have been pro-

posed in the literature (Naaman et al. 1991; Banholzer, Brameshuber, and Jung 2006; Grande and Milani 2021), the procedure presented in Focacci et al. (2017), and employed also in Rovero, Galassi, and Misseri (2020), is hereafter reported. The calibration relies on the interpretation of load slip diagrams obtained from direct shear tests.

In case a tri-linear CML is assumed, the typical load-slip diagram of a pull-out test on FRCM specimens shows an initial linear behaviour, corresponding to the phase in which all points of the domain are in the ascending branch of the CML, identified by a segment with a constant slope, until point $A(\delta_1; P_1)$. Afterwards, the response of the system becomes non-linear due to the onset of the debonding process, causing a progressive stiffness decrease in the response, due to the fact that some points of the domain are in the descending branch of the CML. In this phase, load value continues to increase up to point $B(\delta_2; P_2)$. When the FRCM system is sufficiently long, a further linear segment can be recorded before reaching peak load at point $C(\delta_3; P_3)$. The debonding propagates after peak load until involving the entire length of the specimen and causing the fibre to slip dynamically, Fig.2.3.

Each point of the interface is subject to one of the resisting mechanism, depending on slippage value s:

1. for $s < \delta_1$, the point of the interface is in the linear elastic phase;

2. for $\delta_1 < s < \delta_2$, the bonding between the matrix and the interface begins to deteriorate;

3. for $\delta_2 < s < \delta_3$, the interface is debonded, but its sliding is resisted by frictional resisting forces.

Since changes in the shape of the load slip diagram reflect the activation of different shear transfer mechanisms that are described in the cohesive material law, a relation between the CML and the load slip diagram can be established. The slip values defining the branches of the CML can be retrieved from points A, B and C so that δ_1 marks the end of the linear elastic branch and the onset of debonding, δ_2 marks the end of debonding and the onset of friction, and δ_3 marks the end of the frictional branch. Provided that the area underneath the CML represents the fracture energy needed for the crack to propagate, G_f, (Focacci et al. 2017), the values of peak shear stress τ_1 and frictional shear stress $\tau - 2$ are obtained equating the work done by the fibres during the elongation and the work done by the shear stress due to fibre slip at the interface:

$$n\, b_f\, t_f\, E_f \int_0^x \left(\int_0^{\varepsilon_f(x)} \varepsilon_f d\varepsilon_f \right) dx = 2\, n\, b_f \int_0^x \left(\int_0^{s(x)} \tau(s)\, ds \right) dx \qquad (2.15)$$

where, n is the number of yarns in the fibre, b_f is the width of each yarn, t_f is the equivalent thickness of the yarn, ε_f is the strain of the fibre, E_f is the fibre elastic modulus and $\tau(s) = \tau[s(x)]$ is the local bond-slip relation, i.e. CML. The origin of the reference system is set at the free end of the composite. For $x = L$, and given that the fracture energy that is equal to the area underneath the CML at corresponding points is given by

$$\int_0^{s(x)} \tau(s)\, ds = G_i \qquad (2.16)$$

Equation 2.15 becomes

$$E_f \, b_f \, t_f \int_0^{\varepsilon(x)} \varepsilon \, d\varepsilon = 2 \, b_f \, G_i \tag{2.17}$$

$$E_f \, b_f \, t_f \, \frac{\varepsilon^2}{2} = 2 \, b_f \, G_i \tag{2.18}$$

$$E_f \, t_f \frac{\varepsilon^2}{2} = 2 \, G_i \tag{2.19}$$

$$\varepsilon^2 = (4 \, G_i)/(E_f \, t_f) \tag{2.20}$$

$$\varepsilon = 2 \sqrt{\frac{G_i}{E_f \, t_f}} \tag{2.21}$$

Substituting $\varepsilon = \frac{P_i}{b_f \, t_f \, E_f}$ in the former equation, the equation for the load at a generic point is obtained:

$$P_i = 2 \, n \, b_f \, \sqrt{E_f \, G_i \, t_f} \tag{2.22}$$

In the case of a tri-linear CML, the value of fracture energy expressed by Equation 2.16 for points A and B becomes:

$$G_A = \int_0^{\delta_1} \left(\frac{\tau_1}{\delta_1} \right) s(x) \, ds \tag{2.23}$$

$$G_A = \frac{\tau_1 \, \delta_1}{2} \tag{2.24}$$

$$G_B = \int_0^{\delta_1} \left(\left(\frac{\tau_1 - \tau_2}{\delta_1 - \delta_2} \right) [s(x) - \delta_2] + \tau_2 \right) ds \qquad (2.25)$$

$$G_B = \frac{1}{2} (\delta_2 - \delta_1)(\tau_1 + \tau_2) + \frac{\tau_1 \, \delta_1}{2} \qquad (2.26)$$

Inputting G_A and G_B in Equation 2.16 and rearranging, the expressions providing the values of the shear stress at the matrix-fibre interface can be obtained:

$$\tau_1 = \frac{P_1}{2n^2 b_f^2 \, E_f \, t_f \, \delta_1} \qquad (2.27)$$

$$\tau_2 = \frac{\delta_2 \, \tau_1}{\delta_1 - \delta_2} - \frac{P_B^2}{2n^2 b_f^2 \, E_f \, t_f \, (\delta_1 - \delta_2)} \qquad (2.28)$$

The slips, δ_1 and δ_2 and the shear stress values, τ_1 and τ_2, defining the CML are therefore determined.

2.4.4 Direct shear test

As far as concerns analytical modelling of DST, several studies, e.g. DAmbrisi, Feo, and Focacci (2013a), DAmbrisi, Feo, and Focacci (2013b), Carozzi et al. (2016), Colombi and D'Antino (2019), and Rovero, Galassi, and Misseri (2020), are based on the explicit solution of the differential problem based on the balance condition of an infinitesimal portion of the composite and retrieve the load slip diagram assuming a rigid matrix and support, and a linear elastic textile. In Grande et al. (2018) an analytical model for DST is developed relying on the balance equation of an infinitesimal portion of the fibre and of the upper mortar layer. Assumptions envisage that the lower mortar layer and the support are rigid, the upper matrix

layer is only axially deformable, and the fibre-matrix interface has a zero thickness and is only shear deformable. Displacements of the upper mortar layer and of the textile are therefore expressed in terms of slip of the upper and lower interfaces. Linear elastic consecutive laws are assumed for the fibre and the mortar matrix. In Calabrese, Colombi, and D'Antino (2019), an analytical solution for the bond behaviour of FRCM, using an energy approach is proposed, assuming a rigid softening CML. The snap-back phenomenon is also modelled, although it is clearly stated that there is no experimental evidence from FRCM tests showing it. The effect of the CML shape variation on the response of DST is investigated in Misseri, Rovero, and Galassi (2021), Colombi and D'Antino (2019), and Focacci et al. (2017). In Zou, D'Antino, and Sneed (2021), the authors investigate different bond-slip relations on single lap single shear tests, through a similar finite difference model. In order to capture the snap-back phenomenon, an arc length iteration is carried out, and the solution approach consists of two stages: a displacement control procedure up to peak load, and a load-control procedure until failure. In Bilotta and Lignola (2021) a finite difference model is developed to interpret the bond behaviour of a single bundle embedded in mortar matrix and adhered to a support. A non-linear constitutive law, showing delayed stiffness activation is assumed for the yarn in order to account for possible uneven tightening levels of the reinforcement during installation

Modelling DST through a finite element (FE) approach is found in Grande and Milani (2018), where authors consider a 1D model composed of linear and non-linear spring elements to account for the limited tensile strength of the mortar and employ a bi-linear CML with no frictional plateau. Detailed bi-dimensional modelling of DST through commercial FE codes has been proposed, e.g., Razavizadeh,

Ghiassi, and Oliveira (2014). In Carozzi, Milani, and Poggi (2014) authors employ a simplified 1D analytical model and a 3D rigid-elements with non-linear interfaces FE model. A different approach, which considers the minimization of incremental energy and internal damage variables, is envisaged by Donnini, Lancioni, and Corinaldesi (2018) within a 2D FE environment.

2.4.5 Direct tensile test

Concerning modelling of DTT, in HäuSSler-Combe and Hartig (2007) and Hartig, HäuSSler-Combe, and Schicktanz (2008), a detailed mechanical model, which assumes the fibre reinforcement as divided into a sleeve and a core zone and includes also yarn waviness and defect effects, is implemented into a FE environment considering parametric investigations on the fibre stress distribution and global stress-strain diagrams. In Hartig et al. (2012), the model is further improved regarding the load application to the system through bar elements representing the gripping device. All materials are assumed linear elastic and bond elements acting as shear springs are used to define the interface between bar chains representing steel tabs, matrix, external sleeve, and inner core of the fibre. The effect of perfect, good or poor inner core is evaluated. In Mobasher, Pahilajani, and Peled (2006), the composite laminate theory is employed in an incremental analytical procedure to model the uniaxial tensile response. The FDM is employed in Soranakom and Mobasher (2010a) and Soranakom and Mobasher (2010b) for DTT assuming delayed stiffness activation for the matrix textile and the presence of added axial springs to simulate the presence of transverse filaments. The model developed in Soranakom (2008) and presented in Soranakom and Mobasher (2010a) does not address the uncracked phase and envisages a load control procedure. In Focacci,

D'Antino, and Carloni (2020), the equilibrium problem of a continuous domain assuming both mortar and textile deformability, is solved through a system of differential equations. Mortar is assumed to have a linear elastic constitutive law and an exponential traction-separation law. The assumptions foresee the formation of cracks in a symmetric simultaneous development. Since boundary conditions change between gripped areas and free gauge length, and after the formation of each crack, the solution is found along sub-portions; the model is further improved by including several textile layers and different DTT set-ups, including transverse load distribution in the clamped set-up (Focacci, D'Antino, and Carloni 2022a; Focacci, D'Antino, and Carloni 2022b). In Focacci, D'Antino, and Carloni (2022b) it is experimentally and numerically shown that the change in the reference length for the definition of strains in DTT affects the result and hence should be carefully assumed for design purposes. In Fazzi et al. (2022) and Fazzi, Misseri, and Rovero (2023) the authors present an advancement of the FDM of Soranakom and Mobasher (2010a) concerning the condition of load application in the uncracked state of the DTT. The finite element model presented in Nerilli, Marfia, and Sacco (2020), as an advancement of Mobasher, Pahilajani, and Peled (2006) is aimed at reproducing the mechanical behaviour in tensile tests of a representative unit cell far from the clamped areas. To understand the shear behaviour of the composite, a three-layer laminate geometry is assumed, and the analysis is carried out in the 2d small strain regime. Nerilli, Marfia, and Sacco (2021), considers also non-local effects in the strains. In Grande and Milani (2020) a finite difference mono-dimensional model, accounting for the mortar cracking and debonding at the interface, is developed for the tensile behaviour of FRCM laminas. The domain is subdivided into a mesh and each element is considered constituted by 6 nodes

connected by two sets of springs, representing constituent materials and interface behaviour. Linear springs are assumed for the matrix and textile, while non-linear zero-length springs are assumed for the interfaces. The wide FEM investigation reported in Bertolesi et al. (2014) accounts also for the non-perfect alignment of the textile.

CHAPTER 3

Proposed Model

3.1 PROBLEM STATEMENT

The literature review carried out in Chapter 2 highlighted that the mechanical response of FRCM materials in direct shear tests (DST) and direct tensile test (DTT) is mainly driven by the shear transfer mechanism at the textile-to-matrix interface: the tensile load, applied at the textile free-end in case of DST, Figure 3.1a, or along the gripped length of the specimen, in case of DTT, Figure 3.1b, induces relative slips between the textile and the matrix which activate bond resisting stress at the interface. It also emerged that modelling of the stress-transfer mechanism can be achieved through an analytical framework by imposing the balance condition of an infinitesimal segment of length dx, Figure 3.1d:

$$AE \ d\epsilon(x) = \tau \left(s(x) \right) \psi \ dx \tag{3.1}$$

in which A and E are the fibre cross-sectional area and Young modulus of the textile; $\tau \left(s(x) \right)$ is the shear bond stress, function of the slip, $s \left(x \right)$; $d\epsilon(x)$ is the strain increment of the textile, and ψ is the yarn perimeter. Equation 3.1, for stress-strain compatibility, i.e. $\epsilon(x) = ds(x)/dx$ becomes:

$$\frac{d^2 s(x)}{dx^2} = \psi/(AE) \ \tau \left(s(x) \right) \tag{3.2}$$

The non-linear 2nd order differential equation expressed by Equation 3.2, can be solved once appropriate boundary conditions and a CML are provided, as seen in the definition of the direct problem in Section 2.4.2.
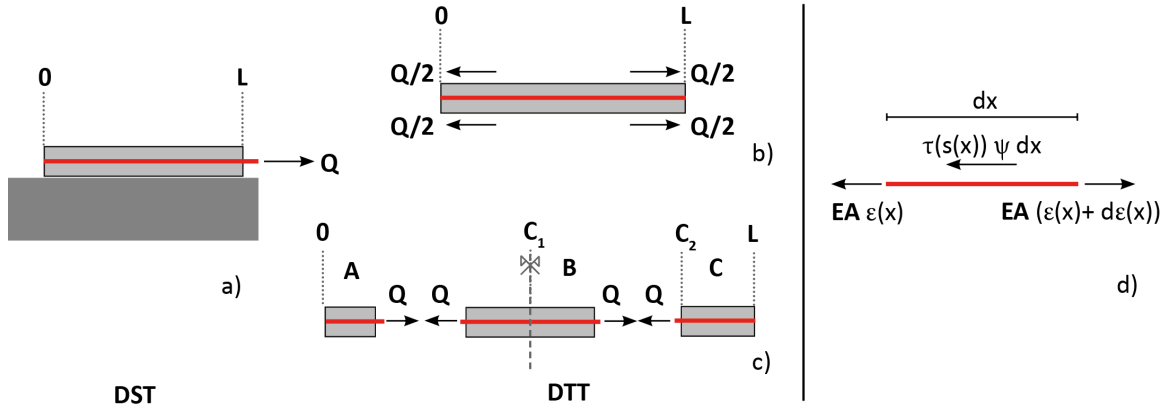
Figure 3.1: Conceptual model of: DST (a), uncracked DTT (b) and cracked DTT (c); equilibrium of the reference infinitesimal portion (d).

The slip value $s(x)$ in Equation 3.1 and 3.2 is given as the difference of relative displacements between matrix and textile:

$$s(x) = u_f(x) - u_m(x) \tag{3.3}$$

where u_f and u_m are the displacements of textile and matrix respectively. For most FRCM materials in which one or two layers of textile are embedded, the axial stiffness of the matrix is several orders of magnitude higher than the one of the fibre (Focacci, D'Antino, and Carloni 2022b). Therefore, unless in the case of high reinforcing ratios, matrix rigidity can be reasonably assumed, implying that the fibre-matrix displacement coincides with the one of the fibre, i.e.

$$s(x) = u_f(x) \tag{3.4}$$

The problem of the shear stress transfer mechanism can be approached numerically by approximating the involved derivative through the Finite Difference Method.

3.2   THE FINITE DIFFERENCE METHOD

The finite difference method (FDM) allows the numerical solution of differential problems through the approximation of function derivatives with finite differences. FDM relies on the discretisation of a continuum spatial domain in a finite number of elements, in which the solution is assumed to have constant values. The derivative of a function in a generic point internal to its domain is defined as the limit of the difference quotient of the function when the increment tends to zero.

$$f'(x_i) = \lim_{x \to 0} \frac{f(x_{i+1}) - f(x_i)}{\Delta x} \tag{3.5}$$

Equation 3.5 geometrically represents the slope of the secant line intersecting a function when the distance between the points of intersection tends to zero. In a domain discretised with constant steps of length h, if h is sufficiently small, it can be assumed $\Delta x \approx h$, and the derivative is approximated as

$$f'(x_i) \approx \frac{f(x_{i+h}) - f(x_i)}{h} \tag{3.6}$$

A better approximation is also obtained if the difference quotient is centred to the point of derivative.

$$f'(x_i) \approx \frac{f(x_{i+h}) - f(x_{i-h})}{2h} \tag{3.7}$$

This procedure allows moving from an analytical problem, governed by a system of differential equations to a numerical one governed by a system of linear equations which can be solved through straightforward matrix algebra methods. The solution provided by the FDM is in the form

$$Ax = b \tag{3.8}$$

where A is a sparse square coefficient matrix, which is related to the number of variables involved in the problem, and b is the known terms vector.

From the modelling point of view, the application of the FDM consists in implementing a model with parameters referred to each element of the discretisation: while in the analytical approach, the equilibrium conditions are written with reference to an infinitesimal portion of the composite, in the finite difference approach they are written for each element of the discretised domain.

3.3 MODEL IMPLEMENTATION

The problem stated by Equation 3.1 is addressed numerically through the FDM. To this aim, the 1D domain defined as the interval $[0, L]$, equal to the embedded length, is discretised by a series of N nodes, at constant spacing h

$$x_{i+1} - x_i = h \tag{3.9}$$

so that each N_{ith} node corresponds to x_i coordinate, with $1 \leq i \leq N$ and

$$x_N = L \tag{3.10}$$

as shown in Figure 3.2a.

The domain discretization allows converting the continuum analytical problem, where the equilibrium is referred to an infinitesimal portion of the specimen of length dx, to a numerical one, where the equilibrium can be written for a discretised element of length h. The balance condition is written with reference to the

$\pm h/2$ length preceding and following the *i-th* node, where bond stresses $\tau[s(x)]$ are assumed to have a constant value. The bond force $B(x_i)$ is associated with the x_i coordinate and depends on the slip value at that node, through the CML. Strains are constant along each step of the discretisation, i.e., in the interval between two x_i coordinates. Consistently with the shift from infinitesimal to finite length, Equation 3.1 becomes

$$AE \, \Delta\varepsilon \;=\; \tau[s(x_i)]\psi \, h \tag{3.11}$$

where $\Delta\varepsilon$ is the difference of strain values at $\pm h/2$, which is provided by

$$\Delta\varepsilon = \; \varepsilon_{i+h/2} - \varepsilon_{i-h/2} \tag{3.12}$$

The strain function is therefore approximated through the finite difference method

$$\begin{aligned} \varepsilon_{i+h/2} &= \; \frac{s_{i+1}-s_i}{h} \\ \varepsilon_{i-h/2} &= \; \frac{s_i-s_{i-1}}{h} \end{aligned} \tag{3.13}$$

and the equilibrium of a finite element becomes:

$$AE \, \frac{s_{i+1} - 2s_i + s_{i-1}}{h} = \tau[s_{(}x_i)]\psi h \tag{3.14}$$

Having expressed the first derivative of the slip through the finite difference centred at $i \pm h/2$, the forces $F(x_{i-h/2})$ and $F(x_{i+h/2})$ arising in the fibre at the $x_{i\pm h/2}$ coordinates (see Figure 3.2b) appear in Equation 3.14, being:

$$\begin{aligned} F(x_{i+h/2}) &= \; \frac{AE(s(x_{i+1})-s(x_i))}{h} \\ F(x_{i-h/2}) &= \; \frac{AE(s(x_i)-s(x_{i-1}))}{h} \end{aligned} \tag{3.15}$$
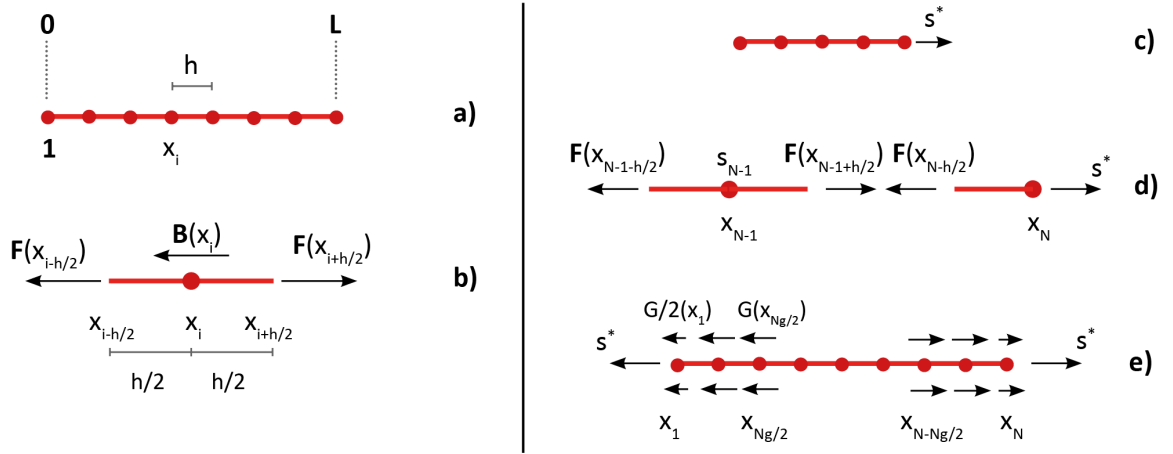
Figure 3.2: Discretization of the domain (a) and balance of the representative element (b); loading condition in displacement terms for DST (c), internal forces at loaded domain extremity (d), uncracked DTT at the *p-th* step of the incremental procedure (e).

The presence of eventual external applied forces, $Q(x_i)$, provides the following general balance condition:

$$F(x_{i+h/2}) - F(x_{i-h/2}) - B(x_i) = Q(x_i) \tag{3.16}$$

Equation 3.16 in displacement terms becomes:

$$\frac{AE}{h}\, s(x_{i-1}) - \left(\frac{2AE}{h} + \psi h \tau\big(s(x_i)\big) \right) s(x_i) + \frac{AE}{h}\, s(x_{i+1}) = Q(x_i) \tag{3.17}$$

which provides a system of non-linear equilibrium equations constituted by N equations, with N, number of nodes, in N unknowns, $s(x_i)$, node slips:

$$\mathbf{M}\,\mathbf{s} = \mathbf{q} \tag{3.18}$$

where, $\mathbf{M}^{N \times N}$ is a square, tri-diagonal matrix, and $\mathbf{s}^{N \times 1}$ and $\mathbf{q}^{N \times 1}$ are the vectors containing the unknowns and the known terms, respectively. The non-vanishing

$m_{i,j}$ coefficients corresponding to the equilibrium equations are:

$$m_{i,j} = -2AE - \psi\tau(s(x_i))h^2 \qquad 2 \leq i = j \leq N-1$$
$$m_{i-1,j} = m_{i+1,j} = AE \qquad 2 \leq i = j \leq N-1 \qquad (3.19)$$
$$m_{i,j} = -EA - \tfrac{1}{2}\psi\,\tau(s(x_i))h^2 \quad i = j = 1 \wedge i = j = N$$

i.e. in matrix form:

$$
\begin{bmatrix}
-EA - \tfrac{1}{2}\psi\,\tau(s(x_1))h^2 & AE & 0 & \cdots & 0 \\
AE & -2AE - \psi\tau(s(x_2))h^2 & AE & \cdots & 0 \\
\cdots & \cdots & \cdots & \cdots & 0 \\
0 & 0 & AE & -2AE - \psi\tau(s(x_{n-1}))h^2 & AE \\
0 & 0 & 0 & AE & -EA - \tfrac{1}{2}\psi\,\tau(s(x_n))h^2
\end{bmatrix}
$$

The different forms of the first and last coefficient of the principal diagonal of matrix **M** is connected to the length of the element, which is $h/2$ instead of h. The elements of the known terms vector, **q**, corresponding to the equilibrium of the node are $q_i = 0$, if the node is free, and $q_i \neq 0$ if the node is loaded.

For loading conditions in displacement terms, the applied force $Q(x_i)$, in Equations 3.17 and 3.16, is not assigned a priori, so it must be determined as an additional unknown. The displacement-based loading procedure envisages that one or both end nodes of the domain, e.g., node at coordinate x_N, undergo a known imposed slip, $s^* = s(x_N)$, which constitutes the loading parameter, Figure 3.2c. Hence, in the balance condition of the contiguous node, e.g., at coordinate x_{N-1}, a known part appears in the term $F(x_{i+h/2}) = F(x_{N-1+h/2}) = F(x_{N-h/2}) = \frac{EA}{h}(s^* - s(x_{N-1}))$, see Equation 3.17 and Figure 3.2d. Therefore, the effective unknown slips become $N-1$, $\mathbf{s}^{(N-1)\times 1}$, and the known part $\frac{EA}{h}s^*$ appears in $\mathbf{q}^{(N-1)\times 1}$ as the last

element of the known terms vector:

$$\frac{AE}{h} \, s(x_{N-2}) - \left(\frac{2AE}{h} + \psi h \tau \big(s(x_i) \big) \right) s(x_{(N-1)}) = \frac{AE}{h} \, s^* \qquad (3.20)$$

Simulation of characterisation tests can be obtained through an incremental procedure, which iteratively increases the applied load.

3.3.1   Problem linearization

For each *p-th* load increment, Equation 3.18 constitutes a non-linear system with as many equations as unknowns. The system non-linearity is due to the M matrix coefficients containing bond stress, $\tau[s(x_i))]$, which depends on the unknown slip at the current, *p-th*, load increment, $s(x_i)^p$. The solution of Equation 3.18 must be run iteratively with incremental steps, to achieve an estimation of the load slip diagram and, to linearize the system, it is assumed that bond stress at the *p-th* step of the iteration, p, with the value obtained at the previous step, $p - 1$.

$$\tau[s(x_i)]^p = k(x_i)^{p-1} \cdot s(x_i)^p \qquad (3.21)$$

where, $k(x_i)^{p-1}$ is the secant modulus of the CLM computed at the end of the *p-1* step:

$$k(x_i)^{p-1} = \tau[s(x_i)]^{p-1} / s(x_i)^{p-1} \qquad (3.22)$$

The accuracy of this approximation clearly relies on the dimension of the prescribed increment; smaller increments provide better approximation and an optimum increment can be defined.

3.3.2 Direct shear test

In modelling DST, the tensile capacity of the matrix is neglected because only in rare cases fibre textile debonding and slippage occur along with cracking of the external layer of the matrix (CNR 2014). The DST set-up envisages a free-end and a loaded-end, see Figure 3.2c. For a displacement-driven loading, the control parameter to be increased is the slip at an external node, e.g., N, $s(x_N) = s^*$, Equations 3.17 is employed to build the matrix, $\mathbf{M}^{(N-1)\times(N-1)}$, and the known terms vector, $\mathbf{q}^{(N-1)\times 1}$. The non vanishing $m_{i,j}$ coefficients are those of Equation 3.19 and the only non-zero element of $\mathbf{q}$ is $q_{N-1} = EAs^*$, providing

$$
\begin{bmatrix}
-EA - \frac{1}{2}\psi\,\tau(s(x_1))h^2 & AE & 0 & \cdots \\
AE & -2AE - \psi\tau(s(x_2))h^2 & AE & \cdots \\
\cdots & \cdots & \cdots & \cdots \\
0 & 0 & AE & -2AE - \psi\tau(s(x_{n-1}))h^2
\end{bmatrix}
=
\begin{bmatrix}
0 \\
0 \\
\cdots \\
AE
\end{bmatrix}
$$

For the construction of the load slip diagram, the value of s^*, increased at each step, is plotted over the internal tensile force at the loaded node, e.g., N, $F(x_{N-1+h/2}) = F(x_{N-h/2})$, multiplied as many times as the number of yarns, n_y.

3.3.3 Direct tensile test

3.3.3.1 Uncracked phase

The different experimental set-ups of the DTT correspond to different loading layouts of the domain, i.e., on the matrix along the gripped length in the clevis and clamped grip, and at fibre ends in the fibre grip set-up (Truong and Kim 2021;

Truong, Lee, and Kim 2021; Focacci, D'Antino, and Carloni 2022a; Dalalbashi, Ghiassi, and Oliveira 2021a). For clevis and clamped grip layouts, the model envisages prescribed slips at the two end nodes and unknown loads along the gripped nodes to be determined according to the prescribed slips. For the clamped-grip layout, modification of the CML for the elements of the gripped part can efficaciously represent the added transversal forces along the clamped length (Fazzi et al. 2022). In particular, the effect of the transverse compression exerted by the clamping device can be considered by increasing the value of the bond force of the CML, evaluating such effect through a proper friction coefficient. In fibre clamping, prescribed slips are defined at both end nodes and the model can be considered a composition of two mirrored DST with fixed free-end nodes.

For the clevis grip, and according to the displacement-driven loading, a prescribed slip, s^*, is imposed at the free-end nodes with an opposite sign, Figure 3.2e. The solution in terms of slip is found together with the values of the gripping forces, added as further unknowns, depending on the value s^* prescribed. The unknown gripping forces, $G(x_i)$, are defined at coordinates x_i with $1 \leq i \leq N_G/2 \wedge N - N_G/2 \leq i \leq N$, N_G, number of gripped nodes, and $N_G \subset N$, Figure 3.2e. The problem so posed shows $N - 2$ unknown slips (since $s(x_1) = -s(x_N) = s^*$), N_G unknown gripping forces, N equilibrium equations (including nodes 1 and N), and $N_G - 2$ equations to define the gripping forces. The equilibrium condition of the first, second and generic gripped nodes, respectively, are:

$$\frac{AE}{h} s(x_2) + G(x_1) = \left(\frac{AE}{h} + \frac{\psi h}{2} (\tau(s^*)) \right) s^* \qquad (3.23)$$

$$-\left(\frac{2AE}{h} + \psi h \tau \left[s(x_2) \right] \right) s(x_2) + \frac{AE}{h} s(x_3) + G(x_2) = s^* \frac{AE}{h} \qquad (3.24)$$
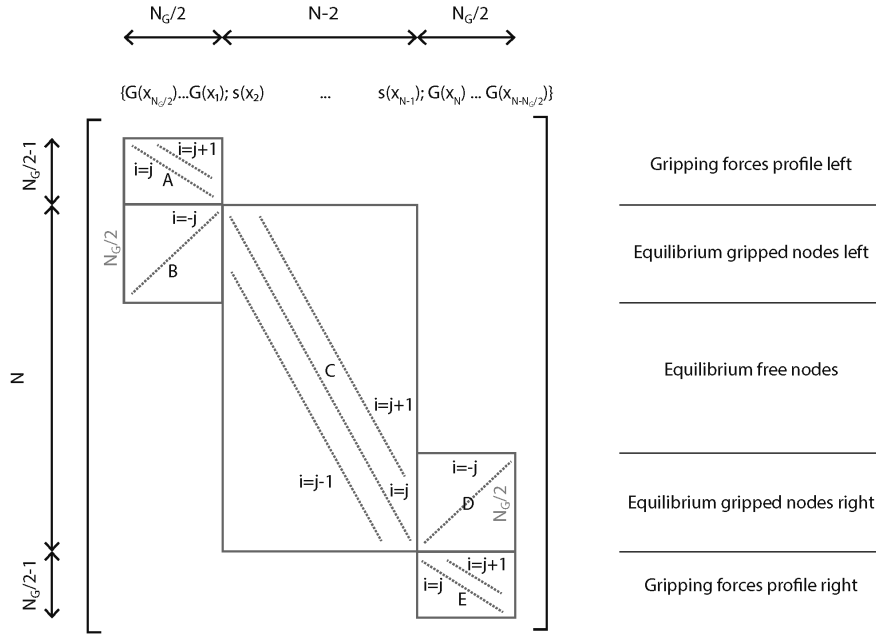
Figure 3.3: Matrix M

$$\frac{AE}{h}\, s(x_{i-1}) - \left(\frac{2AE}{h} + \psi h\tau\big[(s(x_i)\big]\right) s(x_i) + \frac{AE}{h}\, s(x_{i+1}) + G(x_i) = 0 \qquad (3.25)$$

A uniform distribution of the gripping forces requires that $G(x_i) = G(x_{i+1})$ for $2 \leq i \leq N_G/2 \wedge N - N_G/2 \leq n \leq N-1$, and $2G(x_i) = G(x_{i+1})$ for $n_y = 1, N$, since the last node is preceded or followed by an $h/2$ length element. Any other distribution of gripping forces can be implemented with appropriate relations among contiguous forces.

In view of Equation 3.18, and being the unknowns vector, $\mathbf{s}^{K \times 1}$, with $K = (N + N_G - 2)$, composed as follows (see Figure 3.2e)

$$\mathbf{s} = \Big\{ G(x_{N_G/2}); ...; G(x_1); s(x_2); ...; s(x_{N-1}); G(x_{N-N_G/2}); ...; G(x_N) \Big\} \qquad (3.26)$$

the non-vanishing coefficients of the matrix $\mathbf{M}^{K \times K}$ constitute a sparse array com-

posed of five sub-matrices organised as shown in Figure 3.3. Appropriate compo-sition of matrices $\mathbf{B}^{N_G/2\times N_G/2}$, $\mathbf{D}^{N_G/2\times N_G/2}$ and $\mathbf{C}^{N\times N-2}$ provides equilibrium equa-tions of the N nodes. Then, inclusion of matrices $\mathbf{A}^{N_G/2-1\times N_G/2}$, $\mathbf{E}^{N_G/2-1\times N_G/2}$ in the $K \times K$ space according to Figure 3.3 provides information on the gripping forces profiles. For the case of a constant load profile, the following values are assumed in the $M^{K\times K}$:

$$
\begin{aligned}
&a_{i,j} = 1 && 1 \leq i = j \leq N_G/2 - 2 \\
&a_{i,j} = 1/2 && i = j = N_G/2 - 1 \\
&a_{i,j+1} = -1 && 1 \leq i = j \leq N_G/2 - 1 \\
&b_{i,j} = -1 && N_G/2 \leq i \leq N_G - 1 \;;\; N_G/2 \geq j \geq 1 \\
&c_{i,j} = -2AE - \psi\tau(s(x_i))h^2 && N_G/2 + 1 \leq i = j \leq N + N_G/2 - 2 \\
&c_{i,j+1} = c_{i,j-1} = AE && N_G/2 + 1 \leq i = j \leq N + N_G/2 - 2 \\
&d_{i,j} = 1 && N \leq i \leq N + N_G/2 - 1; \\
&&& N + N_G - 2 \geq j \geq N + N_G/2 - 1 \\
&e_{i,j-1} = -1 && N + N_G/2 \leq i = j \leq K \\
&e_{i,j} = 1/2 && i = j = N + N_G/2 \\
&e_{i,j} = 1 && N + N_G/2 + 1 \leq i = j \leq K
\end{aligned}
\tag{3.27}
$$

Then, in the known terms vector $\mathbf{q}^{K\times 1}$, the non-vanishing elements are:

$$
\begin{aligned}
&q_{N_G/2} = -q_{N+N_G/2-1} = s^* \cdot (2AE + \psi\tau(s^*)h^2) \\
&q_{N_G/2+1} = -q_{N+N_G/2-2} = -s^*AE
\end{aligned}
\tag{3.28}
$$

The load-slip diagram for the DTT in the uncracked phase is built considering twice the value of s^*, i.e the slip at the extremity of the system, plotted over the

resultant of the gripping forces at each step of the iteration, i.e. the load transferred to the system. To determine the load level at which the first crack, c_1, forms it is assumed that the matrix force at coordinate x_i, $F_m(x_i)$, is evaluated as the difference between the external load, and the value of the force in the fibre at coordinate x_i, i.e.

$$F_m(x_i) = \sum_{i=1}^{N_G/2} G(x_i) - F(x_i) \tag{3.29}$$

When the tensile strength of the matrix, $f_t m$ is reached, the system is considered to crack.

3.3.3.2 *Cracked phase*

In the cracked phase of DTT, the domain is represented through a series of crack-separated portions, hence, new boundaries form sub-dividing the initial domain. Portions of the domain are linked by the un-bonded yarn, which must undergo the same tightening level at each crack location, corresponding to the resultant of forces transmitted at the grips. Hence, strain continuity and the same strain value must be ensured at all the internal ends of each portion. Cracks can open in any position of the domain with the exception of the gripped areas. If a homogeneous strength along the domain is assumed, cracks necessarily form symmetrically, first at grips, then, in the middle, and following, in the middle of the further sub-portions formed. Cracks can form anywhere if a random distribution of the tensile strength capacity is envisaged. The crack opens without any mode-I fracture energy dissipation and the CML does not deteriorate.

At the coordinate at which a crack forms, x_{c1}, slips at the left and right crack edges, $s(x_c^L)$ and $s(x_c^R)$, respectively, show opposite sign, and the sum of their abso-

lute value defines the crack width, w_1, which is assumed as the loading parameter and is increased at each step of the incremental procedure, Figure 3.5a.

$$w_1 = |s(x_{c1}^L)| + |s(x_{c1}^R)| \tag{3.30}$$

If one or more cracks divide the domain symmetrically, the slip at the left and right crack edges are equal, i.e. $|s(x_{c1}^L)| = |s(x_{c1}^R)|$. If a crack opens in a generic position of the domain, the parameter $\rho_1 \in [0, 1]$ (Figure 3.5a) is introduced as an unknown combination coefficient of the crack width:

$$\begin{cases} s(x_c^L) = & w_1 \rho_1 \\ s(x_c^R) = & -w_1(1 - \rho_1) \end{cases} \tag{3.31}$$

Strain continuity, requiring that the forces in the fibre at the right and left edge of a generic crack are equal, offers:

$$\frac{EA}{h}\big(s(x_{c+1}) + w(1 - \rho_1)\big) = \frac{EA}{h}\big(w\rho_1 - s(x_{c-1})\big) \tag{3.32}$$

For an N nodes domain, and a crack forming at coordinate x_{c1}, with $N_G < c1 \leq N - N_G$, there are $N - 1$ unknown slips, one unknown combination coefficient, ρ_1, $N - 1$ equilibrium conditions on the nodes (of the kind of Equations 3.16 and 3.17), and the strain continuity condition (Equation 3.32).

The elements of the unknowns vector s in Equation 3.18 for the one-crack DTT are therefore:

$$s = \left\{ s(x_1); ...; s(x_{c1-1}); \rho_1; s(x_{c1+1}); ...; s(x_N) \right\} \tag{3.33}$$

and the following coefficients of matrix $\mathbf{M}^{N \times N}$ must be substituted to the values

appearing in Equation 3.19 at the appropriate positions:

$$m_{c1,c1} = -2EAw$$
$$m_{c1-1,c1} = EAw \quad m_{c1+1,c1} = EAw \tag{3.34}$$

In Equation 3.32, the term $\frac{EA}{h}w$ is known since depends directly on w, which is the prescribed loading parameter; therefore, vector $\mathbf{q}^{N \times 1}$ is assembled with the following non-zero elements:

$$q_c = -EAw \quad q_{c+1} = EAw \tag{3.35}$$

Equations 3.18 and 3.19, in view of Equations 3.31, 3.32, 3.33, 3.34 and 3.35, provide the solution at each $p-th$ increasing value assumed by w^p.

To determine the load level at which further cracks form, the matrix tensile force at coordinate x_i is evaluated as the difference between the tensile force in the un-bonded yarn at the left or right of the existing crack, $F(x_{ci \pm h/2})$, and the tensile force at x_i. This value coincides with the sum of all bond forces comprised between x_{ci} and x_i.

If two cracks, c_1 and c_2, open at coordinate $x_{c_2} > x_{c_1}$, Figure 3.5b, a further unknown combination coefficient, ρ_2, must be introduced:

$$\begin{cases} s(x_{c2}^L) = w_1(1 - \rho_1) \\ s(x_{c2}^R) = w_1\rho_2 \end{cases} \tag{3.36}$$

where, crack widths are w_1 and $w_2 = |s(x_{c2}^L)| + |s(x_{c2}^R)| = w_1(1 - \rho_1 - \rho_2)$. The problem so posed shows $N - 2$ unknown slips, two unknown combination coefficients, ρ_1 and ρ_2, $N - 2$ equilibrium equations (of the kind of Equations 3.16 and 3.17), and

two strain continuity conditions of the type of Equation 3.32.

Assuming the presence of two cracks at the generic nodes c_1 and c_2, with $x_{c_2} > x_{c_1}$ and, as previously soecified, $N_{grip} < c_1; c_2 \leq N - N_{grip}$, the following elements of matrix **M** in Equation 3.18 must be replaced:

$$
\begin{aligned}
m_{c_1,c_1} &= -2EAw \\
m_{c_1-1,c_1} &= EAw \quad m_{c_1+1,c_1} = EAw \\
m_{c_2,c_2} &= -EAw \\
m_{c_2-1,c_2} &= 0 \quad\quad m_{c_2+1,c_2} = EAw
\end{aligned}
\tag{3.37}
$$

And the following non-vanishing elements of matrix **M** must be introduced:

$$
\begin{aligned}
m_{c_2-1,c_1} &= -EAw \\
m_{c_2,c_1} &= EAw
\end{aligned}
\tag{3.38}
$$

Also, vector **q** is assembled with the following non-zero elements:

$$
\begin{aligned}
q_{c_1} &= -EAw \quad\quad q_{c_1+1} = EAw \\
q_{c_2-1} &= -EAw \quad q_{c_2} = EAw
\end{aligned}
\tag{3.39}
$$

Equations 3.18 and 3.19, considering also 3.36, 3.37, 3.38 and 3.39, provides the solution at each increasing value assumed by w^p.

In case $x_{c2} < x_{c1}$, slips of nodes facing each crack are:

$$
\begin{cases}
s(x_{c2}^L) = w\rho_2 \\
s(x_{c2}^R) = -w(1 - \rho_1) \\
s(x_{c1}^L) = w(1 - \rho_1) \\
s(x_{c1}^R) = -w\rho_1
\end{cases}
\tag{3.40}
$$

Accordingly, the following elements of matrix **M** must be replaced:

$$
\begin{aligned}
m_{c_2,c_2} &= -EAw \\
m_{c_2-1,c_2} &= EAw \quad m_{c_2+1,c_2} = 0 \\
m_{c_1,c_1} &= 2EAw \\
m_{c_1-1,c_1} &= -EAw \quad m_{c_1+1,c_1} = -EAw
\end{aligned}
\tag{3.41}
$$

Then, the following elements of matrix **M** must be introduced:

$$
\begin{aligned}
m_{c_2,c_1} &= -EAw \\
m_{c_2+1,c_1} &= EAw
\end{aligned}
\tag{3.42}
$$

Vector **q** is assembled with the following non-zero elements:

$$
\begin{aligned}
q_{c_2} &= -EAw \quad q_{c_2+1} = EAw \\
q_{c_1-1} &= -EAw \quad q_{c_1} = EAw
\end{aligned}
\tag{3.43}
$$

Iteration of the solution to Equations 3.18, in view of Equations 3.19, 3.36, 3.37, 3.38 and 3.39, provides the solution at each increasing value assumed by w.

The solution to system configuration envisaging a higher number of cracks can be found accordingly.

3.3.4 Construction of the load-slip diagram for DTT

As seen in the previous section, the solving system of equations expressed in matrix form by Equation 3.18 must be specified to the uncracked and cracked phases of DTT through the enforcement of appropriate boundary and continuity conditions. Consequently, for a given number of cracks envisaged by the system equal to Nr_c, $Nr_c + 1$ solving systems are identified.
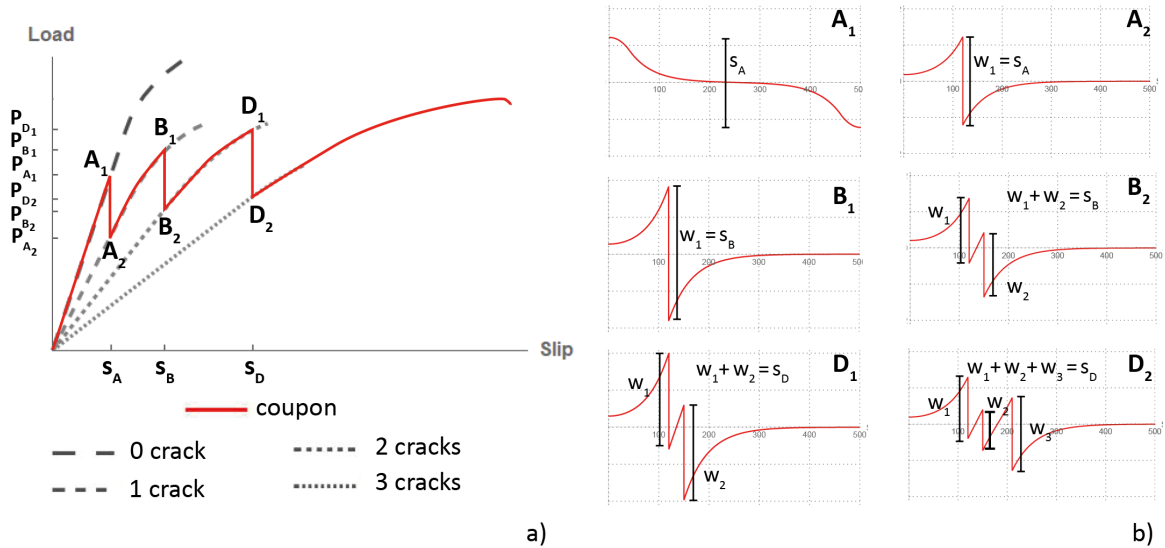
Figure 3.4: Reference load-slip diagram and related independent diagrams with cracks opening at slip values S_A, S_B and S_D (a); and corresponding slips distribution along the domain before and after each load drop (b).

Each solving system can be run independently, assuming that the model undergoes a generic phase of the cracking process from the beginning of the loading procedure, without changing configuration, i.e. neglecting the tensile strength of the matrix. The set of independent load-slip diagrams thus obtained, shown as gray dashed lines in Figure 3.4a, provide information on the stiffness of e of the system, so that the estimation of the load-slip diagram of DTT can be obtained. The brittle fracture opening triggers load drops that reconnect the independent load-slip diagrams, red continuous line in Figure 3.4a, and is bounded by the load registered at the previous phase, e.g., uncracked P_{A_1}, and the load registered for the same slip value, S_A, in the independent load-slip diagram of the following phase, P_{A_2}, Figure 3.4a.

From the numerical point of view, such result is obtained as follows: the solution specific to the uncracked phase is run by increments of the applied load until the attainment of matrix tensile strength, point A_1 in Figure 3.4, triggering
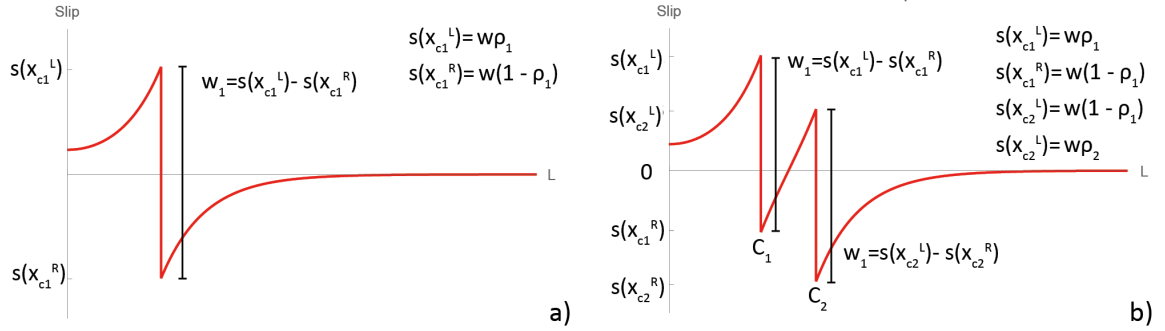
Figure 3.5: Use of distribution coefficients ρ_1 and ρ_2 for the definition of slips at the right and left tips of each crack. Slip distribution along the domain and crack width measuring: in the one-crack phase (a), at $x(c_1)$; and in the two crack phase, at $x(c_1)$ and $x(c_2)$ (b).

the opening of the first crack, c_1. The crack formed is assumed to show an initial width coinciding with the last attained global slip $w_1 = s_A$, and due to the reduced stiffness of the cracked system compared to the uncracked one, a load drop is registered. Crack width w_1 is incremented until matrix tensile strength is reached again for s_B and P_{B1} at a generic x_{c2} coordinate. The crack formed at x_{c2} is assumed to show an initial width coinciding with the last attained global slip $w_1 = w_1 + w_2$, ($B_1 - B_2$ in Figure3.4); since the values of distribution coefficients ρ_1 and ρ_2 at slip s_B are unknown *a priori*, they are retrieved by the algorithm from the independent solution of the two-crack phase and inputted in the iteration. For the phases including further cracks, the global slip value is similarly assumed as the sum of the crack widths and the load slip diagram is built according to the same procedure.

The obtained local distribution of slip, strain and bond stress attained at the end of the uncracked, one-crack, two-crack and three-crack phases are shown in Figure 3.6.

Since each crack-separated portion is subject to the same axial force, when a crack forms at the end of the gripped length, the load capacity of the system equals
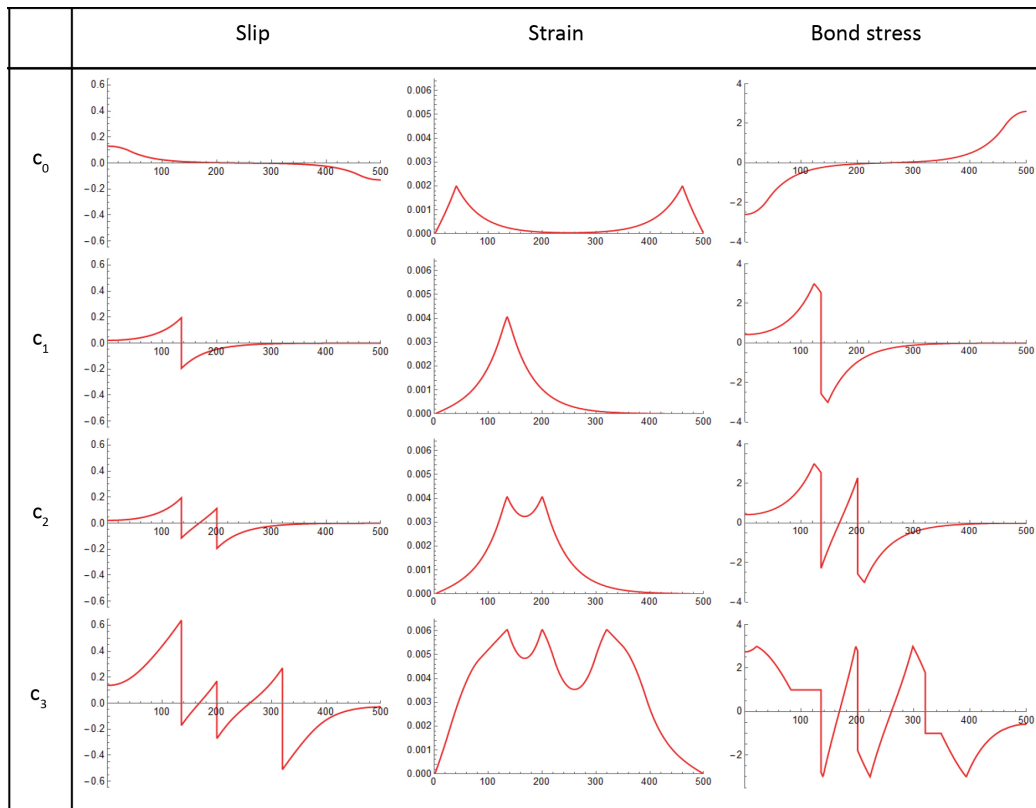
Figure 3.6: Local distribution of slip, strain, and bond stress at the end of the un-cracked (c_0), one-crack (c_1), two-crack (c_2) and three-crack (c_3) phases.

the sum of bond forces along the gripped length (Focacci, D'Antino, and Carloni 2022a). In general, for cracks opening at random coordinates, the load capacity of the system in DTT equals the maximum bond force transferable by the shortest external sub-portion, regardless of the number of cracks formed. This issue is further deepened in Section 4.3.3.

In this framework, and recalling rigidity assumptions for matrix and support, the extremity portions of the cracked DTT can be considered as two DST loaded at nodes facing the crack, while central portions can be considered as DTTs with fibre grip configuration, i.e. loaded at the extremity nodes only. Each half of the central portions of DTT can be further conceived as a DST with fixed end extremity, see Figure 3.1.

CHAPTER 4

Parametric analysis

4.1 MODEL SET-UP AND SETTING

A parametric study is conducted to verify the consistency of model response for both DTT and DST systems. Parameters defining the geometrical and mechanical characteristics of constituent materials and bond properties are considered in the analysis of both DST and DTT systems: elastic modulus of the fibre (E); yarn perimeter (ψ) for fixed cross-section (A); bond stresses (τ_1, τ_2) and slip values (δ_1, δ_2) defining the CML; tensile strength of the mortar matrix (f_{tm}), where relevant. The effect of test set-up and cracks opening at different positions is also assessed for the DTT system.

Each fibre yarn of the textile is assumed to have an elliptical cross-section, $A = \pi a \cdot b$, with a and b, major and minor ellipse semi-axes, respectively and perimeter:

$$\psi = n_y \sqrt{2\pi \frac{A(1 + \chi^2)}{\chi}} \qquad (4.1)$$

defined as a function of the ratio between semi-axes, $\chi = b/a$, to account for different yarn layouts for a given cross section. Where not differently specified, crack positions in DTT systems, of total length $L=500$mm, are fixed as follows: $x_{c1} = 100$ mm, $x_{c2} = 250$ mm, and $x_{c3} = 400$ mm. To account for the difference in clamping and clevis set-up, it is assumed that the bond stress in the gripped areas is magnified by the added frictional forces that arise due to the applied compression.

Geometrical characteristics of the DST system are: system length is $L=200$ mm, thickness including matrix, $t_m=10$ mm , width, $b=95$ mm, equivalent thickness of the textile, $t_f=0.01$ mm. The area of each yarn is, $A = (b \cdot t_f)/n_y$, where, n_y is the

number of the embedded bundles. For the DTT system, length is L=500mm, width, b=60 mm, and gripping length, L_g=40mm, thickness and fibre characteristics are the same as for DST. Mesh discretisation is set at 1-mm spacing.

Table 4.1: Parameters for the analysis: textile elastic modulus E, single yarn perimeter ψ, number of yarns embedded in the matrix, n_y; values defining the tri-linear CML: shear stress at the end of the ascending branch, τ_1, shear stress at the end of the linear softening branch, τ_2, slip at the end of the ascending branch,δ_1, slip at the end of the linear softening branch, δ_2; mortar tensile strength, f_{tm}. Parameters are increased or decreased by the coefficients reported at the beginning of each column.

		x 0.5	x 1	x 1.5	x 2
E	[GPa]	125	250	375	-
$\psi \cdot n_y$	[mm]	-	3.55	5.17	7.14
τ_1	[MPa]	1.06	2.12	3.18	-
τ_2	[MPa]	0.35	0.7	1.05	-
δ_1	[mm]	0.075	0.15	0.225	-
δ_2	[mm]	0.175	0.35	0.525	-
f_{tm}	[MPa]	0.5	1	1.5	2

Reference values of the parameters are considered, and in turn decremented and incremented by shifts of fifty per cent of their value, as reported in Table 4.1. Results of the variation of each parameter are shown in Figure 4.1 and Figure 4.7. Load-slip diagrams are reported with values normalised to the load and slip attained at the end of the linear phase, for DST, and at the formation of the first crack for DTT, by the base system, i.e. the diagram obtained with reference values of the parameter. Therefore, the reference diagram indicated with a $x1$ label, is common to all figures of DST and to all sub-figures referred to the same test set-up of DTT.
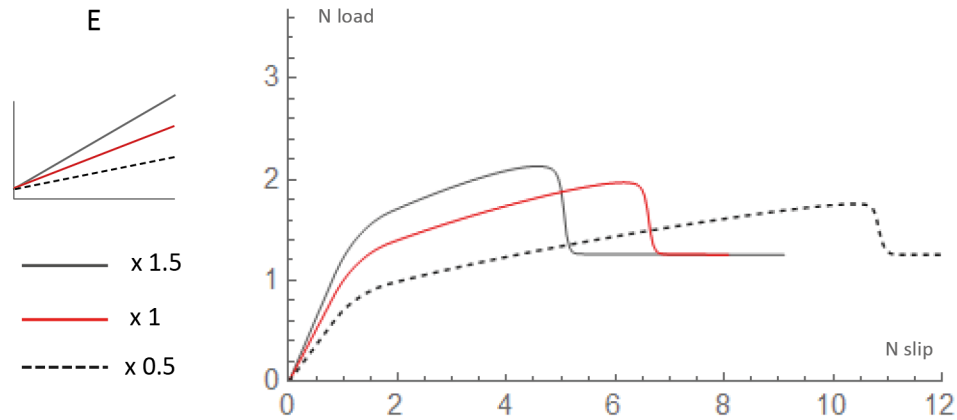
Figure 4.1: Parametric analysis of DST to the variation of the elastic modulus of the fibre E; values of the normalised load (N load) plotted against the normalised slip (N slip).

4.2 DIRECT SHEAR TEST

4.2.1 Effect of textile characteristics

As shown in the following, the parametric analysis on DTT highlights that the variation of the textile Young's modulus, induces parallel shifts of the pre-peak branch of the load-slip diagram, while variations of ψ, cause different tangent stiffnesses of the pre-peak branch.

Each 50% increase of the fibre elastic modulus E, Figure 4.1, determines approximately a 30% increase in the stiffness of the linear ascending branch of the load slip diagram. For the lowest value of E, a 68% higher displacement capacity and a 12% decrease in load capacity are recorded at peak, compared to the reference value; for the highest value of E, a 25% lower displacement capacity and an 8% increase in load capacity are recorded at peak compared to the middle value.

For a constant cross-section of the fibre, the increase in the value of perimeter, $\psi \cdot n$, Figure 4.2, i.e., greater $\chi = b/a$, see Equation 4.1, implies a wider fibre to matrix interface on which the stress transfer mechanism can be activated, thus
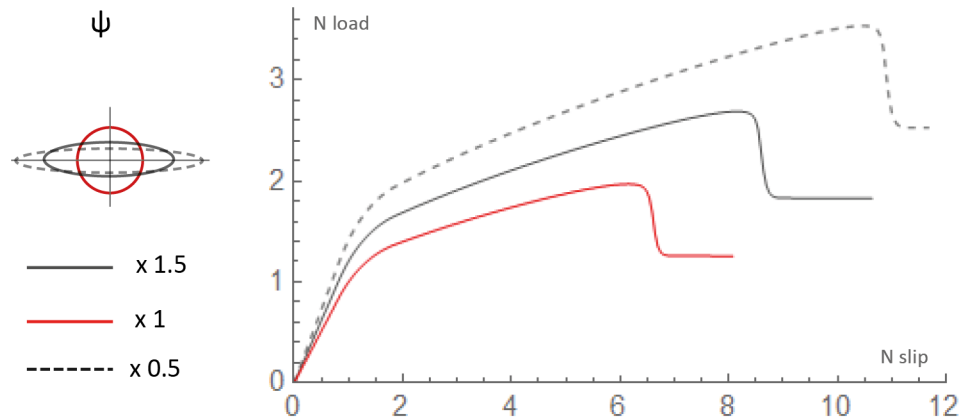
Figure 4.2: Parametric analysis of DST to the variation of the perimeter of the fibre $\psi \cdot n$. values of the normalised load (N load) plotted against the normalised slip (N slip).

producing a stiffer branch in the linear phase, higher peak load and displacement capacity of the system. For each increase of ψ value, the load and displacement capacity at the peak load are both increased by approximately 30%. It must be noted that longer perimeters determine proportionally higher ending plateaus.

4.2.2 Effect of CML properties

Variations of the CML properties are not all equally relevant to the load-slip response. The variation of the slip defining the end of the linear ascending branch of the CML, δ_1, Figure 4.3, slightly affects the stiffness of the pre-peak phase and the peak load of the diagram.

Compared to the diagram provided by the middle δ_2 value, Figure 4.4, the peak load and corresponding slip are increased by approximately 10% for the highest δ_2 and are decreased by approximately 17% for the lowest δ_2.

The variation of τ_1 is firstly performed by keeping constant the slope of the branches in the CML, Figure 4.5. Higher τ_1 values produce longer linear ascending branches of the load-slip diagram and lead to higher load and displacement
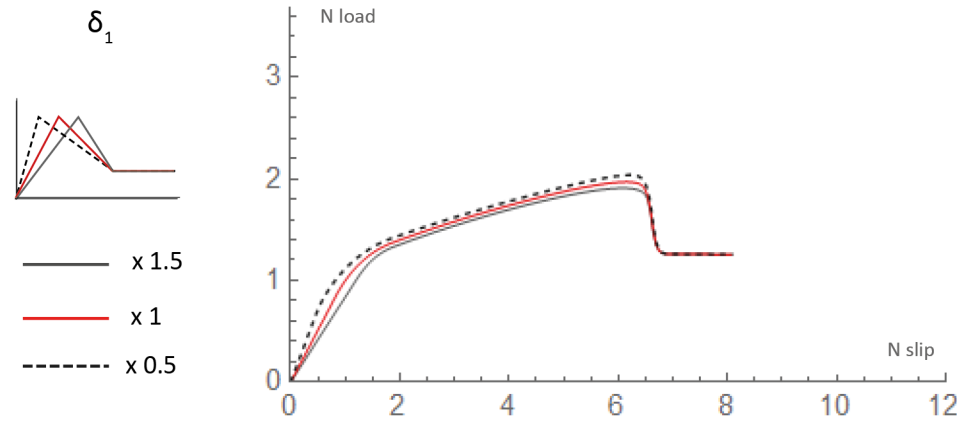
Figure 4.3: Parametric analysis of DST to the variation of slip value δ_1 defining the end of the linear ascending branch of the tri-linear CML. values of the normalised load (N load) plotted against the normalised slip (N slip).
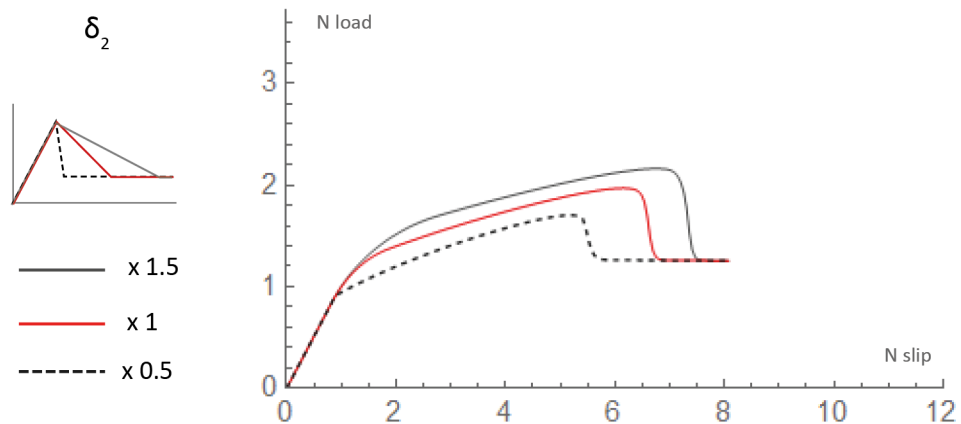
Figure 4.4: Parametric analysis of DST to the variation of slip value δ_2 defining the end of the softening branch of the tri-linear CML. values of the normalised load (N load) plotted against the normalised slip (N slip)
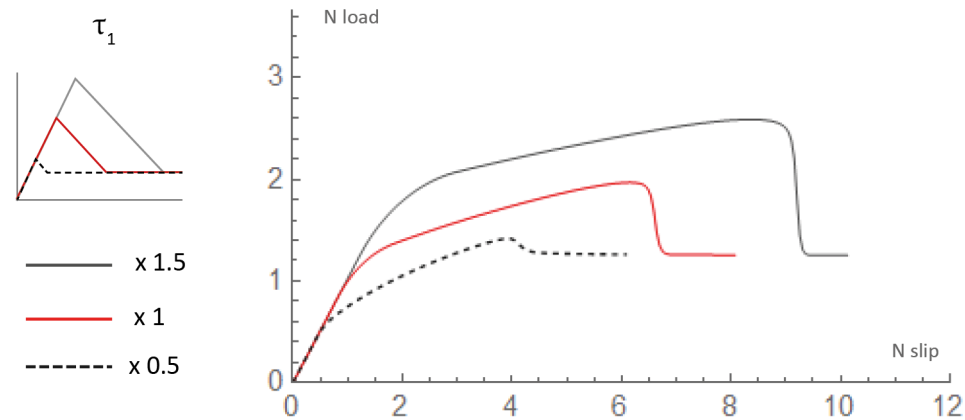
Figure 4.5: Parametric analysis of DST to the variation of peak shear stress, τ_1 with fixed ascending stiffness (varying δ_1). Values of the normalised load (N load) plotted against the normalised slip (N slip).

capacity. Compared to the middle value, the increase or decrease of τ_1 respectively induces a 31% higher or lower peak load and a 37% corresponding slip.

Changes in the value of parameter τ_1 with constant δ_1, cause different slopes of the linear ascending branch and of the softening branch of the CML, Figure 4.6. The load-slip diagram associated with the lowest τ_1 exhibits a 37% lower stiffness in the linear ascending branch, and reaches a 27% lower peak load at a 29% lower slip, compared to the middle τ_1 value. The highest τ_1 determines a 20% higher stiffness in the linear phase, while peak load and corresponding slip are 17% and 20% higher, respectively, if compared to the middle value.

Each 50% shift of the τ_2 value determines a 50% variation in the load attained in the ending plateau phase, Figure 4.7 and Figure 4.8. If τ_2 is varied without changing the slope of the softening branch in the CML, and consequently changing the δ_2 value, the highest and lowest τ_2 are associated respectively with a 21% peak load increase or decrease and a 13% slip increase or decrease. If τ_2 is varied by changing the slope of the softening branch of the CML, Figure 4.7, the highest and lowest τ_2 are associated respectively to an approximately 20% peak load increase
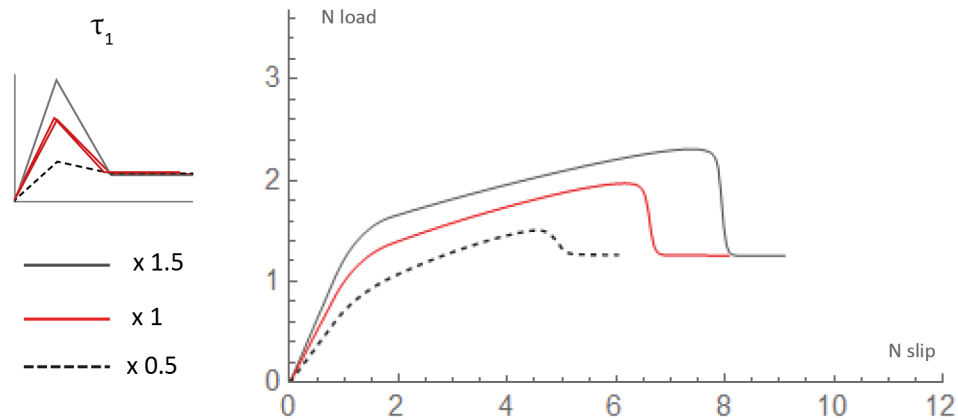
Figure 4.6: Parametric analysis of DST to the variation peak shear stress, τ_1 with changing stiffness (fixed δ_1). Values of the normalised load (N load) plotted against the normalised slip (N slip).

or decrease and 10% slip increase or decrease.

4.3 DIRECT TENSILE TEST

4.3.1 Effect of textile and mortar characteristics

Results of the parametric analysis with respect to textile and mortar characteristics are reported in Figure 4.9 and Figure 4.17, where load-slip diagrams obtained from base value parameters, red line, and their variations, gray continuous or dashed lines, are compared both for the clevis and clamped configurations. Load and slip values in all the diagrams are normalised to the values of load and slip at the end of the uncracked phase obtained for the reference curve (the red continuous curve). Hence, the reference is the same for all diagrams of the same configuration, i.e. clevis or clamping.

The increase of the elastic modulus, E, of the fibre only slightly affects the uncracked phase of the load-slip diagram, but significantly influences the crack opening process, the slope of the diagram in the cracked phase, and the peak load
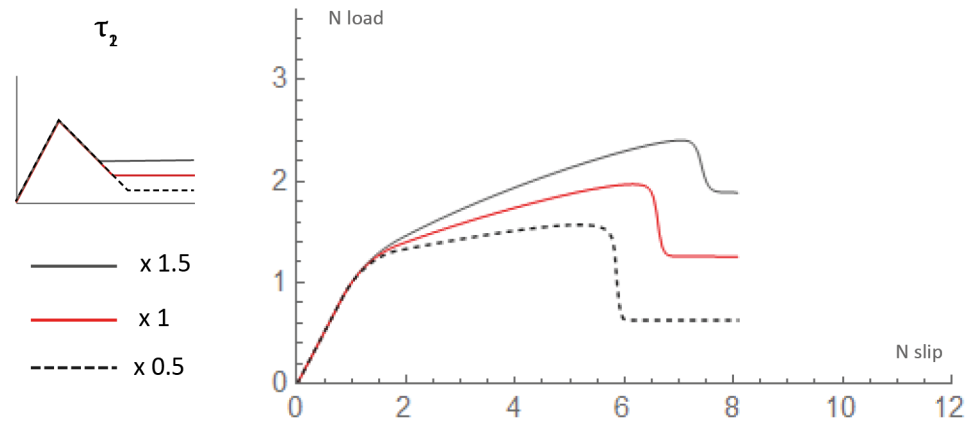
Figure 4.7: Parametric analysis of DST proposed model to the variation of the frictional stress value τ_2, with fixed softening stiffness (varing δ_2). Values of the normalised load (N load) plotted against the normalised slip (N slip).
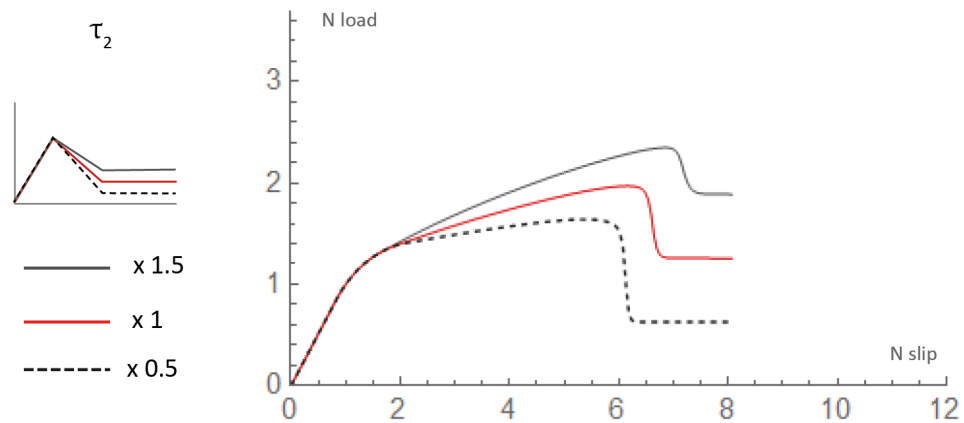
Figure 4.8: Parametric analysis of DST proposed model to the variation of the frictional stress value τ_2, with changing softening stiffness (fixed δ_2).
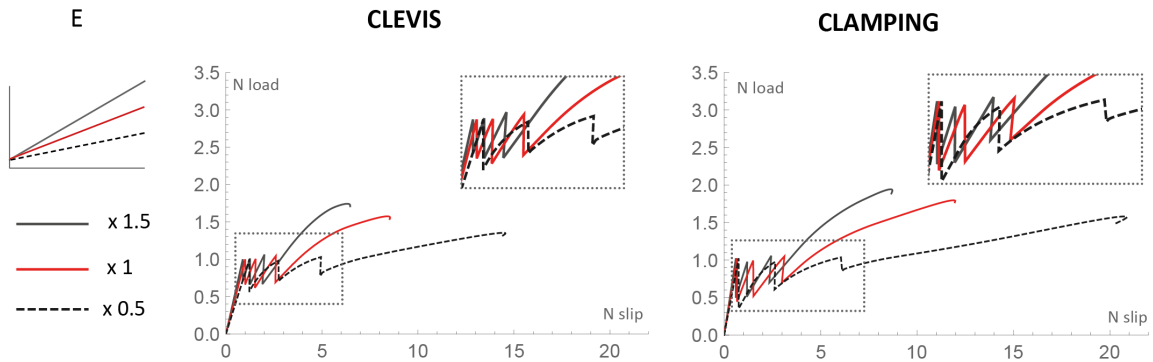
Figure 4.9: Parametric analysis of the proposed model to the variation of the elastic modulus of the fibre, E. Values of the normalised load (N load) plotted against the normalised slip (N slip).

reached, Figure 4.9. The lowest elastic modulus, provides more than 70% slip increase at peak load, both in clevis and clamping set-ups, compared to the base value, grey continuous curve, and peak load reduces up to 13%.

For a constant cross-section of the fibre, the variation of the perimeter, ψ, by variation of the ellipse major and minor semi-axes of length a and b, respectively, determines different responses in all phases of the load-slip diagram, see Figure 4.10. Longer perimeters, i.e. higher eccentricity of the ellipse, imply a wider fibre to matrix interface on which the stress transfer mechanism can be activated, thus producing a stiffer branch in the uncracked phase and higher loads in the post-cracked phase. For each increase of ψ value, the load and displacement capacity at the peak are both increased by approximately 30% in clevis set-up and 35% in camping set-up. Conversely, the displacement capacity corresponding to the formation of any new crack decreases with the increase of the perimeter, see zoomed diagrams of Figure 4.10. In fact, a larger contact surface allows for higher loads to be transferred at a given slip. Consequently, for each increase of ψ value, the end of the cracking process is registered at smaller slips and the crack-opening process
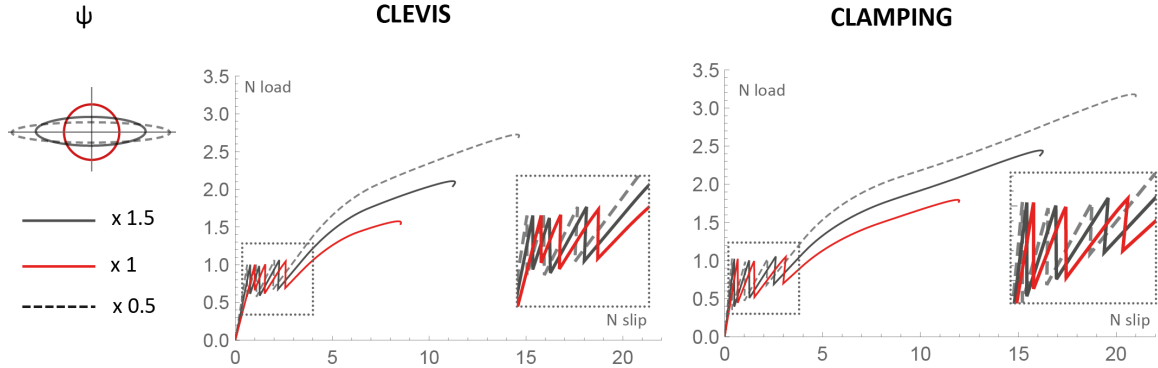
Figure 4.10: Parametric analysis of the proposed model to the variation of perimeter of the fibre, $\psi \cdot n$. Values of the normalised load (N load) plotted against the normalised slip (N slip).

is 8% and 15% shorter in clevis and clamping set-up respectively.

the variation of matrix tensile strength, f_{tm}, affects the cracking response of the specimen, determining both the load at which each crack forms, and the number of cracks developed. Matrix tensile strength increase, see Figure 4.11 delays the formation of the first crack providing proportionally longer linear elastic phases. Furthermore, the matrix tensile strength increase reduces the number of cracks and the displacement capacity at peak load for the clamped set-up. For decreasing matrix tensile strength, cracks form at slip values closer to each other. In particular, for the lowest value of f_{tm}=0.5 MPa, the crack opening process in the clevis set-up develops in the range 0.48-1.34 of the normalised slips, i.e. 10% of the slip at maximum load; for f_{tm}=1.5 MPa, slips are in the range 1.56-5.76 (49% of the slip at maximum load). In the clamping set-up, for the lowest values of f_{tm}=0.5 MPa, the crack opening process develops in the range 0.42-1.5 of the normalised slips range (9% of the slip at maximum load); for f_{tm}=1.5 MPa, slips are in the range 0.97-6.7 (47.8% of the slip at maximum load). For f_{tm}=2 MPa, no crack forms in the clevis grip set-up, and for the clamp-grip set-up, the load reached after the
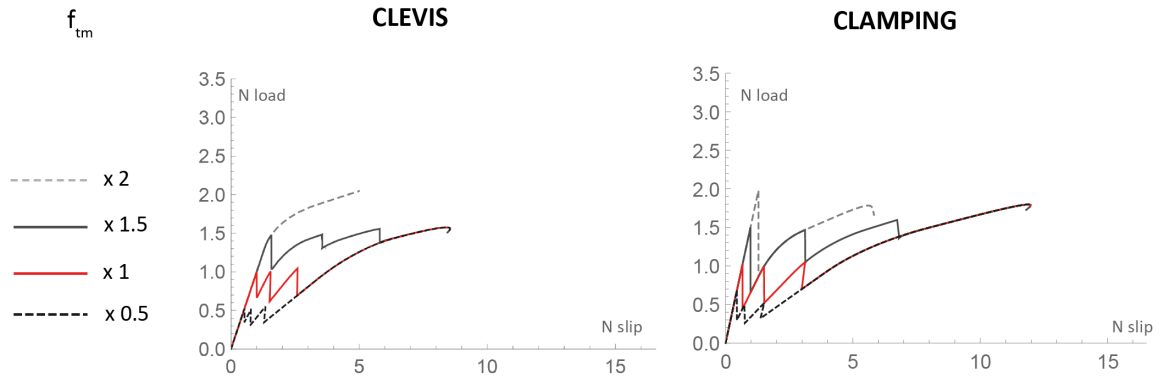
Figure 4.11: Parametric analysis of the proposed model to the variation of matrix tensile strength, f_{tm}. Values of the normalised load (N load) plotted against the normalised slip (N slip).

crack has formed is lower than the load reached at the end of the uncracked phase. For the considered parameter values, the shape of the load-slip diagrams changes noticeably.

4.3.2 Effect of CML properties

Concernig variation of the CML parameters, Equation 2.1, the variation of parameter δ_1 with constant τ_1 values, see Figure 4.12, only slightly affects the load-slip response: smaller δ_1 values produce a stiffer branch in the diagrams of the un-cracked phase, a shorter crack-opening phase and a slightly higher load capacity.

The variation of parameter δ_2, see Figure 4.13, shows that steeper softening branches of the CML cause shorter post-cracking branches and lower peak loads in the load-slip diagram. For the highest value of δ_1, a 13% and a 10% peak load increase, with respect to the middle value, occurs in clevis set-up and in clamping respectively. For both set-ups, a 20% load decrease, with respect to the middle values, occurs instead when the lowest value of δ_1 is considered.

In Figure 4.14, the shear stress defining the end of the linear elastic branch of
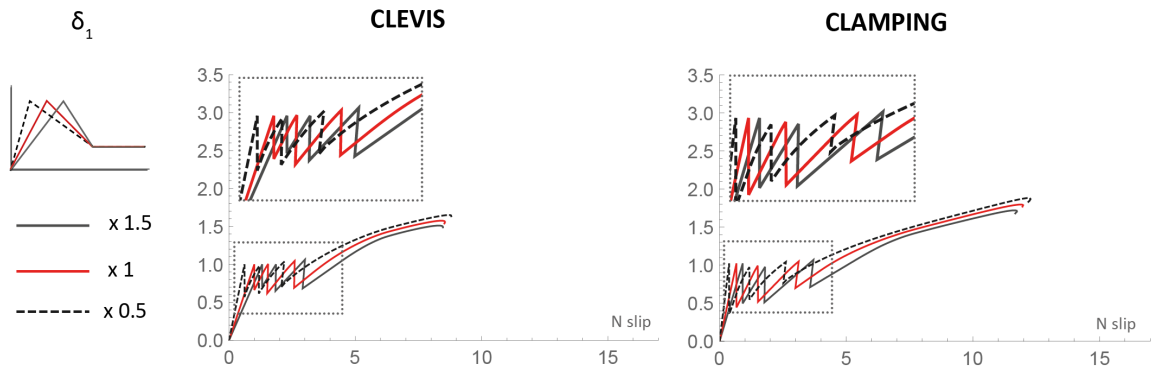
Figure 4.12: Parametric analysis of the proposed model to slip value defining the end of the linear ascending branch of the tri-linear CML, δ_1. Values of the normalised load (N load) plotted against the normalised slip (N slip).
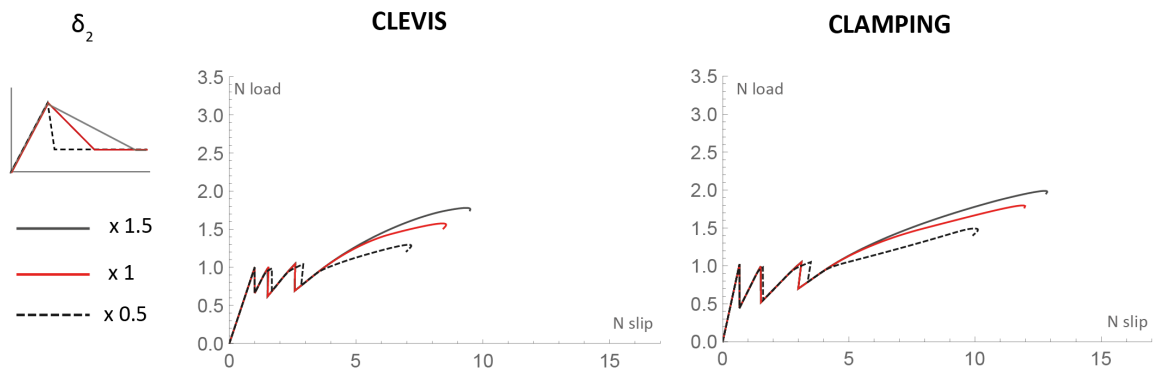
Figure 4.13: Parametric analysis of the proposed model to slip value defining the end of the softening branch of the tri-linear CML, δ_2. Values of the normalised load (N load) plotted against the normalised slip (N slip).
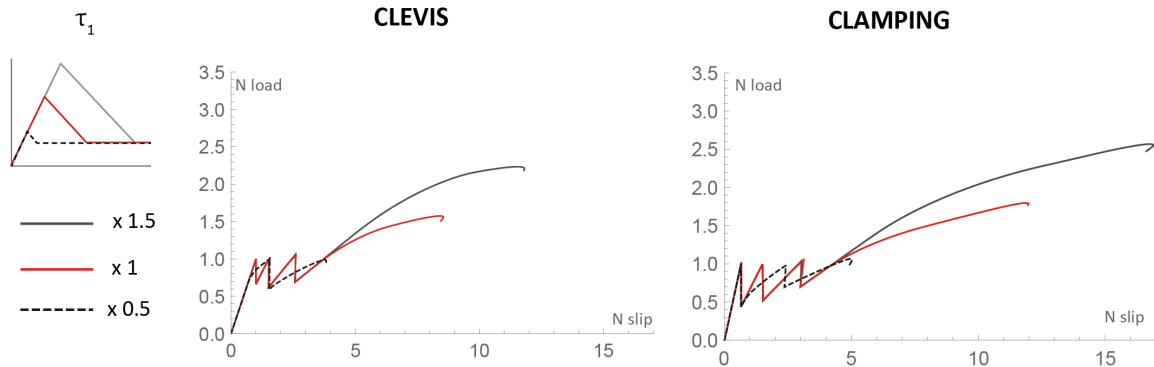
Figure 4.14: Parametric analysis of DTT to the variation of peak shear stress, τ_1 with fixed ascending stiffness (varying δ_1). Values of the normalised load (N load) plotted against the normalised slip (N slip).

the CML, τ_1, is varied without changing the slope of the linear elastic and softening branches of the CML, i.e. accordingly varying the associated slips δ_1 and δ_2. Higher τ_1 values lead to higher load and displacement capacity either in clevis and clamping: approximately, a 40% peak load and a 60% slip decrease are evaluated for the lowest value of the τ_1 compared to the middle value. For the increment of τ_1 from the base value to the highest, a 40% load and slip increase is determined. The lowest τ_1 value also determines the formation of only one crack in the clevis set-up and two cracks in the clamping one, due to the fact that the system early enters in the softening branch of CML.

The variation of τ_1 was also performed changing the values and consistently the slope of the linear elastic and softening branches of the CML, Figure 4.15. Remarkable differences are noticeable in the extent of the cracking phase. Compared to the middle τ_1 value, the smallest τ_1 value, black dashed diagrams, causes a 50% longer cracking phase in clamping and a 40% longer in clevis, gray continuous diagrams. The τ_1 variation also considerably affects the peak load, determining shifts between -32% and +22% for the lowest and highest values of τ_1, respectively,
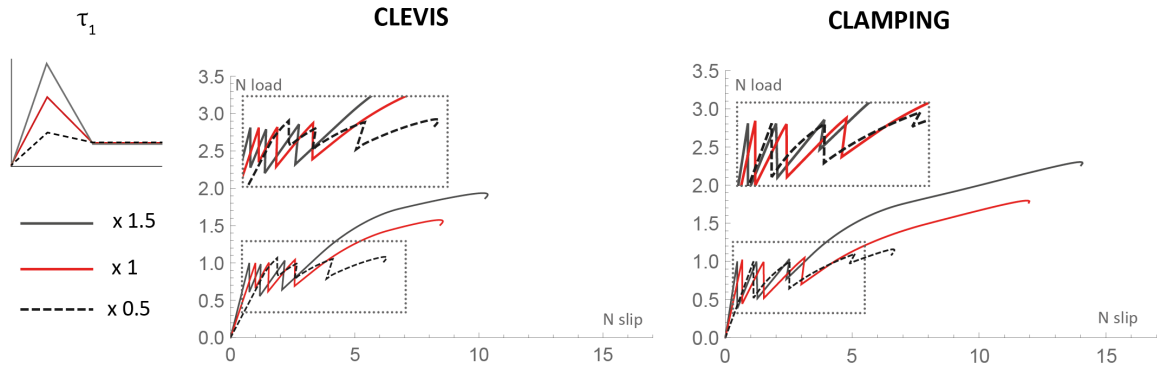
Figure 4.15: Parametric analysis of the DTT proposed model to the variation peak shear stress, τ_1 with changing stiffness (fixed δ_1). Values of the normalised load (N load) plotted against the normalised slip (N slip).

compared to the middle one in the clamping set-up, and between -45% and +25% in the clevis.

The τ_2 value is first varied along with δ_2, to avoid the change in the slope of softening branch of the CML, Figure 4.16. Such τ_2 variation yields slight effects on the peak load and displacement capacity, which both are increased or decreased by approximately 9% for each τ_2 shift. The variation of τ_2 is also performed by changing the value and the slope of the softening branch of the CML, Figure 4.17. Such a change leads to slightly more accentuated variations both in slip (-12% and +15%) and load (-11% and +12%) for the clevis set-up; similar variations are recorded for the clamped set-up.

4.3.3 Effect of crack position

The effect of cracks opening at different positions is investigated in the one-crack and two-crack conditions of the model, assuming a clevis grip configuration. Results are reported in Figures 4.18 and 4.19 where the load-displacement diagrams are normalised with respect to the values of load and slip attained at the end of
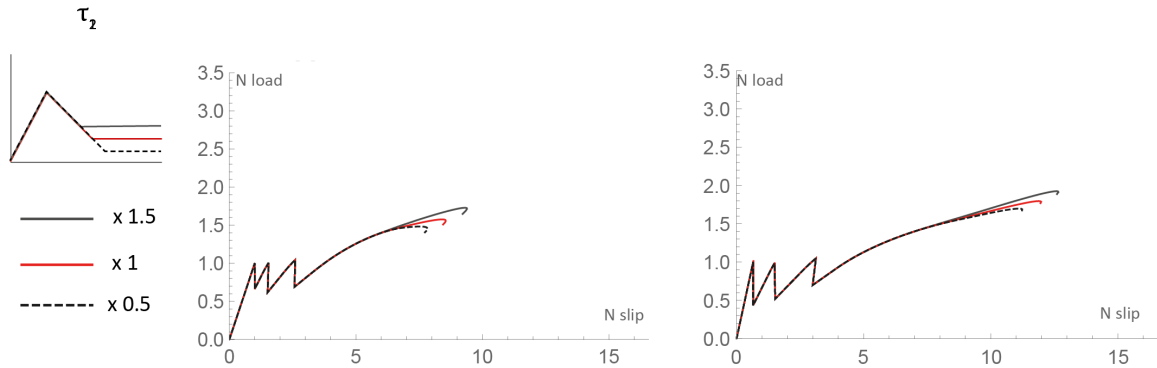
Figure 4.16: Parametric analysis of the DTT proposed model to the variation of the frictional shear stress, τ_2 with fixed softening stiffness (varying δ_2). Values of the normalised load (N load) plotted against the normalised slip (N slip).
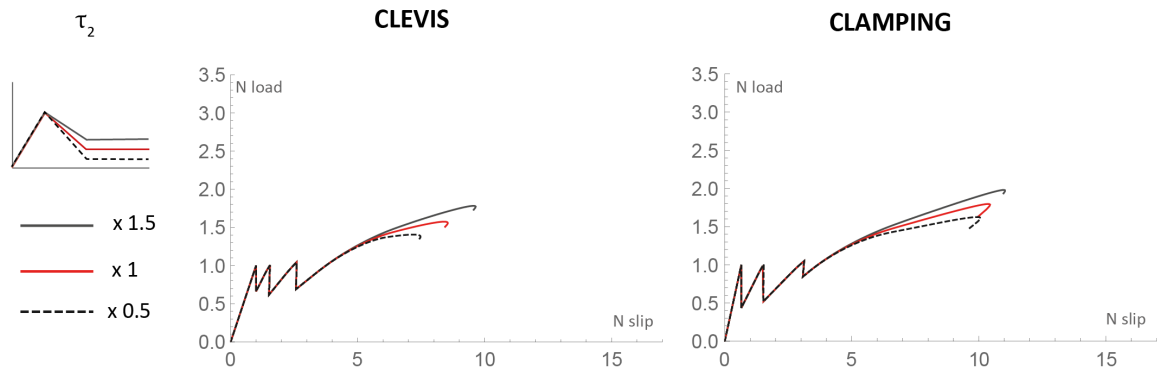
Figure 4.17: Paramrtic analysis of the DTT proposed model to the variation of the frictional shear stress, τ_2, with changing stiffness (fixed δ_2). Values of the normalised load (N load) plotted against the normalised slip (N slip).

Table 4.2: Parametric analysis for DTT: mechanical and geometrical parameters

Param.	var.	E_{lin} clevis	clamp	P_{max} clevis	clamp	$s_{P_{max}}$ clevis	clamp	L_c clevis	clamp
each	**x 1**	1	1.50	1.58	1.80	8.42	11.87	1.61	-
E	**x 0.5**	0.80	1.31	1.35	1.58	14.53	20.68	3.70	5.09
	x 1.5	1.34	1.70	1.73	1.93	6.32	8.67	1.13	1.83
ψn_y	**x 1.5**	1.37	2.07	2.10	2.43	11.30	16.25	1.50	2.12
	x 2	1.60	2.63	2.71	3.17	14.56	20.92	1.44	1.81
f_{tm}	**x 0.5**	-	-	1.057	-	-	-	0.86	1.08
	x 1.5	-	-	1.057	-	-	-	4.20	2.41
δ_1	**x 0.5**	1.61	2.76	1.65	1.88	8.73	12.24	1.36	2.23
	x 1.5	0.73	-	-	1.72	8.37	11.68	1.52	2.78
δ_2	**x 0.5**	-	-	1.29	1.48	7.11	10.09	1.91	2.86
	x 1.5	-	-	1.77	1.98	9.43	12.81	1.05	-
$\tau_1 (\text{and } \delta_1)$	**x 0.5**	-	-	-	1.06	3.74	4.99	-	1.74
	x 1.5	-	–	2.22	2.57	11.68	16.86	1.05	-
τ_1	**x 0.5**	1.35	0.90	1.087	1.15	6.18	6.59	2.25	1.42
	x 1.5	0.64	2.16	1.93	2.30	10.17	14.04	1.43	2.06
$\tau_2 (\text{and } \delta_2)$	**x 0.5**		-	1.48	1.69	7.69	11.21	1.05	-
	x 1.5	-	-	1.72	1.93	9.32	12.62	1.05	-
τ_2	**x 0.5**	-	-	1.40	1.62	7.33	10.98	1.56	-
	x 1.5	-	-	1.77	1.98	9.56	9.98	1.05	-

the uncracked phase, showing that for the same FRCM system remarkable differences are caused by different crack patterns. Normalised values of the stiffness of the pre-peak branch of the load-slip diagram E_c, maximum load value P_{max} and corresponding slip s_P and length of the cracking phase L_c are reported in Table 4.2.

Table 4.3: Paraemetric analysis for DTT: crack position

Crack pos.	E_c	P_{max}	s_P	L_c
C1=0.5L	2.65	2.14	19.6	-
C1=0.08L	2.89	1.61	0.57	-
C1=0.1L, C2=0.5L	2.91	0.81	2.65	-
C1=0.2L C2=0.5L	4.97	1.32	8.56	0.99
C1=0.2L, C2=0.7L	5.15	1.32	9.50	0.83
C1=0.4L, C2=0.5L	3.81	1.87	15.98	0.86

For the one-crack condition, two opposite settings are considered: a crack opening in the middle of the domain, i.e. at $x_{c1} = L/2$ (Figure 4.18a), or at the end of the left gripping area, i.e. $x_{c1} = L_g$ (Figure 4.18b). The system cracked at the middle shows a 62% and a 89% higher load and displacement capacity respectively, compared to the system cracked at 0.08L. Also, the stiffness of the load-slip diagram of the system cracked at 0.5L is 10% higher compared to the system cracked at 0.08L, being the shorter portion of Figure 4.18a, 6.25 times longer than that of Figure 4.18b.

For the two-crack condition, cracks generate three portions named A, B, and C, Figure 4.19a, b, c, d. In each combination of cracks, portion A is the shortest of the two extremity portions. Cracks are first set to open at c_1=0.1L and c_2=0.5L, Figures 4.19a, then their positions are varied as follows: first increasing portion A, reducing middle portion B and keeping fixed the longer extremity (C), by shifting c_1 to 0.2L, Figures 4.19a, b; then, keeping fixed extremity A with c_1=0.2L, and re-
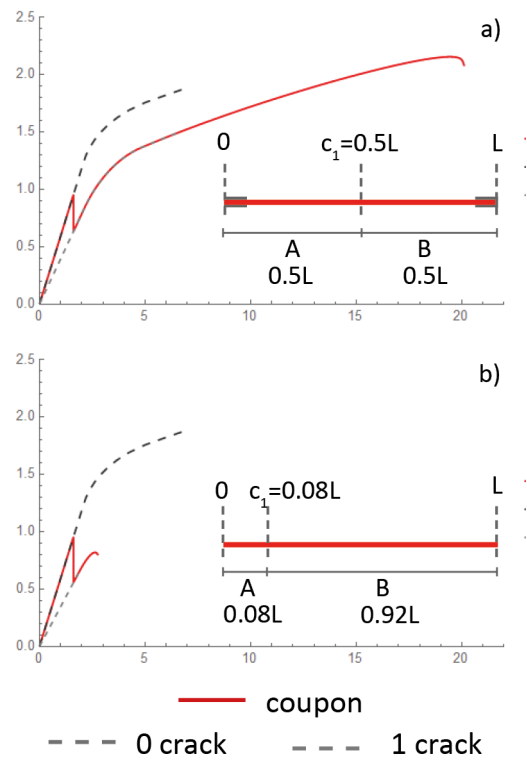
Figure 4.18: Effect of one crack opening at different locations assuming one crack at 0.5L (a), and 0.08L (b).

ducing extremity C, Figures 4.19b, c, hence, increasing middle portion B by setting c_2=0.7L; and finally moving cracks closer to the centre, i.e. c_1 =0.4L and c_2=0.5L, reducing middle portion B (Figures 4.19d).

In the load-slip diagram of the first scenario (first crack at the end of the gripping length), Figure 4.19a, after the formation of the first crack (first crack formed at 0.1L), the bond force transmitted from part A to the others is not high enough to induce the attainment of matrix tensile strength and the second crack cannot form at 0.5L. The slip and load capacity of the system is therefore limited.

In the second scenario, Figure 4.19b, portion A shows double the length of the previous configuration (Figure 4.19a). The stiffness of the one-crack independent diagram (Figure 4.19d) is 17% higher compared to the previous configuration, and both cracks develop. The displacement capacity at the peak load of the system is nearly four times higher.

For a decreasing length of the longest extremity portion C, Figure 4.19b, c, and a fixed length of portion A equal to 0.2L, the independent load-displacement diagram of the one-crack phase is the same, while the stiffness of the independent diagram of the two-crack phase (grey dashed curve) is 8% lower for c_2 forming at 0.7L (Figure 4.19c). As a result, the peak loads reached are equal, but a 10% slip capacity increase is recorded for a decreasing length of the longest extremity portion C, Figure 4.19c, passing from 8.4 to 9.5.

For cracks closer to the middle, case of Figure 4.19d, both the one-crack and two-crack independent diagrams (dashed curves) show higher stiffness compared to Figure 4.19c and the load slip diagram exhibits the highest load and slip capacity of the whole set.

From the analysis emerges that the length of the shortest extremity portion, i.e.
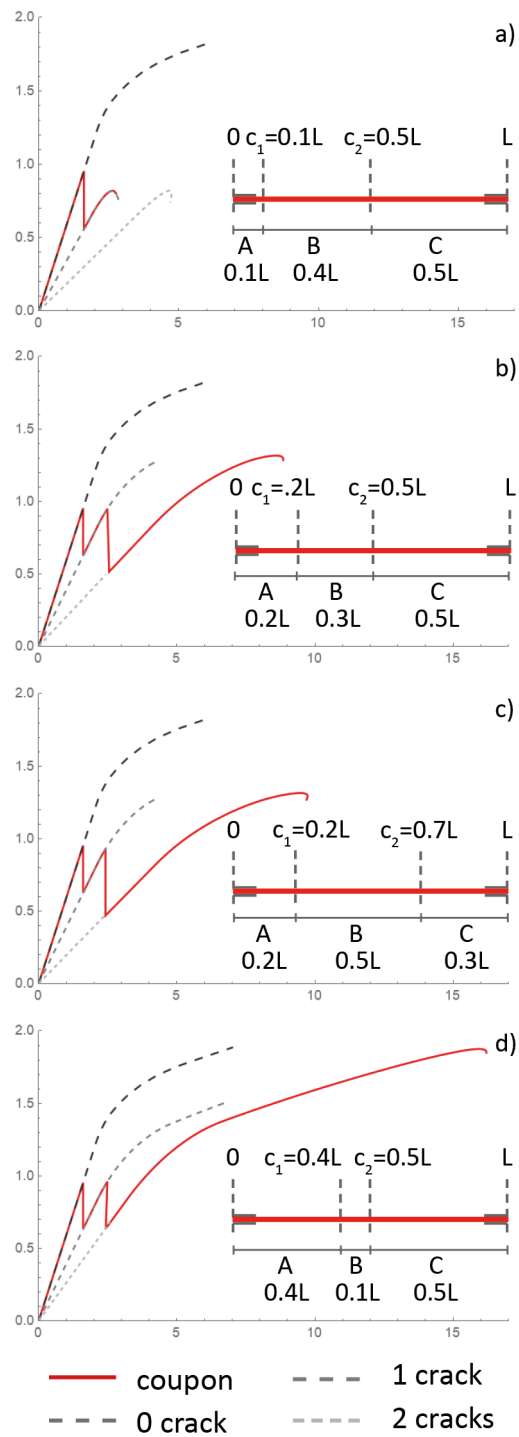
Figure 4.19: Effect of two cracks opening at different locations: 0.1L and 0.5L (a); 0.2L and 0.5L (b); 0.2L and 0.7L (c); and 0.4L and 0.5L (d)

A, is the driving parameter affecting the response quality and maximum load capacity. In particular, if the bond force transferred by the shortest extremity portion is lower than the maximum tensile force that the mortar can bear, any further crack cannot open. Also, increasing the length of portion A induces a stiffer branch of the load-slip diagram in the cracked phases and a higher load capacity, regardless of the length of the other segments. For a fixed-length segment A, capable of triggering a two-crack phase, and an increasing length of segment C, equal peak loads are reached, but for longer segment C, lower global displacement capacity at the peak is recorded. Also, stiffer branches in the cracking phases determine smaller load drop at crack formation. Therefore, for the same FRCM system, i.e., fixed CML, test set-up and specimen geometry, it is shown that the number of cracks and their position provide remarkable variations both quantitatively in terms of the recorded parameters and on the shape of the global response diagram.

CHAPTER 5

Discussion and model validation

5.1 DISCUSSION ON THE DTT SYSTEM

5.1.1 Effect of the relationship between mortar and CML characteristics

The parametric analysis carried out in Chapter 4 allowed the identification of the parameters, which mostly affect the response of FRCM system under tensile loading conditions. Among others, it was found that matrix tensile strength significantly influences the cracking behaviour of the specimen, determining both the load at which each crack forms, and the number of cracks developed; furthermore it was highlighted that the load and slip capacity of the system are affected by stress and slip values defining the CML.

Relying on such findings, an analysis of the combined variation of mortar tensile strength and CML characteristics was undertaken. Fifteen cases relevant to the quality of the load slip diagram were compared, assuming three values for τ_1, four values for τ_2, and three classes of mortar tensile strength, f_{tm}. The cases are displayed in Figure 5.1 and Figure 5.2, where each row corresponds to a CML defined by a τ_1 value (increased as in Figure 4.15b), while columns correspond to three classes of mortar tensile strength, f_{tm}; the value of τ_2 is set equal to 0.7 MPa in Figure 5.1, and to $\tau_1/3$ in Figure 5.2; the values of the maximum bond force per unit length per yarn are also indicated to ease identification and comparison with experimental results.

The combinations of parameters defining the selected cases provide different load slip diagrams (Figure 5.1 - 5.2), which are analysed according to the following featuring elements:
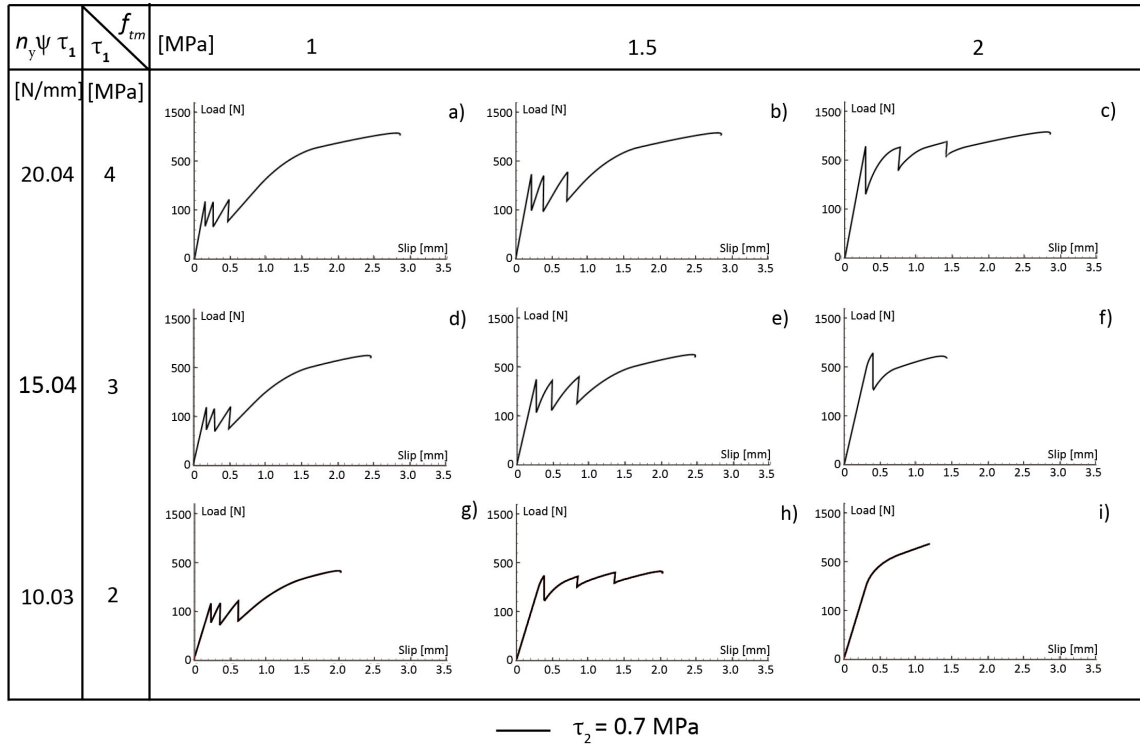
Figure 5.1: Load-slip diagrams for variations of the shear value defining the CML, τ_1, and matrix tensile strength, f_{tm}, assuming $\tau_2 = 0.7$MPa; a), b) and c) diagrams for τ_1=4MPa and f_{tm}=1MPa, 1.5 MPa and 2MPa, respectively; d), e) and f) diagrams for τ_1=3MPa and f_{tm}=1MPa, 1.5 MPa and 2MPa, respectively; g), h) and i) diagrams for τ_1=2MPa and f_{tm}=1MPa, 1.5 MPa and 2MPa, respectively. The DTT system has a total length L=500mm, crack positions at $x_{c1} = 100$ mm, $x_{c2} = 250$ mm, $x_{c3} = 400$ mm, and n_y=4.
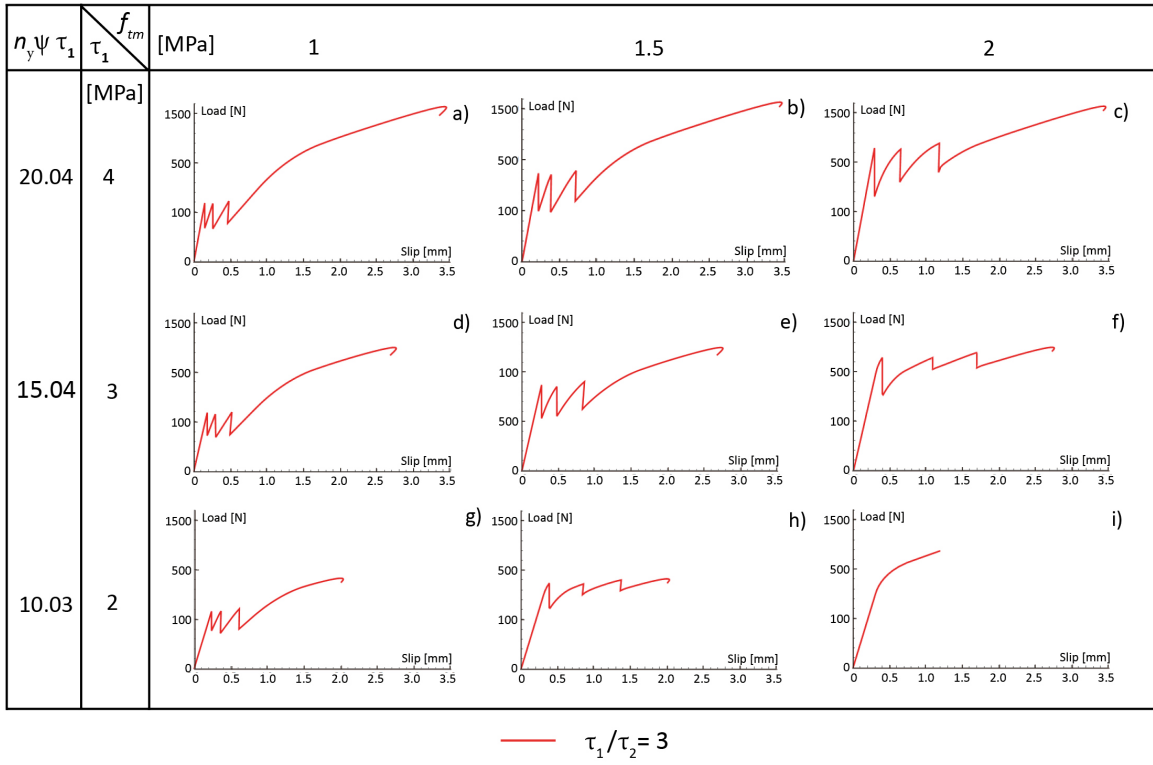
Figure 5.2: Load-slip diagrams for variations of the shear value defining the CML, τ_1, and matrix tensile strength, f_{tm}, assuming τ_1/τ_2=3; a), b) and c) diagrams for τ_1=4MPa and f_{tm}=1MPa, 1.5 MPa and 2MPa, respectively; d), e) and f) diagrams for τ_1=3MPa and f_{tm}=1MPa, 1.5 MPa and 2MPa, respectively; g), h) and i) diagrams for τ_1=2MPa and f_{tm}=1MPa, 1.5 MPa and 2MPa, respectively. The DTT system has total length L=500mm, crack positions at x_{c1} = 100 mm, x_{c2} = 250 mm, x_{c3} = 400 mm, and n_y=4.

- load and slip at the first crack

- length of the cracking phase

- post-cracking maximum load and related slip

For each given CML (rows of Figures 5.1 - 5.2), mortar tensile strength increase determines an increase of the first-crack load, a progressive stretching of the cracking phase, and does not affect the peak load. Hence, the fist-crack load and the peak load become closer for higher mortar strength values, affecting the overall shape of the diagram. These trends become more evident where the τ_2 value is kept constant (Figure 5.1).

For each tensile strength value (columns of Figures 5.1 - 5.2), the τ_1 increase determines an increase in the values of the post-cracking maximum load and related slip, with no effect on the first cracking load and slip, and a shrinkage of the cracking phase, markedly noticeable for the middle value of f_{tm}, see b, e, h in Figures 5.1 - 5.2. Also, for low values of τ_1 and high values of f_{tm}, (see f, h, i in Figures 5.1 - 5.2), non-linear pre-peak branches can develop. Limit cases of these trends are observed for one-crack conditions with peak load comparable to crack load (Figure 5.1f), or no crack due to high tensile strength and low τ_1 (Figure 5.1i and Figure 5.2i).

For the investigated systems, it is observed that the shapes of the load slip diagram are related to classes of τ_1/f_{tm} and τ_1/τ_2 ratios. Diagrams characterised by a high τ_1/f_{tm} ratio, show a shorter cracking phase and a load recovery branch, that can be idealised as a tri-linear diagram, see a, b and d in Figures 5.1 - 5.2. For decreasing values of the τ_1/f_{tm} ratio (Figures 5.1c, f, h and Figures 5.2f, h) a longer cracking phase is determined and a load recovery branch cannot be clearly

recognised; in this case, the global response can therefore be idealised as a bi-linear diagram. For fixed τ_1/τ_2 ratios (Figure 5.2), similar τ_1/f_{tm} ratios, found along the diagonals, produce self-similar diagrams with scaled values, as shown by Figures 5.2b, d in which τ_1/f_{tm}=2.6 and τ_1/f_{tm}=3 respectively; Figures 5.2c, e, g, in which τ_1/f_{tm}=2; and Figures 5.2f, h, in which τ_1/f_{tm}=1.5 and τ_1/f_{tm}=1.33 respectively.

5.1.2 Analysis of literature data

Trends highlighted in Section 5.1.1 suggest that in DTT, the relation between bond properties and matrix tensile strength deeply affects the load slip diagram so that either bi-linear or tri-linear diagrams can be obtained for the same value of the bond force. In the literature, good bonding at the fibre-to-matrix interface is related to a tri-linear load-slip diagram, while poor bonding to a bi-linear diagram (Truong and Kim 2021; Arboleda et al. 2016; D'Antino and Papanicolaou 2018). Observational evidence shows that both bi-linear and tri-linear behaviour can be found within the same test method, depending on the quality of bonding (D'Antino and Papanicolaou 2018) and FRCM tested typology (Arboleda et al. 2016; De Santis et al. 2018). A comparison with experimental data available in Caggegi et al. (2017) and Barhum and Mechtcherine (2012) is carried out to benchmark the results presented in Figures 5.1 - 5.2. In Caggegi et al. (2017), the same PBO-based system was tested by several research units, employing clevis and clamping set-ups. To allow comparison, the maximum bond stress of each system, τ_1, was back-calibrated from SST diagrams shown in Figure 10 of Caggegi et al. (2017) and is reported in Table 5.1, along with the main geometrical and mechanical characteristics. Since mortar tensile strength values were very close in all tests (see values reported in Figure 5.1), a comparison can be established with the right column of Figures 5.1 -

Fig. 11. Stress-strain curves of the PBO-FRCM specimens tested by clamping the extremities with hydraulic grips.
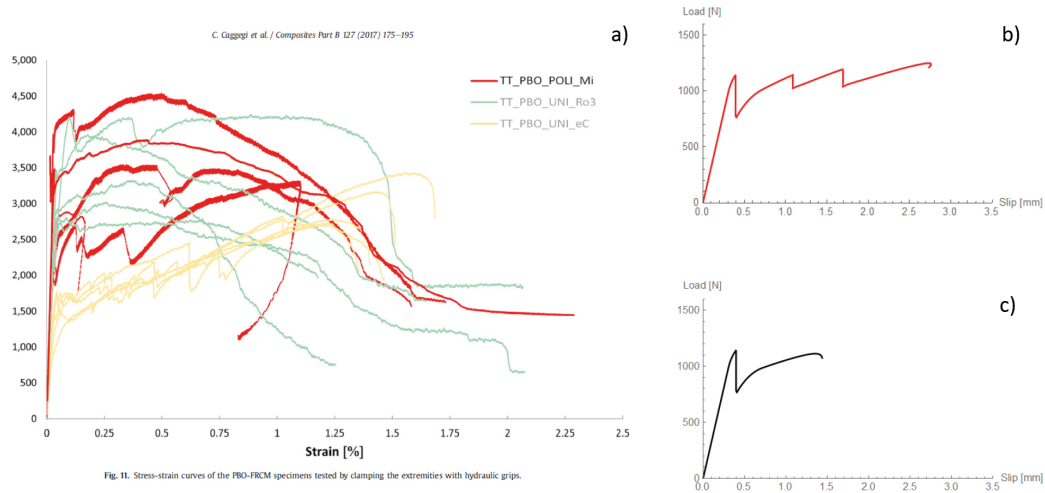
Figure 5.3: Comparison between (a) the load slip diagrams of PoliMi DST results reported in (Caggegi et al. 2017) and the load slip diagrams of (b) Figure 5.1f and (c) Figure 5.2f.

5.2. It must be noted that tests performed by CUT and UniRo3 are not considered, since failure in DST was induced by tensile rupture of the fibre.

Table 5.1: Parameters for the calibration of maximum shear stress value τ_1 of the round robin tests reported in Caggegi et al. (2017)

	t_f [mm]	b [mm]	n_y [-]	f_{tm} [mm]	δ_1 [mm]	τ_1 [MPa]	$\tau_1 \cdot \psi$ [N/mm]
PoliMi	0.014	45	3	2.58	0.75	3.25	2.38
UnieC	0.014	115	8	2.45	0.25	5.73	4.19
UniLy	0.014	45	3	2.8	0.6	2.59	1.89

The PoliMi DTT results, obtained with clamping set-up (Figure 11 in Caggegi et al. 2017), show one main crack followed by one or two more cracks and peak stress slightly higher than the cracking stress. This behaviour can be compared with Figures 5.1f - 5.2f, where the τ_1, as per calibrated from bond tests, falls into, see Figure 5.3.

The UnieC DTT results, obtained with clamping set-up (Figure 11 in Caggegi
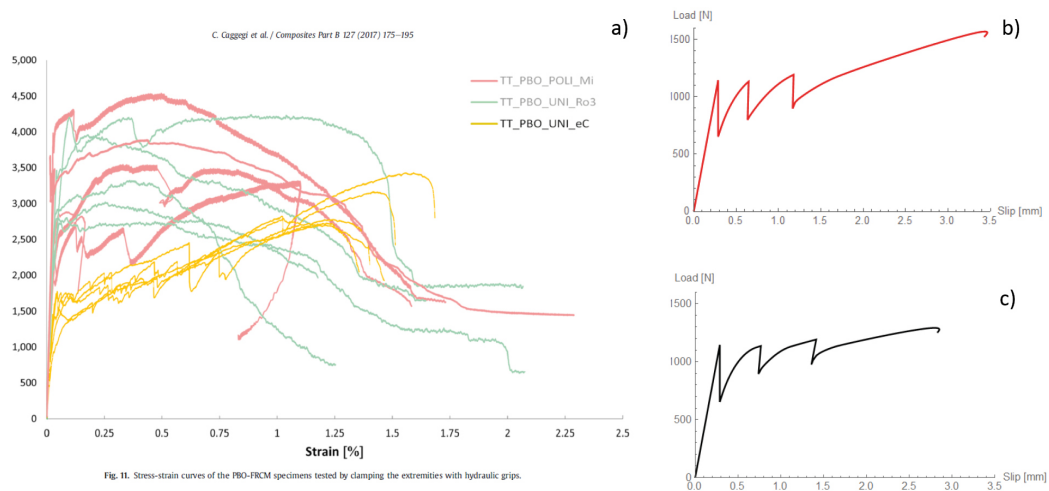
Figure 5.4: Comparison between (a) the load slip diagrams of UnieC DST results reported in (Caggegi et al. 2017) and the load slip diagrams of (b) Figure 5.2c and (c) Figure 5.1c.

et al. 2017), show a tighter series of cracks, a longer cracking phase and a higher number of cracks. The recorded peak stress is noticeably higher than the cracking stress. This behaviour can be compared to Figures 5.2c - 5.1c, where the closer τ_1 value in the table can be found, see Figure 5.4. The results of UniLy on DTT, obtained with the clevis grip set-up (Figure 12 in Caggegi et al. 2017), show a unique crack followed by a tension recovery up to post-cracking maximum stress equal or lower than the cracking stress, Figure 12 in Caggegi et al. (2017). According to the τ_1 value determined from bond tests, this FRCM system can be compared to the results showed in Figures 5.1f,i - 5.2i, see Figure 5.5.

Experimental results reported in Barhum and Mechtcherine (2012) show that increasing matrix tensile capacity, by adding short dispersed fibres to the same mortar, determines an increase in the load at which the first crack forms and the elongation of the crack development phase, (Figures 8 and 9 in Barhum and Mechtcherine 2012), while the load capacity of the system remains almost unchanged, hence, i.e. the bond capacity of the system can be considered unchanged.
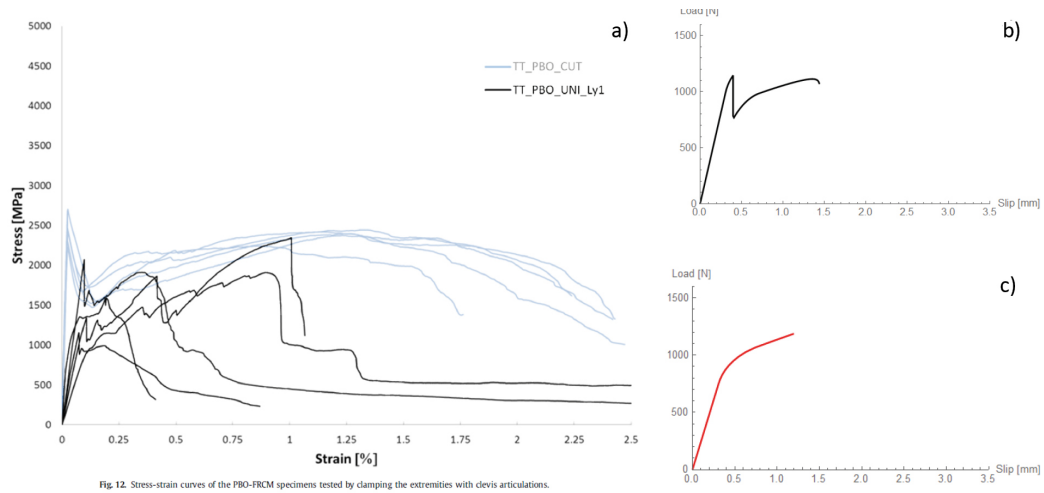
Fig. 12. Stress-strain curves of the PBO-FRCM specimens tested by clamping the extremities with clevis articulations.

Figure 5.5: Comparison between the load slip diagrams of (a) UniLy DST results reported in (Caggegi et al. 2017) and the load slip diagrams of (b) Figure 5.2i and (c) Figure 5.1f, i.

Diagrams similar to Figure 5.1f are found in Dalalbashi, Ghiassi, and Oliveira (2021b) and Soranakom and Mobasher (2010a). The same shape of the diagram is also found in Soranakom and Mobasher (2010a), but the load drop right before the initiation of the softening phase is attributed to the effect of junction points between the weft and warp direction of the reinforcing textile.

CHAPTER 6

Experimental campaign

An experimental campaign was carried out on a set of four commercially available FRCM systems to benchmark the ability of the proposed model to correctly predict the global behaviour of different FRCM systems. The experimental campaign was aimed at providing sets of data from FRCM systems with various geometrical and mechanical properties to feed into the model. Characterization of the tested composite materials for application purposes would have required a higher number of samples in most trials and is beyond the scope of this study.

The FRCM systems selected for the experimental campaign comprised a lime-based and two cement-based mortar matrices:

- a cement-based mortar matrix, named MXCAR in the following, constituted by portland cement clinker, flue dust, crystalline silica, and polymer additives, reinforced with short dispersed fibres (material not specified by the producer), and with an M20 resistance class (EN 998-2), according to the data-sheet;

- a cement-based mortar matrix, named MXPBO, also constituted by portland cement clinker, flue dust, crystalline silica, and polymer additives, reinforced with short dispersed fibres (material not specified by the producer), but with an M15 resistance class, according to the data-sheet;

- a lime-based matrix, named MXBAS, made of natural NHL and geo-binder, siliceous washed natural river sand, Dolomitic limestone and pure fine white Carrara marble, with an M15 resistance class, according to the data-sheet.

The main characteristics of matrices are reported in Table 6.1.

Table 6.1: Characteristics of the mortar matrices employed in the experimental campaign; the compressive strength class is as indicated in the producer datasheet. The constituting material of the short fibres is not provided in the datasheet

Name	binder	class	water per Kg $[l/Kg]$	short fibres
MXCAR	Portland cement	M20	0.26	x
MXPBO	Portland cement	M15	0.280	x
MXBAS	natural NHL	M15	0.212	-

Four balanced bi-directional open mesh textiles, constituted by three different reinforcing materials were coupled with the mortars:

- a carbon mesh textile, named CAR hereafter, with an equivalent thickness of $t_f = 0.023mm$, $42g/m^2$ of reinforcing fibres in the weft and warp directions, coupled with a tighter mesh of PE filaments, providing geometrical stability;

- a PBO textile, named PBO10 hereafter, with t_f=0.014 mm, 22 g/m^2 of reinforcing fibres in the weft and warp directions;

- a PBO textile, named PBO22 hereafter, with t_f=0.0064 mm, 10 g/m^2 of reinforcing fibres in the weft and warp directions, coupled with coated glass yarns and dry polypropylene yarns;

- a basalt textile, named BAS hereafter, with t_f=0.032 mm, 200 g/m^2 of reinforcing fibres in the weft and warp directions, coupled with AISI304 steel micro-rovings.

All textiles were fabricated with a woven technique, i.e. through the alternate overlapping of yarns in the weft and warp directions so that no mechanical anchorage was provided at the intersection points; only for the basalt textile, a light bonding apparently due to thermal forming between yarns belonging to weft and warp

directions was observed. The main characteristics of the selected textile are summarised in Table 6.2, where surface density, yarn spacing and equivalent thickness are reported.

Table 6.2: Characteristics of the bi-directional reinforcing textiles employed in the experimental campaign; the surface density provided by the reinforcing fibre is reported in brackets, when the information is made available by the producer.

Name	main material	surface density $[g/m^2]$	yarn spacing $[mm]$	eq. thickness $[mm]$
CAR	carbon	137 (84)	19	0.023
PBO 22	PBO	72 (44)	15	0.014
PBO 10	PBO	104 (20)	30	0.0064
BAS	basalt	200	17	0.032

6.1 MATERIAL TESTING

6.1.1 Three-point bending tests

The mechanical characterization of the mortar matrix consisted of three-point bending tests and compression tests.

Parallelepipedal specimens were fabricated for the three-point bending tests, by casting mortar in 160x40x40 mm specific steel formworks as follows. Each mortar was prepared according to directions provided in the producer data-sheet, adopting the water to cement ratio indicated in Table 6.1. A release agent was applied to the surfaces of the formworks and the formation of an oil film was awaited. Mortar was cast in the formworks, which were manually vibrated to enhance air expulsion. Specimens were cured for 28 days at ambient temperature and 50% relative humidity.

In the test set-up, each obtained specimen was placed above two supporting
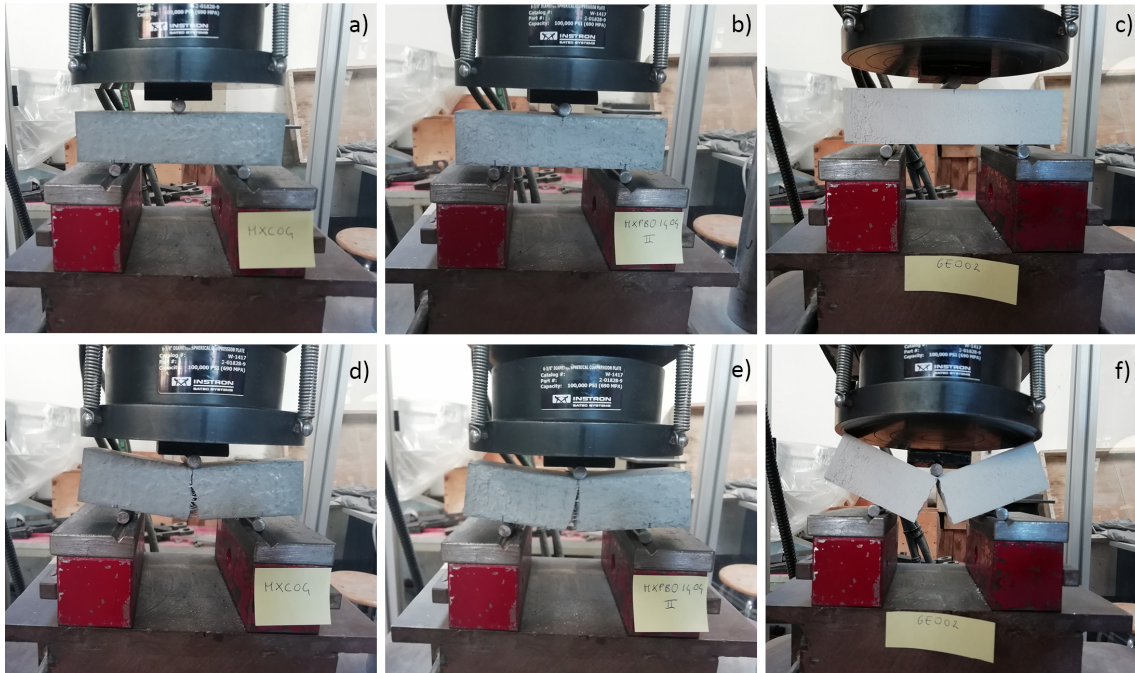
Figure 6.1: Three-point bending tests on the cement and lime based matrices: configuration of MXCAR (a), MXPBO (b) and MXBAS (c) before the beginning of the trial; configuration of MXCAR (d), MXPBO (e) and MXBAS (f) after failure.

steel cylinders with a 10 mm diameter, which were positioned at 30 mm from the right and left ends, thus leaving a 100 mm free length. A third cylinder was placed on the top surface of the specimens at middle section (80 mm from the right and left ends). The load was transferred to the upper cylinder through a steel plate in contact with the load cell; tests were carried out in a TC 5000N load cell at a 0.135 mm/min load rate. Results obtained are reported in 6.3, where the maximum attained load P_{max} and indirect tensile strength f_t for each specimen are listed.

It can be observed the MXCAR and MXPBO performed similarly providing P_{max} equal to 2039 N and 3022 N respectively, i.e. f_t equal to 6.65 N/mm^2 and 7.08 N/mm^2. MXBAS showed instead lower mechanical properties reaching a maximum load equal to $2497N$, i.e. a tensile strength equal to $5.85N/mm^2$. The short fibres dispersed in MXCAR and MXPBO bridged the crack after the failure of the

Table 6.3: Results of three-point bending and compression tests carried out on the cement-based MXCAR matrix.

Three-point bending			Compression		
specimen -	P_{max} [N]	f_t $[N/mm^2]$	specimen -	P_{max} [N]	f_c $[N/mm^2]$
MXCAR-01	2847.4	6.67	MXC-01a	27556	17.22
			MXCAR-01b	26596	16.62
MXCAR-02	2937.5	6.89	MXCAR-02a	29915	18.69
			MXCAR-02b	31373	19.61
MXC-03	2748.7	6.44	MXCAR-03a	28193	17.62
			MXCAR-03b	29315	18.32
MXCAR-04	2773.2	6.49	MXCAR-04a	24441	15.27
			MXCAR-04b	18386	11.49
MXCAR-05	2704.3	6.34	MXCAR-05a	24742	15.46
			MXCAR-05b	26975	16.86
MXCAR-06	3024.7	7.09	MXCAR-06a	29120	18.20
			MXCAR-06b	26469	16.54
Av.	2839.3	6.65	Av.	26923	16.83
St. Dev.	122.38	0.289	St. Dev.	3376.79	2.11
CV	4.34%	4.34	CV	12.5%	12.5%

specimen causing energy dissipation.

6.1.2 Compression tests

The two halves obtained from the failure of parallelepipedal specimens in three-point bending tests were tested in compression according to CEN (1999). Each specimen half was subjected to axial compression transferred through 40x40 mm steel plates. Tests were carried out with a 0.5 mm/min loading rate. Results obtained, reported in Tables 6.3-6.5, highlight a $16.83 N/mm^2$ compressive strength for the MXCAR, a $19.50 N/mm^2$ compressive strength for the MXPBO, and a $23.41 N/mm^2$ compressive strength for the MXBAS.
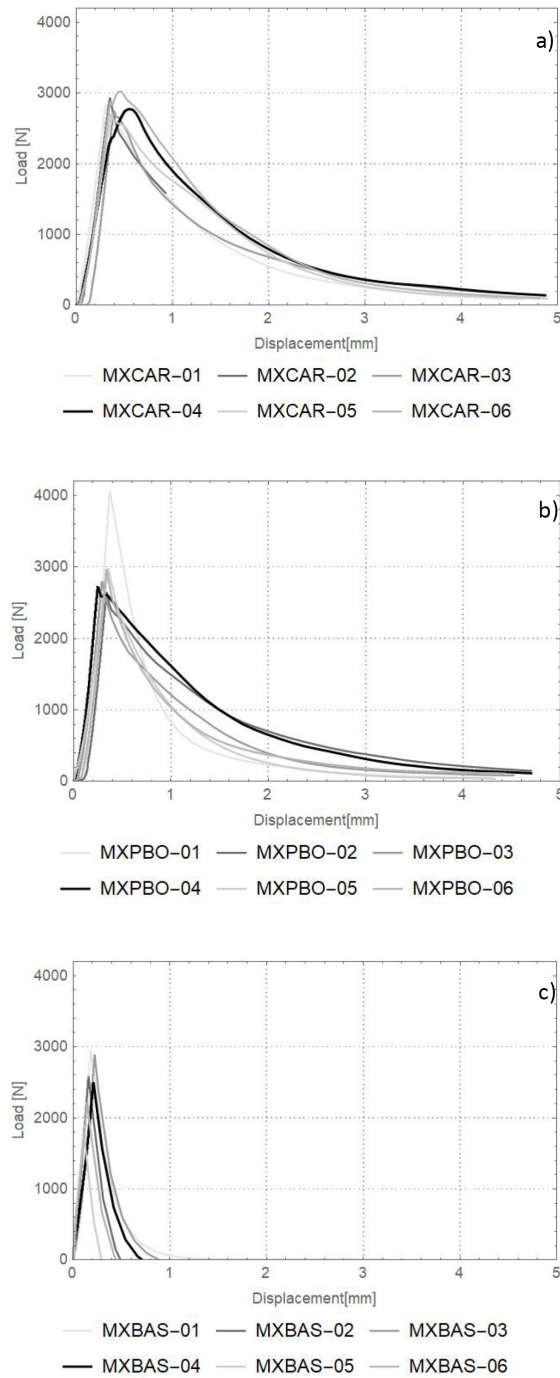
Figure 6.2: Results of three-point bending tests on the cement-based matrices MX-CAR (a), MXPBO (b), and the lime-based matrix, MXBAS (c).

Table 6.4: Results of three-point bending and compression tests carried out on the cement-based MXPBO matrix.

Three point bending			Compression		
specimen	P_{max}	f_t	specimen	P_{max}	f_c
-	[N]	$[N/mm^2]$	-	[N]	$[N/mm^2]$
MXPBO-01	4045.5	9.48	MXPBO-01a	16024	10.02
			MXPBO-01b	27561	17.23
MXPBO-02	2638.2	6.18	MXPBO-02a	33762	21.10
			MXPBO-02b	39568	24.73
MXPBO-03	2805.2	6.57	MXPBO-03a	16024	10.01
			MXPBO-03b	40387	25.24
MXPBO-04	2714.5	6.36	MXPBO-04a	37980	23.74
			MXPBO-04b	39331	24.58
MXPBO-05	2980.9	6.99	MXPBO-05a	35453	22.16
			MXPBO-05b	30139	18.84
MXPBO-06	2948.7	6.91	MXPBO-06a	30668	19.17
			MXPBO-06b	27525	17.20
Av.	3022.17	7.08	Av.	31201	19.50
St. Dev.	518.35	1.21	St. Dev.	8420	5.26
CV	17.15%	17.15%	CV	26.98%	26.98%

Table 6.5: Results of three-point bending and compression tests carried out on the lime-based MXBAS matrix.

Three point bending			Compression		
specimen	P_{max}	f_t	specimen	P_{max}	f_c
-	[N]	$[N/mm^2]$	-	[N]	$[N/mm^2]$
MXBAS-01	2968.8	6.95	MXBAS-01a	37396	23.37
			MXBAS-01b	37989	23.74
MXBAS-02	2586.4	6.06	MXBAS-02a	35679	22.30
			MXBAS-02b	38734	24.21
MXBAS-03	2893.1	6.78	MXBAS-03a	36801	23.00
			MXBAS-03b	40517	25.32
MXBAS-04	2504.1	5.87	MXBAS-04a	36387	22.74
			MXBAS-04b	38768	24.23
MXBAS-05	1804.8	4.23	MXBAS-05a	36571	22.86
			MXBAS-05b	38762	24.23
MXBAS-06	2226.3	5.21	MXBAS-06a	37977	23.73
			MXBAS-06b	33974	21.23
Av.	2497.25	5.85	Av.	37462	23.41
St. Dev.	433.57	1.015	St. Dev.	1722.2	1.076
CV	17.36%	17.36%	CV	4.5%	4.5%
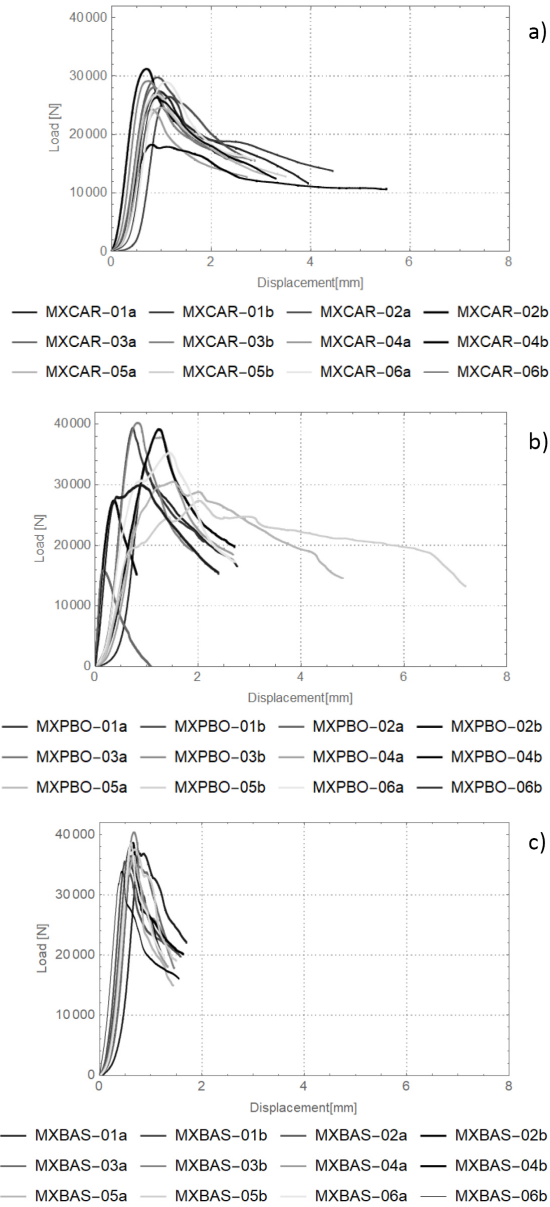
Figure 6.3: Resukts of compression tests on the cement-based matrices MXC (a), and MXPBO, (b), and the lime-based matrix, MXBAS (c).
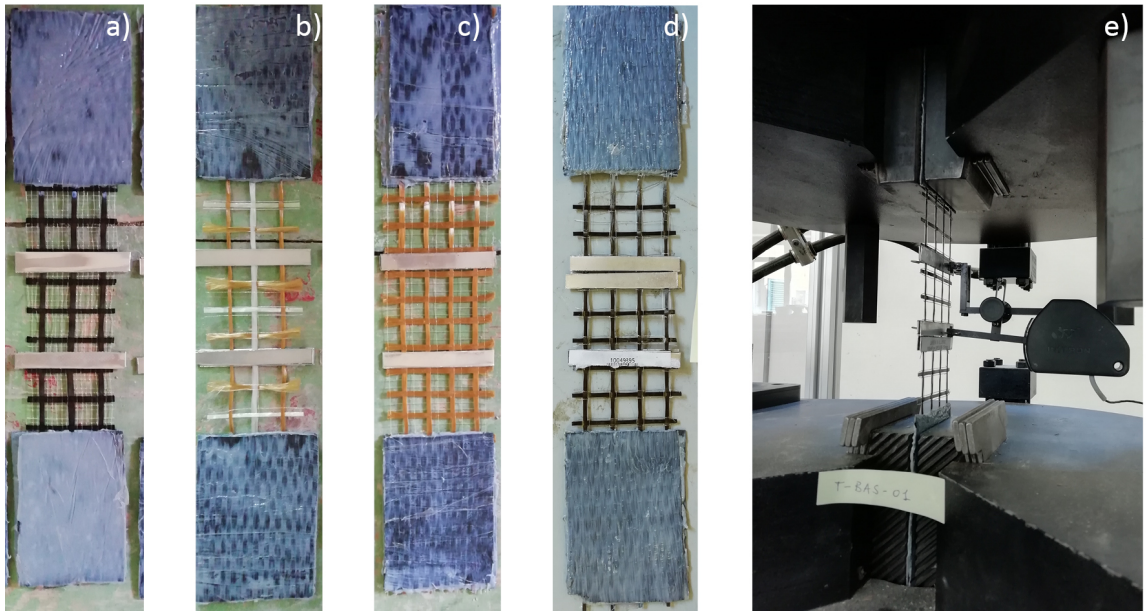
Figure 6.4: Specimens for direct tensile tests on the CAR (a), PBO10 (b), PBO22 (c), and BAS (d) textile; test set-up and instrumentation employed (d).

6.1.3 Fibre Direct tensile test

Fibre tensile tests were carried out for the mechanical characterization of the textile reinforcement. Specimens were fabricated by cutting 60x300 mm rectangular portions of the textiles. Each specimen comprised a specific number of yarns, according to yarn spacing reported in Table 6.2: three yarns of the CAR and of the BAS textile, four yarns of the PBO22 textile and two yarns of the PBO10 textile. After 70x100 mm FRP tabs were applied to the extremities to provide gripping, specimens were inserted in a TC 5000N load cell and tested in displacement control with a 0.5mm/min load rate.

All specimens showed a linear elastic behaviour until tensile failure of the fibre, see Figure 6.5. Results, reported in Table 6.6, and shown in Figure6.5, allowed the evaluation of the average elastic modulus, E, and tensile strength f_t of all reinforcing textiles: f_t=1185 N/mm^2 and a E=78061 N/mm^2 were found for the
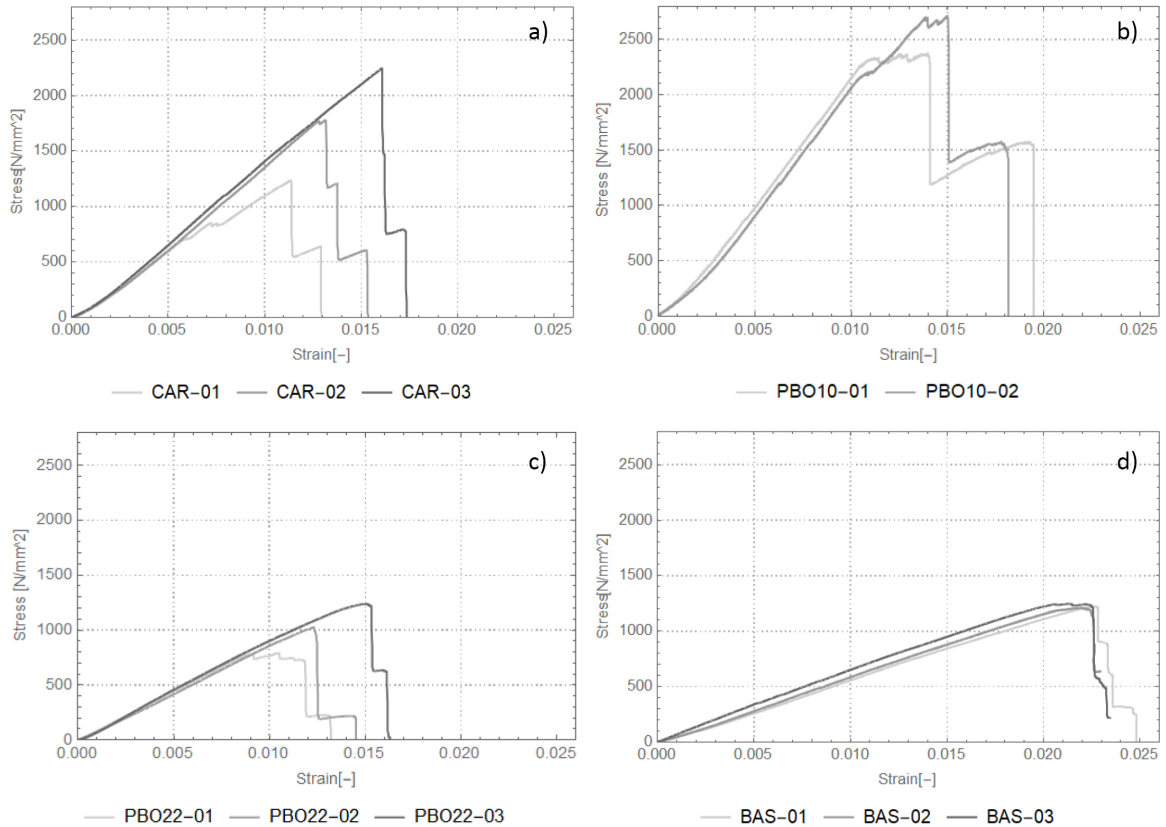
Figure 6.5: Stress-strain diagrams obtained from results of the direct tensile tests on the CAR (a), PBO10 (b), PBO22 (c), and BAS (d) textile.

basalt textile; f_t=1756 N/mm^2 and E=193740 N/mm^2 were found for the carbon textile; $f_t = 1020 N/mm^2$ and E=119487 N/mm^2 were found for the PBO22 textile; a f_t=2385 N/mm^2 and E=300250 N/mm^2 were found for the PBO10 textile.

6.1.4   Direct Shear Tests

Direct Shear Tests were performed on 220x95x8 mm composite jackets adhered to a brick substrate. Two 95x220 mm timber moulds were fabricated for each DST specimen, with 4x4 mm square section slats. Bricks were cleaned with a dry medium bristle brush and saturated with water. A wooden mould was fixed to the upper surface keeping its sides parallel to the brick edges. A 95x350 mm portion of each
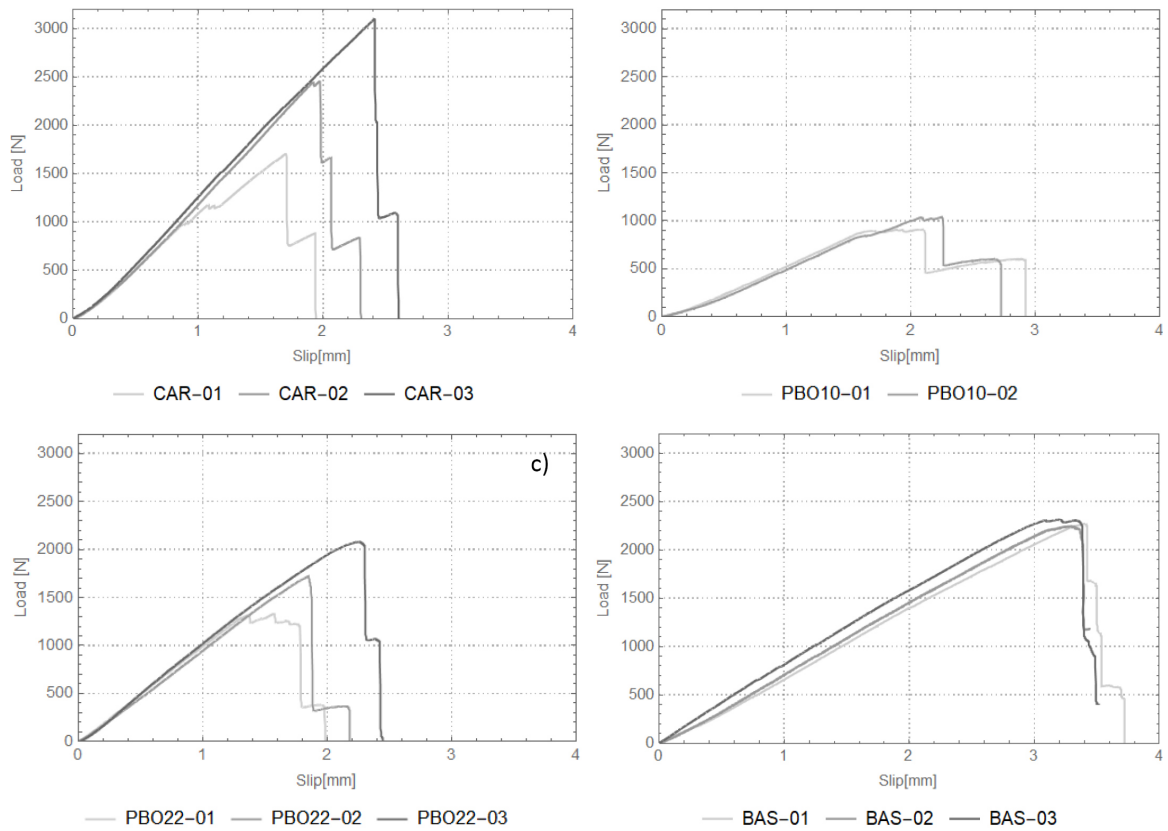
Figure 6.6: Load-slip diagrams obtained from results of the direct tensile tests on the CAR (a), PBO10 (b), PBO22 (c), and BAS (d) textile.

Table 6.6: Results of tensile tests on the reinforcing textiles.

specimen	ε_u	f_t	E_y
	[-]	$[N/mm^2]$	$[N/mm^2]$
CAR-01	0.014	1239	136348
CAR-02	0.015	1783	148639
CAR-03	0.018	2245	150927
Average	0.016	1756	145302
St. Dev.	0.0013	503.74	7840.59
CV	11%	29%	5.4%
PBO10-01	-	-	-
PBO10-02	0.015	2373	226404
PBO10-03	0.014	2712	299306
Average	0.015	2542	262855
St. Dev.	-	-	-
CV	-	-	-
PBO22-01	0.009	1592	89845
PBO22-02	0.012	2051	88159
PBO22-03	0.015	2477	90842
Average	0.012	2041	89615
St. Dev.	0.003	221.50	1355
CV	25%	22%	1.5%
BAS-01	0.022	1223	59419
BAS-02	0.022	1210	61478
BAS-03	0.023	1246	60797
Av.	0.022	1226	60564
St. Dev.	0.0001	18.26	1048.79
CV	1.1%	1.5%	1.7%

reinforcing textile was cut. The matrix paste was cast in the mould and levelled with a spatula, so that an even thickness of 4 mm was ensured; then the reinforcing textile was applied to the surface, taking care of its alignment, and slightly pressed. The second mould was positioned over the first and fixed to it. Another layer of cement paste was cast and levelled, reaching a total thickness of 8mm, Figure 6.7. Specimens were cured for 28 days at 20°C and 50% relative humidity. After curing, the extremity of the free length of the textile was wrapped around a steel cylinder and then fixed through an epoxy resin, which was also applied to the non-embedded length.

Each specimen, labelled according to the name of the embedded textile followed by an identification number, was placed in a steel frame fixed to the testing machine, as suggested in Carloni et al. (2015), obtaining a pull-push configuration; the steel cylinder was inserted in a U-shaped steel device connected to the testing machine through hinges and shackles, which prevented the misalignment of the fibre during load application. Two cantilever displacement transducers were positioned at the end of the jacket, and a third one on the side of the brick. Tests were carried out at 0.2 mm/min displacement rate using a 50-kN load cell (type TCLP5B, Tokyo Sokki Kenkyujo Co. Ltd).

Results of specimens CAR 02 and CAR 03, Figure 6.9a, of the carbon-based system showed a linear behaviour followed by decreasing stiffness, reached peak loads of 2491 N and 2912 N respectively, and failed due to tensile rupture of the textile out of the matrix. Specimen CAR01, Figure 6.9a, described an anomalous load slip diagram, due to rotation of the brick substrate, which led to misalignment of the embedded and non-embedded textile: after a delayed stiffness activation followed by a linear elastic phase up to 1857 N load value, the specimen experienced
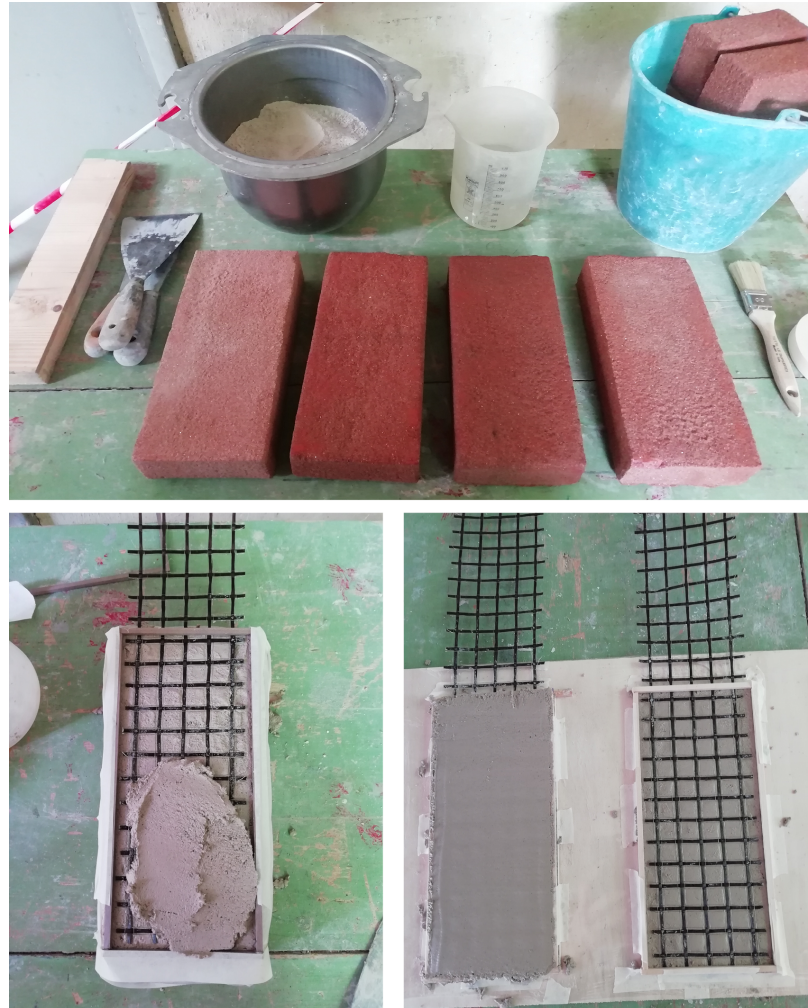
Figure 6.7: Fabrication process of SST specimens.
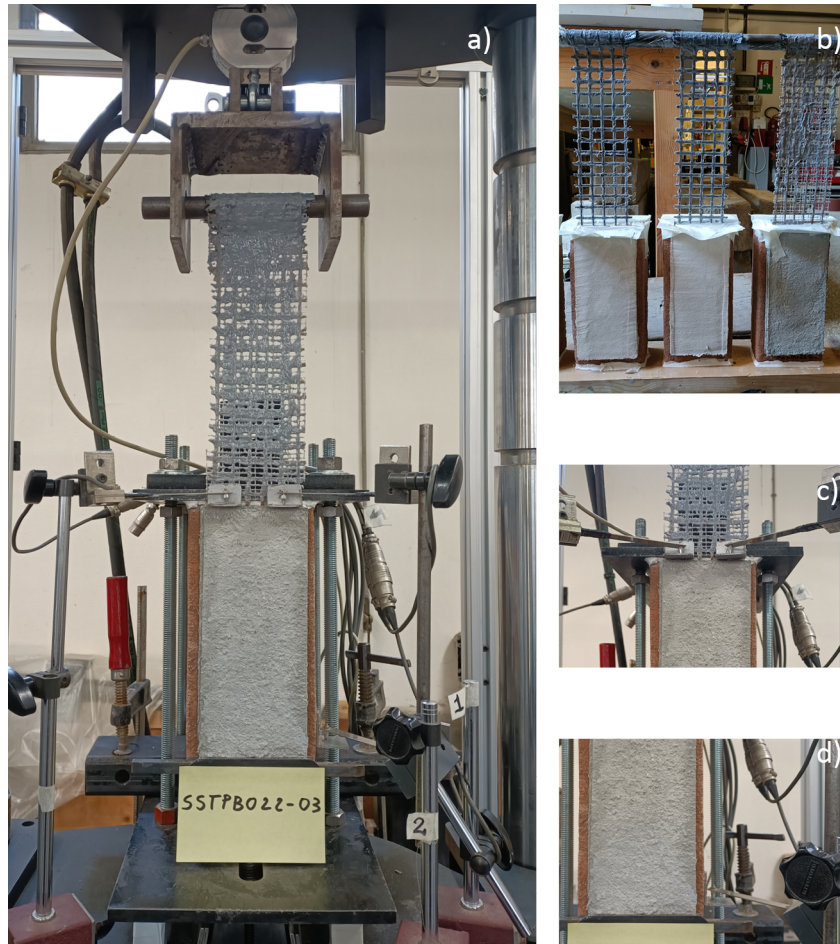
Figure 6.8: SST testing set-up (a); impregnation of the un-embedded textile with epoxy resin (b); cantilever displacement transducers at the edge of the embedded length (c); cantilever displacement transducer positioned on the side of the support (d).

Figure 6.9: Load-slip diagrams obtained through direct shear tests on the FRCM system reinforced with: CAR (a), PBO10 (b), PBO22 (c), and BAS (d) textiles.

a strain hardening behaviour and failed due to rupture of the fibre at 2540 N.

The PBO10-01 and PBO10-02, Figure 6.9b, specimens provided a linear ascending branch followed by a non-linear branch reaching up to an average peak load of 1262 N and followed by a short descending branch. Specimens PBO10-03, Figure 6.9b, after reaching the load value of 936 N, showed a short descending branch and a load recovery which led to a peak load value of 1055 N, i.e. the frictional plateau. All specimens of the PBO10 system failed due to textile slippage.

The PBO22-01 specimen, Figure 6.9c, provided a linear behaviour followed by a non-linear ascending branch, which reached 2549 N, before failing due to tensile

rupture of the textile out of the matrix. Specimens PBO10-02, Figure 6.9c, shared the same load path as PBO22-01, but failed prematurely due to rupture of the non-embedded textile wrapped around the steel cylinder at 1611 N; the same failure mode was also observed in specimen PBO22-03, which also showed an initial delayed stiffness activation probably caused by different tightening levels of the embedded yarns, Figure 6.9c.

The basalt-based textile, Figure 6.9d, showed an almost linear elastic behaviour until failure, which was recorded prematurely at 2667 N load and 1.32 mm slip for BAS 01 and at 1571 N and 0.57 load for BAS 02.

6.1.5 Direct Tensile Tests with clamped set-up

Direct tensile tests were performed on 500x60x8 mm composite laminas, that were fabricated according to the following procedure: two 500x60 mm moulds were assembled for each DTT specimen with 4x4 mm timber slats and one of them was secured to a flat surface. The matrix paste was cast in the mould reaching 4 mm thickness; the reinforcing textile was cut in stripes of the same dimension of the mould and positioned on the mortar, taking care of fibre alignment and slightly pressed. The second timber mould was positioned over the previous one and the second layer of mortar was cast reaching 8 mm total thickness. Specimens were cured for 28 days at 20°C and 50% relative humidity and tests were performed according to a bolted clamping set-up: after glueing aluminium plates to the gripped areas, the coupon specimen was inserted into steel plates coated with a neoprene layer to enhance adhesion and prevent mortar failure within the gripping, leaving a 260 mm free length. The steel plates were secured by fastening six bolts with a dynamometer key, assessing 11 Nm, which corresponded to 4.7 MPa of transverse
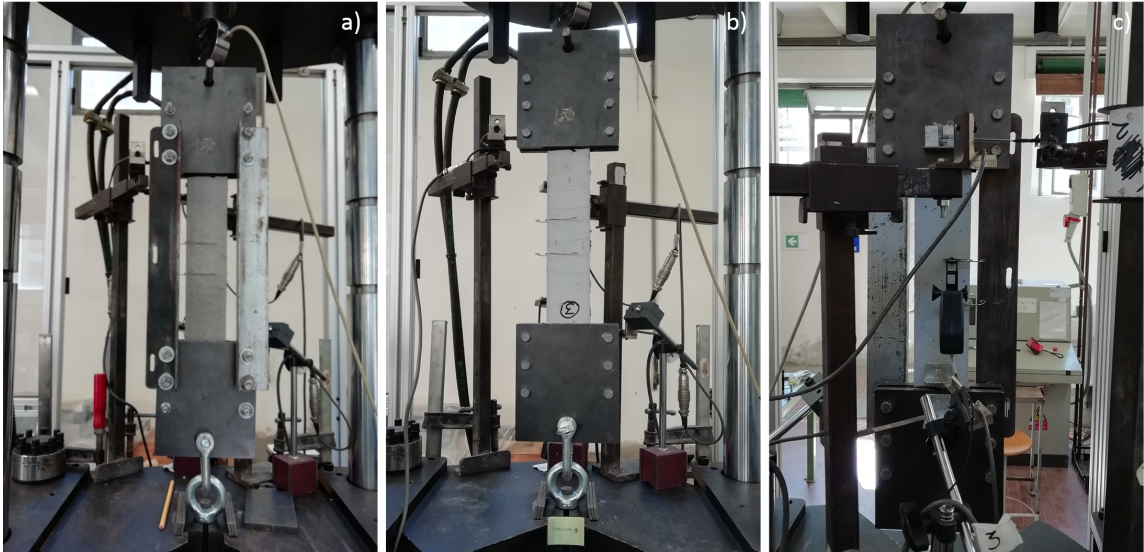
Figure 6.10: Set-up for DTT: specimens placed in the testing machine with steel frame (a); front view of the specimen with the 50 mm extensometer at middle section (b); rear view of the specimen where the linear variable transducers placed on the steel plates of the gripping are visible (c).

compression on the gripped areas. Two cantilever displacement transducers were positioned on the steel plates, and two on the specimen jacket, measuring 310 mm and 240 mm gauge length. A 50 mm gauge length extensometer was also placed in the middle section of the specimen. The slip values plotted in load-slip diagrams correspond to the relative displacement of the cantilever displacement transducers placed on the jacket close to the gripping apparatus and therefore comprise textile-matrix slips and strains of the composite constituent materials.

A 50-KN (type TCLP5B, Tokyo Sokki Kenkyujo Co. Ltd) load cell was placed above the upper jaw to register the global displacement, in addition to the load cell embedded in the actuator. Tests were carried out in displacement control at a 0.2mm/min load rate.

Results of the carbon-based FRCM system reached an average peak load of 2206 N, before the onset of the cracking process, which involved the formation of
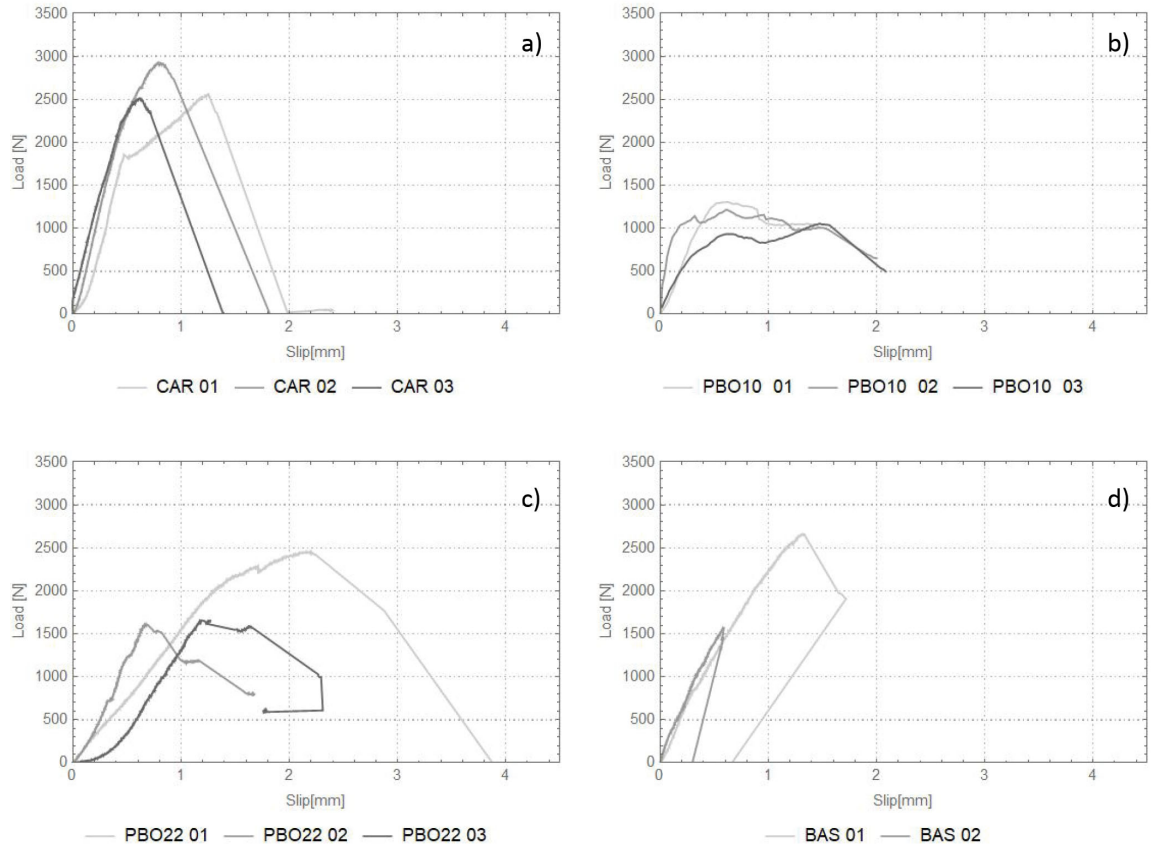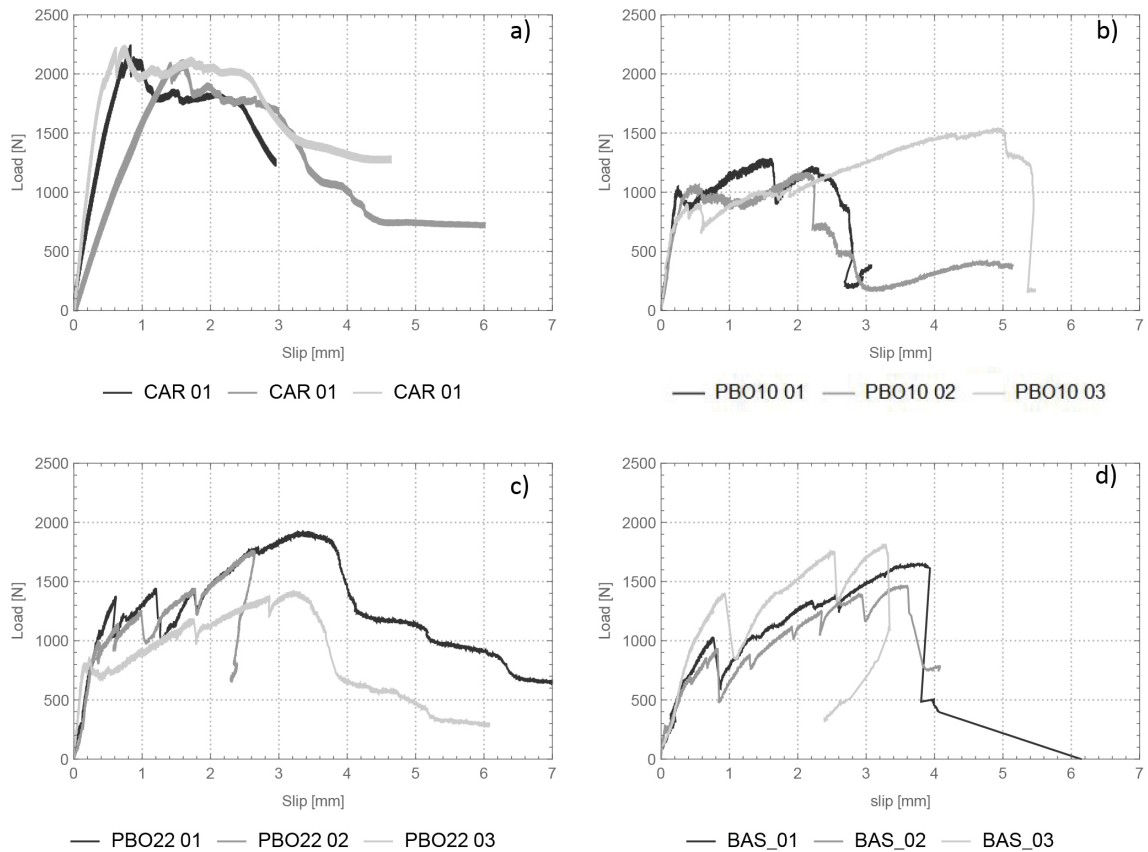
Figure 6.11: Load-slip diagram obtained through direct tensile tests on the FRCM system reinforced with CAR (a), PBO10 (b), PBO22 (c) and BAS (d) textiles.

one crack for CAR-02 and two cracks for CAR-01 and CAR-03. Specimens failed due to textile slippage of the fibre within the matrix and described a frictional ending plateau around 1900 N load value, Figure 6.11a.

The specimens of the PBO10 system, Figure 6.11b, behaved linearly in the uncracked phase, which ended at an average load value of 913 N; the cracking process, which envisaged the formation of one main crack close to the gripping area, and other minor cracks, was followed by a load recovery phase which leads to 1288 N, 1168 N and 1541 N peak loads for PBO-01, PBO-02 and PBO-03 respectively.

Specimens of the PBO22 FRCM system showed a first linear elastic branch up

to an average load value of 949 N, see Figure 6.11c. After crack formation a load recovery phase with reduced stiffness was observed up to reaching an average peak load of 1704 N. Specimens failed prematurely PBO-03 underwent premature rupture of the fibre.

For the basalt-based system, Figure 6.11d, after a short linear branch ending between 0.04 and 0.06 mm slip, all specimens showed reduced stiffness and exhibited a non-linear behaviour before the formation of the first crack. An average peak load of 1647 N was recorded and all specimens failed for tensile rupture of the fibre.

6.2 BACK-CALIBRATION OF THE COHESIVE MATERIAL LAW

The Cohesive Material Laws characterising the investigated FRCM systems were back-calibrated from experimental results provided by direct shear tests. The calibration was performed on the experimental results of the presented campaign for the carbon-based and both PBO-based FRCM systems; for the basalt-based system, data from Misseri et al. (2019) were employed as well, to overcome difficulties caused by the premature failure of the SST specimens highlighted in Section 6.1.5. The back calibration was performed according to the procedure presented by Focacci et al. (2017) and previously recalled in Chapter 2.

For modelling purposes, a tri-linear shape of the CML, with an initial branch starting from zero slip at zero stress and an ending frictional branch described by Equation 2.1, was assumed. The selected shape of the CML was defined by the following parameters: τ_1 and s_1, shear stress and slip values at the end of the linear elastic branch; τ_2 and s_2 shear stress and slip values at the end of the softening branch. The back calibration was performed through the interpretation of

Table 6.7: Parameters employed for the estimation of DTT mechanical response through the proposed model.

		CAR	PBO10	PBO22	Basalt
$\psi \cdot n$	[mm]	7.03	3.7	5.03	7.84
f_{tm}	[MPa]	3.5	1.9	1.9	1.5
τ_1	[MPa]	3.88	2.51	1.49	2.14
τ_2	[MPa]	2.56	1.18	0.89	0.66
δ_1	[mm]	0.33	0.17	0.060	0.29
δ_2	[mm]	0.44	0.32	0.807	0.61

the experimental curves. Points $A(\delta_1; P_1)$, $B(\delta_2; P_2)$ and $C(\delta_3; P_3)$ which defines changes in the quality of the response of the specimen were manually located on the envelope of the experimental curves for each FRCM system. Values of δ_1 and δ_2 were directly obtained from the slips corresponding to points A and B. Values of the shear stresses τ_1 and τ_2 were obtained through Equation 2.27 and Equation 2.28. The predictive analytical curves of DST, based on such CML values were then retrieved through the integration of the differential equation of equilibrium implemented in the software Mathematica, with a code previously developed by Giulia Misseri, Department of Architecture, University of Florence. On the basis of visual comparison between predictive curves and experimental envelopes, the calibration of CML parameters was repeated until the prediction of analytical curves was deemed satisfactory, see analytical curves in Figure 6.12. The obtained stress values τ_1 and τ_2 and slip values, δ_1 and δ_1, defining the CML are reported in Table 6.7.

6.3 MODELLING OF DTT RESULTS

Results of the direct tensile tests of the experimental campaign were estimated through the proposed finite difference model, here specifically implemented in

Mathematica. Tests for the characterisation of the FRCM systems constituents enabled the definition of the mechanical parameters employed, which are reported in Table 6.7. Values of matrix tensile strength, f_{tm} were instead selected through fitting of experimental load slip diagrams of DTT. Values of f_{tm} inducing crack formation, were between 1/4 and 1/2 of the indirect tensile strength obtained through three-point bending tests, Table 6.6. Such framework is compliant with interpretation models (Soranakom and Mobasher 2010a; Grande et al. 2018) accounting for the effect of random defects and the slender ratio of the cross-section, which can ease crack formation in specimens subject to tightening. The predictive curve of DST, based on the calibrated CML and obtained through the integration of the differential equation of equilibrium implemented in Mathematica and through the proposed model are reported in Figure 6.12 superposed to the envelopes of experimental outcomes. For the PBO10, PBO22 and BAS systems, after the attainment of peak load a sudden decrease of the slip, i.e., a snap-back, is described by the solution provided by the system of differential equations. Such behaviour is not observed in the FDM estimation which is obtained through a displacement-driven loading procedure. For the CAR system, the predictive curves do not fully reproduce the behaviour of the composite, since the early tensile failure of the textile did not allow a correct calibration of the CML; as shown in Fazzi, Misseri, and Rovero (2023), a satisfactory estimation can be found considering textile tensile strength.

For the prediction of DTT results, the effect of clamping compression was considered through a modified CML for the nodes in the gripping areas; a 0.4 friction coefficient was assumed to model the restraining effect on slip exerted by the clamping set-up. Therefore, the values of τ_1 and τ_2 stress referring to clamped nodes were increased by 1.88 MPa, obtained considering the clamping compres-
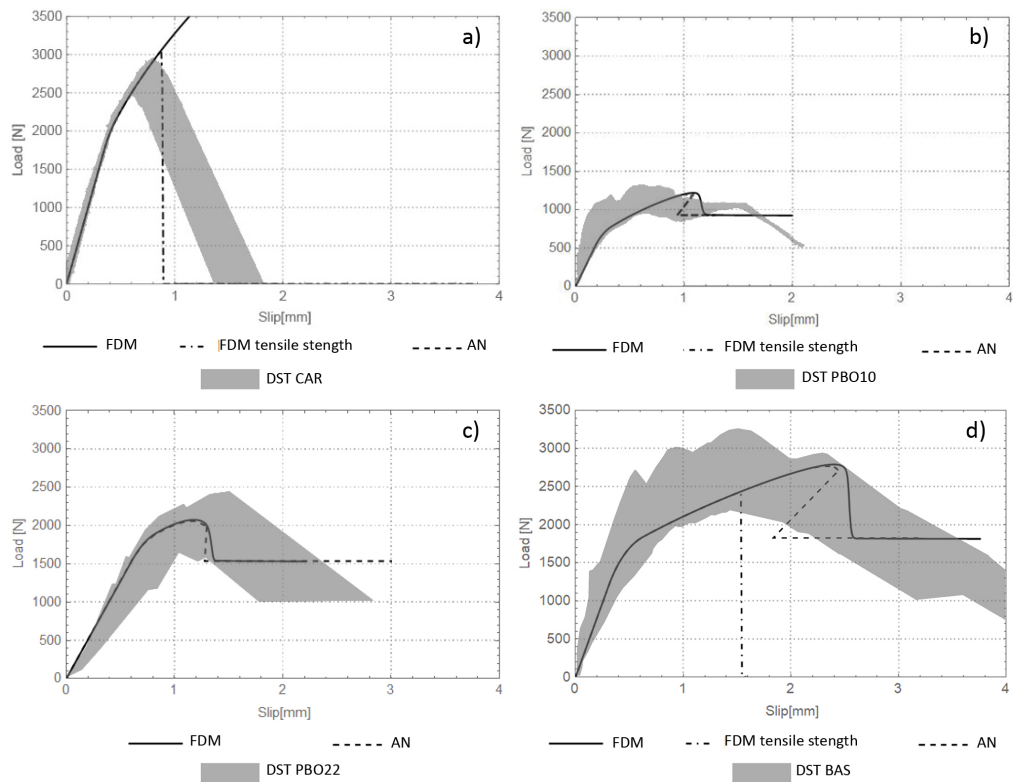
Figure 6.12: Predictive curve of DST based on the calibrated CML obtained through the proposed finite difference model without (FDM) and with tensile strength (FDM tensile strength) and through analytical model (AN). Curves are printed over the envelopes of experimental results of FRCM systems reinforced with (a) CAR, (B) PBO10, (C) PBO22 and (d) BAS textiles.
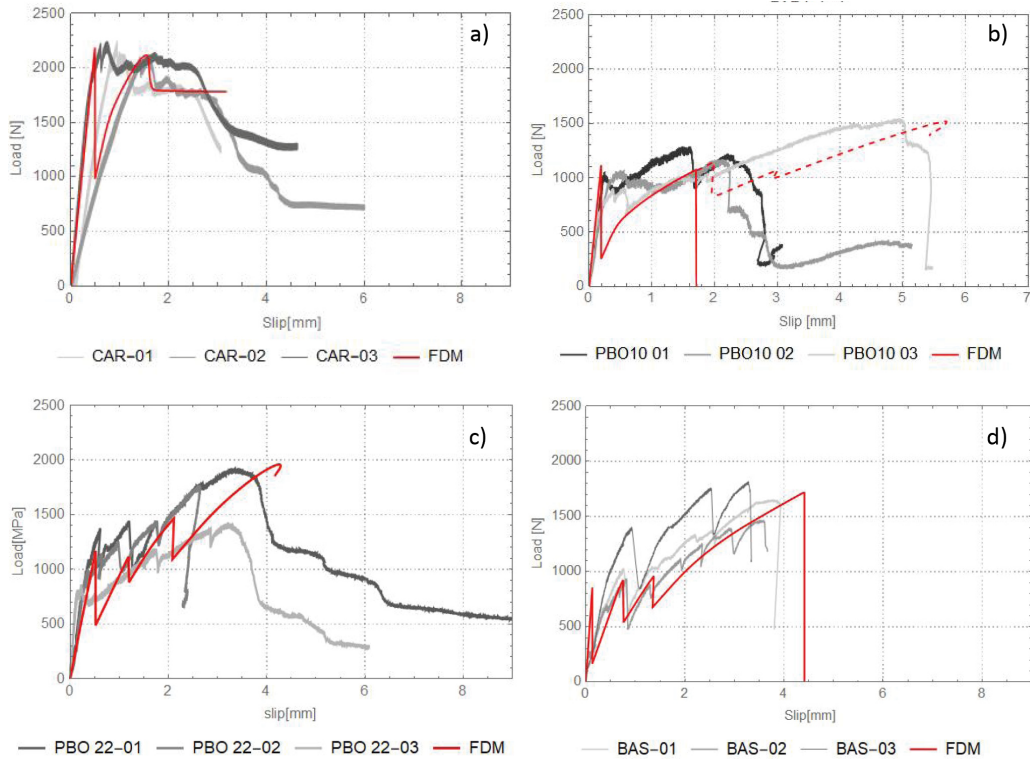
Figure 6.13: Prediction through the proposed finite difference model (FDM) of the load-slip diagrams of the FRCM systems reinforced with (a) CAR, (b) PBO10, (c) PBO22 and (d) BAS textiles.

sion, 4.7MPa, derived from the torque assigned to the bolts.

The model estimations correctly capture the main features highlighted by experimental tests. The load slip diagram prediction for the carbon-based system shows a linear elastic branch reaching up to a 2178 N peak load at 0.49 mm slip. After the formation of one crack, the predicted diagrams reach up to a load value of 2113 N and, after a short descending branch, provide a frictional plateau at 1780N.

For the PBO10-based system, the model provides a linear ascending branch up to a peak load equal to 1182 N, followed by a crack and a non-linear load recovery phase reaching tensile failure of the textile at 974 N and 1.44 mm slip value. Since textile strength was provided by only two direct tensile tests, see Section 6.1.3,

the predictive curve obtained without setting tensile strength for the textile is also reported with a dashed line in Figure 6.11b: a load and slip capacity of 1550 N and 5.75 mm are obtained respectively, showing a behaviour closer to specimen PBO10-03.

For the PBO22 system a linear elastic branch ending at load value 1171 MPa and a peak load equal to 1959 MPa are provided, Figure 6.13c. The cracking phase extends between 0.48 mm and 1.96 mm slip. No tensile failure of the fibre is reached.

For the basalt-based system, the model estimation provides an uncracked phase showing the same stiffness as the initial part of the experimental diagrams and a cracking phase extending between 0.14 mm and 1.38 mm slip, Figure 6.13d. A 1711 N peak load and a failure mode due to reaching fibre tensile strength are estimated by the model.

The application to experimental data proved that the model can provide good estimations of the mechanical behaviour of FRCM subject to DTT; in particular, a good prediction of the load reached at the end of the uncracked phase, the peak load, the stiffness of the uncracked phase, the degradation caused by crack openings and the failure mode experienced by different systems. The main discrepancies between model estimations and experimental outcomes are encountered in the load drop caused by crack openings. Relying on non deformable matrix assumptions, the model envisages brittle crack formation only, and fracture energy dissipated in the crack opening process is not accounted for. The load drop predicted by the model can be greater than the one recorded experimentally also due to the presence of short dispersed fibres bridging cracks. Nonetheless, the stiffness of the cracked phases experienced by the specimen during trials is satisfactory and close to experimental curves.

CHAPTER 7

Conclusions

7.1 CONCLUDING REMARKS

The present study was aimed at contributing to a better understanding of the mechanical behaviour of FRCM materials. In particular, the research pursued an improved understanding of the relationship between the great variability of results obtained in characterization tests in terms of test set-ups, variation of mechanical and geometrical parameters defining constituent materials, shape of the load-slip diagram, and failure mode.

Such issues were addressed through the implementation of a finite difference model, which accounts for the shear transfer mechanism at the fibre-to-matrix interface. The enforcement of appropriate boundary and continuity conditions allowed modelling of FRCM composite systems in direct shear (DST) and tensile (DTT) tests. It was shown that different loading conditions determined by set-up can also be considered in the model.

A specific displacement-driven procedure was developed for the DTT, overcoming the problem of a non-unique solution, stated in Soranakom (2008), through the introduction of combination coefficients, also taking into account Focacci, D'Antino, and Carloni (2020). Therefore the maximum load attainable by the system could be found and cracks opening in random positions of the domain could be considered.

Based on independent solutions which consider the system in different phases since the beginning of the loading process, a new procedure was also developed for the construction of the load slip diagram of DTT, allowing estimation of load

drops and stiffness degradation caused by cracks opening.

Application to experimental data proved that the model can provide good estimations of the mechanical behaviour of different FRCM systems in DTT. Some divergences between model estimations and experimental outcomes were encountered in the load drop caused by crack openings: relying on a minimal number of assumptions, the model envisages brittle crack formation only, and fracture energy dissipated in the crack opening process is not considered. Stronger validation of the implemented procedure could be achieved through comparison with a wider number of experimental outcomes.

A parametric analysis also highlighted that matrix tensile property and its distribution along the reinforcement play a relevant role in determining the response of FRCM systems. In particular the random distribution of matrix tensile strength, accounting for the presence of defects, induces crack-separated portions of the domain with different lengths, which greatly influence the load and slip capacity of the system:

- Longer extremity portions (cracks closer to the central part of the domain) induce a stiffer cracking phase and smaller load drops.

- The length of the shortest extremity portion is the driving parameter affecting the response quality in displacement terms and maximum load capacity, which coincides with the maximum bond force of the shortest extremity portion. While the dimension of the longest extremity portion does not affect the peak load reached by the system, it influences the slip capacity: longer portions decrease global displacement capacity. Since crack location is determined by the random distribution of the tensile strength, through the DTT, different strain capacities can be recorded for the same mechanical system.

The quality of the response of DTT does not rely on the bond properties of the composite system only; also the relation with matrix tensile strength deeply affects the shape of the load slip diagram:

- For the same maximum bond stress, τ_1, the increase in matrix tensile strength lengthens the cracking phase and determines the modification of the global diagram shape from tri-linear to bi-linear.

- For the same mortar tensile strength, the τ_1 increase increases the post-cracking maximum load and related slip and decreases the span of the cracking phase modifying the global diagram shape from bi-linear to tri-linear.

- For CMLs with the same geometrical ratios, similar relationships between bond stresses, τ_1, and tensile strength, f_{tm}, produce self-similar diagrams with scaled values.

The analysis hitherto carried out highlights the role of matrix tensile strength in the definition of the tensile behaviour of FRCM systems. In fact, the random distribution of matrix tensile strength along the specimen length can induce cracks to open at equally random positions and therefore determines:

- the load at the end of the uncracked phase.

- the stiffness of the uncracked phase.

- the peak load attainable by the system (in case of no premature failure of the textile) that is equal to the load transferred at the matrix to fibre interface of the shortest crack-separated segments.

- the strain capacity of the system.

- the possibility of the formation of further cracks: if the maximum load transferable by the shortest extremity portion does not allow reaching again matrix tensile strength, the cracking process is inhibited.

The ability of the proposed model to assess the variation of matrix tensile strength, CML properties and crack pattern implies that a wide range of FRCM systems can be modelled within it. The assessed parameters allow accounting for the specific properties of both the inorganic matrix and the reinforcement, which define the mechanical behaviour of the composite and are engineered to achieve desired structural performances in applications. From this perspective, the proposed model can be considered an effective tool for the development and optimization of FRCM systems.

BIBLIOGRAPHY

[1] ICC AC434. "Acceptance criteria for masonry and concrete strengthening using fiber-reinforced cementitious matrix (FRCM) composite systems". In: *ICC-Evaluation Service, Whittier, CA* (2013).

[2] ACI 549.4 R-13. *Guide to Design and Construction of Externally Bonded Fabric-Reinforced Cementitious Matrix (FRCM) Systems for Repair and Strengthening Concrete and Masonry Structures*. American Concrete Institute, 2013.

[3] Valerio Alecci, Sara Barducci, Mario De Stefano, Stefano Galassi, Raimondo Luciano, Luisa Rovero, and Gianfranco Stipo. "Reliability of Different Test Setups and Influence of Mortar Mixture on the Fabric-Reinforced Cementitious Matrix-to-Brick Bond Response". In: *Journal of Testing and Evaluation* 49.6 (2021).

[4] Valerio Alecci, Mario De Stefano, Raimondo Luciano, Luisa Rovero, and Gianfranco Stipo. "Experimental investigation on bond behavior of cement-matrix–based composites for strengthening of masonry structures". In: *Journal of Composites for Construction* 20.1 (2016).

[5] Diana Arboleda, Francesca Giulia Carozzi, Antonio Nanni, and Carlo Poggi. "Testing procedures for the uniaxial tensile characterization of fabric-reinforced cementitious matrix composites". In: *Journal of Composites for Construction* 20.3 (2016).

[6] Luigi Ascione, Gianmarco De Felice, and Stefano De Santis. "A qualification method for externally bonded Fibre Reinforced Cementitious Matrix

(FRCM) strengthening systems". In: *Composites Part B: Engineering* 78 (2015), pp. 497–506.

[7]   Domenico Asprone, Massimo Durante, Andrea Prota, and Gaetano Manfredi. "Potential of structural pozzolanic matrix–hemp fiber grid composites". In: *Construction and Building Materials* 25.6 (2011), pp. 2867–2874.

[8]   Björn Banholzer. "Bond behaviour of a multi-filament yarn embedded in a cementitious matrix". PhD thesis. Bibliothek der RWTH Aachen, 2004.

[9]   Björn Banholzer, Wolfang Brameshuber, and Wolf Jung. "Analytical evaluation of pull-out teststhe inverse problem". In: *Cement and Concrete Composites* 28.6 (2006), pp. 564–571.

[10] Björn Banholzer, Wolfang Brameshuber, and Wolf Jung. "Analytical simulation of pull out tests the direct problem". In: *Cement and Concrete Composites* 27.1 (2005), pp. 93–101.

[11] Rabea Barhum and Viktor Mechtcherine. "Effect of short, dispersed glass and carbon fibres on the behaviour of textile-reinforced concrete under tensile loading". In: *Engineering Fracture Mechanics* 92 (2012), pp. 56–71.

[12] Arnon Bentur, RJ Gray, and S Mindess. "Cracking and pull-out processes in fibre reinforced cementitious materials". In: *3th Symp. on Developments in Fibre Reinforced Cement and Concrete: RFC*. Vol. 86. 1986.

[13] Elisa Bertolesi, Francesca Giulia Carozzi, Gabriele Milani, and Carlo Poggi. "Numerical modeling of Fabric Reinforce Cementitious Matrix composites (FRCM) in tension". In: *Construction and Building Materials* 70 (2014), pp. 531–548.

[14] Veronica Bertolli and Tommaso D'Antino. "Modeling the behavior of externally bonded reinforcement using a rigid-trilinear cohesive material law". In: *International Journal of Solids and Structures* 248 (2022).

[15] Antonio Bilotta and Gian Piero Lignola. "Effect of fiber-to-matrix bond on the performance of inorganic matrix composites". In: *Composite Structures* 265 (2021).

[16] Carmelo Caggegi, Francesca Giulia Carozzi, Stefano De Santis, Francesco Fabbrocino, Francesco Focacci, ukasz Hojdys, Emma Lanoye, and Luigia Zuccarino. "Experimental analysis on tensile and bond properties of PBO and aramid fabric reinforced cementitious matrix for strengthening masonry structures". In: *Composites Part B: Engineering* 127 (2017), pp. 175–195.

[17] Angelo Savio Calabrese, Pierluigi Colombi, and Tommaso D'Antino. "Analytical solution of the bond behavior of FRCM composites using a rigid-softening cohesive material law". In: *Composites Part B: Engineering* 174 (2019).

[18] Christian Carloni, Tommaso D'Antino, Lesley H Sneed, and Carlo Pellegrino. "Role of the matrix layers in the stress-transfer mechanism of FRCM composites bonded to a concrete substrate". In: *J. Eng. Mech* 141.6 (2015).

[19] Francesca Giulia Carozzi, Alessandro Bellini, Tommaso D'Antino, Gianmarco De Felice, Francesco Focacci, Lukasz Hojdys, Luca Laghi, Emma Lanoye, Francesco Micelli, and Matteo Panizza. "Experimental investigation of tensile and bond properties of Carbon-FRCM composites for strengthening masonry elements". In: *Composites Part B: Engineering* 128 (2017), pp. 100–119.

[20] Francesca Giulia Carozzi, Pierluigi Colombi, Giulia Fava, and Carlo Poggi. "A cohesive interface crack model for the matrix–textile debonding in FRCM composites". In: *Composite Structures* 143 (2016), pp. 230–241.

[21] Francesca Giulia Carozzi, Gabriele Milani, and Carlo Poggi. "Mechanical properties and numerical modeling of Fabric Reinforced Cementitious Matrix (FRCM) systems for strengthening of masonry structures". In: *Composite Structures* 107 (2014), pp. 711–725.

[22] EN CEN. "1015-11: Methods of test for mortar for masonry-Part 11: Determination of flexural and compressive strength of hardened mortar". In: *European Committee for Standardization, Brussels* (1999).

[23] Francesca Ceroni and Piera Salzano. "Design provisions for FRCM systems bonded to concrete and masonry elements". In: *Composites Part B: Engineering* 143 (2018), pp. 230–242.

[24] CNR. "CNR-DT 200R1/2013 Istruzioni per la Progettazione , l'Esecuzione ed il Controllo di Interventi di Consolidamento Statico mediante l'utilizzo di Compositi Fibrorinforzati". In: *CNR: Consiglio Nazionale delle Ricecrche* (2014).

[25] CNR. "CNR-DT 215/2018 Istruzioni per la Progettazione , l'Esecuzione ed il Controllo di Interventi di Consolidamento Statico mediante l'utilizzo di Compositi Fibrorinforzati a matrice inorganica". In: *CNR: Consiglio Nazionale delle Ricecrche* (2018).

[26] Pierluigi Colombi and Tommaso D'Antino. "Analytical assessment of the stress-transfer mechanism in FRCM composites". In: *Composite Structures* 220 (2019), pp. 961–970.

[27]   ACI Committee et al. "ACI 549.4 R-13: Guide to Design and Construction of Externally Bonded Fabric-Reinforced Cementitious Matrix (FRCM) Systems for Repair and Strengthening Concrete and Masonry Structures". In: *American Concrete Institute*. 2013.

[28]   Centrale CSLLPP Servizio Tecnico. "Linee guida per la identificazione, la qualificazione ed il controllo di accettazione di compositi fibrorinforzati a matrice inorganica (FRCM) da utilizzarsi per il consolidamento strutturale di costruzioni esistenti". In: *Rome, Italy* (2019).

[29]   Tommaso D'Antino, Angelo Savio Calabrese, and Carlo Poggi. "Experimental procedures for the mechanical characterization of composite reinforced mortar (CRM) systems for retrofitting of masonry structures". In: *Materials and Structures* 53.4 (2020), pp. 1–18.

[30]   Tommaso D'Antino, Christian Carloni, Lesley H Sneed, and Carlo Pellegrino. "Matrix-fiber bond behavior in PBO FRCM composites: A fracture mechanics approach". In: *Engineering Fracture Mechanics* 117 (2014), pp. 94–111.

[31]   Tommaso D'Antino, Pierluigi Colombi, Christian Carloni, and Lesley H Sneed. "Estimation of a matrix-fiber interface cohesive material law in FRCM-concrete joints". In: *Composite structures* 193 (2018), pp. 103–112.

[32]   Tommaso D'Antino and Catherine Corina Papanicolaou. "Comparison between different tensile test set-ups for the mechanical characterization of inorganic-matrix composites". In: *Construction and Building Materials* 171 (2018), pp. 140–151.

[33] Angelo DAmbrisi, Luciano Feo, and Francesco Focacci. "Experimental analysis on bond between PBO-FRCM strengthening materials and concrete". In: *Composites Part B: Engineering* 44.1 (2013), pp. 524–532.

[34] Angelo DAmbrisi, Luciano Feo, and Francesco Focacci. "Experimental and analytical investigation on bond between Carbon-FRCM materials and masonry". In: *Composites Part B: Engineering* 46 (2013), pp. 15–20.

[35] Ali Dalalbashi, Bahman Ghiassi, and Daniel V. Oliveira. "A multi-level investigation on the mechanical response of TRM-strengthened masonry". In: *Materials and Structures* 54.6 (2021), pp. 1–19.

[36] Ali Dalalbashi, Bahman Ghiassi, and Daniel V. Oliveira. "Textile-to-mortar bond behavior: An analytical study". In: *Construction and Building Materials* 282 (2021).

[37] Ali Dalalbashi, Bahman Ghiassi, Daniel V. Oliveira, and Ana Freitas. "Fiber-to-mortar bond behavior in TRM composites: effect of embedded length and fiber configuration". In: *Composites Part B: Engineering* 152 (2018), pp. 43–57.

[38] Gianmarco De Felice, Maria Antonietta Aiello, Carmelo Caggegi, Francesca Ceroni, Stefano De Santis, Enrico Garbin, Natalino Gattesco, ukasz Hojdys, Piotr Krajewski, and Arkadiusz Kwiecie. "Recommendation of RILEM Technical Committee 250-CSM: Test method for Textile Reinforced Mortar to substrate bond characterization". In: *Materials and Structures* 51.4 (2018), pp. 1–9.

[39] Stefano De Santis, Francesca Giulia Carozzi, Gianmarco De Felice, and Carlo Poggi. "Test methods for Textile Reinforced Mortar systems". In: *Composites Part B: Engineering* 127 (2017), pp. 121–132.

[40] Stefano De Santis, Francesca Ceroni, Gianmarco De Felice, Mario Fagone, Bahman Ghiassi, Arkadiusz Kwiecien, Gian Piero Lignola, Mattia Morganti, Mattia Santandrea, and Maria Rosa Valluzzi. "Round Robin Test on tensile and bond behaviour of Steel Reinforced Grout systems". In: *Composites Part B: Engineering* 127 (2017), pp. 100–120.

[41] Stefano De Santis, Houman Hadad, Francisco De Caso y Basalo, Gianmarco De Felice, and Antonio Nanni. "Acceptance criteria for tensile characterization of fabric-reinforced cementitious matrix systems for concrete and masonry repair". In: *Journal of Composites for Construction* 22.6 (2018).

[42] Jacopo Donnini, Giovanni Lancioni, and Valeria Corinaldesi. "Failure modes in FRCM systems with dry and pre-impregnated carbon yarns: Experiments and modeling". In: *Composites Part B: Engineering* 140 (2018), pp. 57–67.

[43] Eloisa Fazzi, Giulia Misseri, and Luisa Rovero. "Experimental, analytical, and numerical investigations on bond behaviour of basalt TRM systems". In: *International Journal of Masonry Research and Innovation* 8.2-3 (2023), pp. 333–354.

[44] Eloisa Fazzi, Giulia Misseri, Luisa Rovero, and Gianfranco Stipo. "Finite Difference Model for the Bond Behaviour of Polyparaphenylene Benzobisoxazole (PBO) Fibre-Reinforced Composite System for Retrofitting Masonry". In: 916 (2022), pp. 425–432.

[45] Francesco Focacci, Tommaso D'Antino, and Christian Carloni. "Relationship between Results of Tensile Test of FRCM Composites and the Fiber-Matrix Bond Properties". In: *Key Engineering Materials*. Vol. 916. Trans Tech Publ. 2022, pp. 417–424.

[46] Francesco Focacci, Tommaso D'Antino, and Christian Carloni. "Tensile testing of FRCM coupons for material characterization: discussion of critical aspects". In: *Journal of Composites for Construction* 26.4 (2022).

[47] Francesco Focacci, Tommaso D'Antino, and Christian Carloni. "The role of the fibermatrix interfacial properties on the tensile behavior of FRCM coupons". In: *Construction and Building Materials* 265 (2020).

[48] Francesco Focacci, Tommaso D'Antino, Christian Carloni, Lesley H Sneed, and Carlo Pellegrino. "An indirect method to calibrate the interfacial cohesive material law for FRCM-concrete joints". In: *Materials & Design* 128 (2017), pp. 206–217.

[49] Bahman Ghiassi, Daniel V. Oliveira, Vera Marques, Edgar Soares, and Hamid Maljaee. "Multi-level characterization of steel reinforced mortars for strengthening of masonry structures". In: *Materials & Design* 110 (2016), pp. 903–913.

[50] Ernesto Grande, Bahman Ghiassi, and Maura Imbimbo. "Theoretical and FE models for the study of the bond behavior of FRCM systems". In: *Numerical modeling of masonry and historical structures*. Elsevier, 2019, pp. 685–712.

[51] Ernesto Grande, Maura Imbimbo, Sonia Marfia, and Elio Sacco. "Numerical simulation of the de-bonding phenomenon of FRCM strengthening systems". In: *Procedia Structural Integrity* 9 (2018), pp. 257–264.

[52] Ernesto Grande and Gabriele Milani. "Interface modeling approach for the study of the bond behavior of FRCM strengthening systems". In: *Composites Part B: Engineering* 141 (2018), pp. 221–233. ISSN: 1359-8368.

[53] Ernesto Grande and Gabriele Milani. "Numerical simulation of the tensile behavior of FRCM strengthening systems". In: *Composites Part B: Engineering* 189 (2020).

[54] Ernesto Grande and Gabriele Milani. "Procedure for the numerical characterization of the local bond behavior of FRCM". In: *Composite Structures* 258 (2021).

[55] Jens Hartig, Ulrich HäuSSler-Combe, and Kai Schicktanz. "Influence of bond properties on the tensile behaviour of Textile Reinforced Concrete". In: *Cement and concrete composites* 30.10 (2008), pp. 898–906.

[56] Jens Hartig, Frank Jesse, Kai Schicktanz, and Ulrich HäuSSler-Combe. "Influence of experimental setups on the apparent uniaxial tensile load-bearing capacity of textile reinforced concrete specimens". In: *Materials and structures* 45.3 (2012), pp. 433–446.

[57] Ulrich HäuSSler-Combe and Jens Hartig. "Bond and failure mechanisms of textile reinforced concrete (TRC) under uniaxial tensile loading". In: *Cement and concrete composites* 29.4 (2007), pp. 279–289.

[58] J Hegger, N Will, Oliver Bruckermann, and Stefan Voss. "Load–bearing behaviour and simulation of textile reinforced concrete". In: *Materials and structures* 39.8 (2006), pp. 765–776.

[59] S Igarashi, Arnon Bentur, and S Mindess. "The effect of processing on the bond and interfaces in steel fiber reinforced cement composites". In: *Cement and Concrete Composites* 18.5 (1996), pp. 313–322.

[60] Dong Joo Kim. "A review paper on direct tensile behavior and test methods of textile reinforced cementitious composites". In: *Composite Structures* 263 (2021), p. 113661.

[61] Leonidas Alexandros S Kouris and Thanasis C Triantafillou. "State-of-the-art on strengthening of masonry structures with textile reinforced mortar (TRM)". In: *Construction and Building Materials* 188 (2018), pp. 1221–1233.

[62] Lampros N Koutas, Zoi Tetta, Dionysios A Bournas, and Thanasis C Triantafillou. "Strengthening of concrete structures with textile reinforced mortars: State-of-the-art review". In: *Journal of Composites for Construction* 23.1 (2019), p. 03118001.

[63] Marianovella Leone, Maria Antonietta Aiello, Alberto Balsamo, Francesca Giulia Carozzi, Francesca Ceroni, Marco Corradi, Matija Gams, Enrico Garbin, Natalino Gattesco, and Piotr Krajewski. "Glass fabric reinforced cementitious matrix: Tensile properties and bond performance on masonry substrate". In: *Composites Part B: Engineering* 127 (2017), pp. 196–214.

[64] Gian Piero Lignola, Carmelo Caggegi, Francesca Ceroni, Stefano De Santis, Piotr Krajewski, Paulo Lourenço, Mattia Morganti, Catherine Corina Papanicolaou, Carlo Pellegrino, and Andrea Prota. "Performance assessment of basalt FRCM for retrofit applications on masonry". In: *Composites Part B: Engineering* 128 (2017), pp. 1–18.

[65] Giulia Misseri, Luisa Rovero, and Stefano Galassi. "Analytical modelling bond behaviour of polybenzoxazole (PBO) and glass Fibre Reinforced Cementitious Matrix (FRCM) systems coupled with cement and gypsum ma-

trixes: Effect of the Cohesive Material Law (CML) shape". In: *Composites Part B: Engineering* 223 (2021).

[66]   Giulia Misseri, Gianfranco Stipo, Stefano Galassi, and Luisa Rovero. "Experimental Investigation on the Bond behaviour of Basalt TRM Systems-Influence of Textile Configuration and Multi-Layer Application". In: *Key Engineering Materials*. Vol. 817. Trans Tech Publ. 2019, pp. 134–140.

[67]   Barzin Mobasher, Jitendra Pahilajani, and Alva Peled. "Analytical simulation of tensile response of fabric reinforced cement based composites". In: *Cement and Concrete Composites* 28.1 (2006), pp. 77–89.

[68]   Barzin Mobasher, Alva Peled, and Jitendra Pahilajani. "Distributed cracking and stiffness degradation in fabric-cement composites". In: *Materials and structures* 39.3 (2006), pp. 317–331.

[69]   Antoine E Naaman, George G Namur, Jamil M Alwan, and Husam S Najm. "Fiber pullout and bond slip. I: Analytical study". In: *Journal of structural engineering* 117.9 (1991), pp. 2769–2790.

[70]   Francesca Nerilli and Barbara Ferracuti. "A tension stiffening model for FRCM reinforcements calibrated by means of an extended database". In: *Composite Structures* 284 (2022).

[71]   Francesca Nerilli, Sonia Marfia, and Elio Sacco. "Micromechanical modeling of the constitutive response of FRCM composites". In: *Construction and Building Materials* 236 (2020).

[72]   Francesca Nerilli, Sonia Marfia, and Elio Sacco. "Nonlocal damage and interface modeling approach for the micro-scale analysis of FRCM". In: *Computers & Structures* 254 (2021).

[73] RS Olivito, OA Cevallos, and A Carrozzini. "Development of durable cementitious composites using sisal and flax fabrics for reinforcement of masonry structures". In: *Materials & Design* 57 (2014), pp. 258–268.

[74] Alva Peled and Arnon Bentur. "Geometrical characteristics and efficiency of textile fabrics for reinforcing cement composites". In: *Cement and concrete research* 30.5 (2000), pp. 781–790.

[75] Alva Peled and Arnon Bentur. "Reinforcement of cementitious matrices by warp knitted fabrics". In: *Materials and structures* 31.8 (1998), pp. 543–550.

[76] Alva Peled, Arnon Bentur, and David Yankelevsky. "Effects of woven fabric geometry on the bonding performance of cementitious composites: mechanical performance". In: *Advanced Cement Based Materials* 7.1 (1998), pp. 20–27.

[77] Alva Peled, Zvi Cohen, Yonatan Pasder, Andreas Roye, and Thomas Gries. "Influences of textile characteristics on the tensile properties of warp knitted cement based composites". In: *Cement and concrete composites* 30.3 (2008), pp. 174–183.

[78] Alva Peled, Sachiko Sueki, and Barzin Mobasher. "Bonding in fabric–cement systems: effects of fabrication methods". In: *Cement and concrete research* 36.9 (2006), pp. 1661–1671.

[79] ICOMOS Principles. "Principles for the analysis, conservation and structural restoration of architectural heritage". In: *Proceedings of the ICOMOS 14th General Assembly in Victoria Falls, Victoria Falls, Zimbabwe* (2003), pp. 27–31.

[80] Arezoo Razavizadeh, Bahman Ghiassi, and Daniel V. Oliveira. "Bond behavior of SRG-strengthened masonry units: Testing and numerical modeling". In: *Construction and Building Materials* 64 (2014), pp. 387–397.

[81] Technical Committee 232-TDT RILEM. "Recommendation of RILEM TC 232-TDT: test methods and design of textile reinforced concrete: Uniaxial tensile test: test method to determine the load bearing behavior of tensile specimens made of textile reinforced concrete". In: *Materials and Structures/Materiaux et Constructions* 49.12 (2016), pp. 4923–4927.

[82] Luisa Rovero, Stefano Galassi, and Giulia Misseri. "Experimental and analytical investigation of bond behavior in glass fiber-reinforced composites based on gypsum and cement matrices". In: *Composites Part B: Engineering* 194 (2020).

[83] Lesley H Sneed, Tommaso D'Antino, and Christian Carloni. "Investigation of bond behavior of PBO fiber-reinforced cementitious matrix composite-concrete interface". In: *ACI Mater J* 111.5 (2014), pp. 569–580.

[84] Chote Soranakom. *Multi-scale modeling of fiber and fabric reinforced cement based composites*. Arizona State University, 2008.

[85] Chote Soranakom and Barzin Mobasher. "Geometrical and mechanical aspects of fabric bonding and pullout in cement composites". In: *Materials and Structures* 42.6 (2009), pp. 765–777.

[86] Chote Soranakom and Barzin Mobasher. "Modeling of tension stiffening in reinforced cement composites: Part I. Theoretical modeling". In: *Materials and Structures* 43.9 (2010), pp. 1217–1230. DOI: 10.1617/s11527-010-9594-8.

[87] Chote Soranakom and Barzin Mobasher. "Modeling of tension stiffening in reinforced cement composites: Part II. Simulations versus experimental results". In: *Materials and structures* 43.9 (2010), pp. 1231–1243.

[88] Sachiko Sueki, Chote Soranakom, Barzin Mobasher, and Alva Peled. "Pullout-slip response of fabrics embedded in a cement paste matrix". In: *Journal of Materials in Civil Engineering* 19.9 (2007), pp. 718–727.

[89] Van Doan Truong and Dong Joo Kim. "A review paper on direct tensile behavior and test methods of textile reinforced cementitious composites". In: *Composite Structures* 263 (2021). ISSN: 0263-8223.

[90] Van Doan Truong, Do Hyung Lee, and Dong Joo Kim. "Effects of different grips and surface treatments of textile on measured direct tensile response of textile reinforced cementitious composites". In: *Composite Structures* 278 (2021).

[91] ICOMOS Venice Charter. "International charter for the conservation and restoration of monuments and sites". In: $<https://www.icomos.org/charters/venice_e.pdf>[Accessed 22 June 2018]$ (1964).

[92] B Zastrau, M Richter, and I Lepenies. "On the analytical solution of pullout phenomena in textile reinforced concrete". In: *J. Eng. Mater. Technol.* 125.1 (2003), pp. 38–43.

[93] Xingxing Zou, Tommaso D'Antino, and Lesley H Sneed. "Investigation of the bond behavior of the fiber reinforced composite-concrete interface using the finite difference method (FDM)". In: *Composite Structures* 278 (2021).

ACADEMIC CURRICULUM VITAE

Eloisa Fazzi, MA

January 31, 2023

University of Florence

Piazza Brunelleschi, 6 Florence, 50121, Italy

Academic Training:

6/2023(expected)	PhD University of Florence, IT; Structures and Restoration of architecture and of the cultural heritage
04/2018	MA University of Florence, IT; Architecture
09/2015	BA University of Florence, IT; Architecture
09/2011	BA Catholic University of Milan, IT; Philosophy

Doctoral Research:

Title:	Fibre-reinforced cementitious matrix (FRCM) for masonry strengthening: modelling of textile-matrix interface.
Thesis advisor:	Prof. Luisa Rovero, PhD
Defense date:	August, 2023

Original, Peer Reviewed Publications (newest first):

1. <u>Eloisa Fazzi</u>, Giulia Misseri, Luisa Rovero, Experimental, analytical, and numerical investigations on bond behaviour of basalt TRM, *Int. J. of Masonry Research and Innovation systems*, in press.

2. <u>Eloisa Fazzi</u>, Giulia Misseri, Luisa Rovero, Gianfranco Stipo. Finite Difference Model for the Bond Behaviour of Polyparaphenylene Benzobisoxazole (PBO) Fibre-Reinforced Composite System for Retrofitting Masonry. *KEM 2022;916:42532*, April 2022 .

3. Stefano Galassi, Matteo Bigongiari, Giacomo Tempesta, Luisa Rovero, <u>Eloisa Fazzi</u>, Cheima Azil, Letizia Di Pasquale, Giovanni Pancani, Digital Survey and Structural Investigation on the Triumphal Arch of Caracalla in the Archaeological Site of Volubilis in Morocco: Retracing the Timeline of Collapses Occurred during the 18th Century Earthquake, *International Journal of Architectural Heritage, 16:6, 940-955*, April 2022 DOI: 10.1080/15583058.2022.2045387

4. <u>Eloisa Fazzi</u>, Stefano Galassi, Giulia Misseri, Luisa Rovero, Seismic vulnerability assessment of the benedictine basilica typology in central Italy, *Journal of Building Engineering, Volume 43*, November 2021, 102897, ISSN 2352-7102, .

5. Giovanni Pancani, Stefano Galassi, Luisa Rovero, Letizia Dipasquale, <u>Eloisa Fazzi</u>, Giacomo Tempesta, (2020). Seismic vulnerability assessment of the triumphal arch of Caracalla in Volubilis (Morocco): past events and provisions for the future. *International Archives of the Photogrammetry, Remote Sensing Spatial Information Sciences*, September 2020.